Production of High Strength Materials Using High-Pressure Torsion

李, 昇原
九州大学大学院工学府

https://doi.org/10.15017/22006

Production of High Strength Materials Using High-Pressure Torsion

By

Seungwon LEE

Under Supervision of:

Professor Zenji Horita

January 2012

Contents

Chapter 3. Simultaneous strengthening of Al alloys through grain refinement and fine precipitation using high-pressure torsion and subsequent aging

Certificate

The undersigned reviewing committee members hereby certify that **Seungwon LEE** defended his thesis entitled "**Production of high strength materials using high-pressure torsion**" on February, 2012 and the thesis was accepted in fulfillment of the requirement for the degree of Doctor of Engineering at Kyushu University.

Zenji HORITA

(Professor, Faculty of Engineering, Kyushu University)

Minoru NISHIDA

(Professor, Faculty of Engineering Sciences, Kyushu University)

Kenji MATSUDA

(Professor, Faculty of Engineering, University of Toyama)

Chapter 1. Introduction

1.1. Background

1.1.1. Severe plastic deformation (SPD)

There are several important methods for improving mechanical properties of material for example, work hardening, grain refinement, solid solution hardening and precipitation hardening. Among them, grain refinement is well defined by Hall-Petch equation [1, 2]

$$\sigma = \sigma_0 + kd^{-1/2} \tag{1.1}$$

where σ is the yield strength, d is the average grain diameter, and σ_0 and k are constants that depend on the material. However, at very small grain sizes, it is clear that exceptional properties would be expected if this relation continues to hold. Because of this potential, researchers have tried to make materials with as smaller grain size as possible. Early researches were based on traditional thermo-mechanical processing, i.e., heavy cold work followed by low-temperature recrystallization heat treatments.

Two decades ago, bulk ultrafine/ nano structured materials started to research by methods of severe plastic deformation (SPD). The SPD process is very attractive and interesting method to specialists who are in the field of materials science because of their powerful ability to generate ultrafine/nano sized grains [3].

The materials which are processed with SPD methods can be compared with conventional methods, where intense strain is imposed by the SPD process without any

significant change in the overall dimensions of the sample. Several methods were developed for the SPD process, which mainly include equal-channel angular pressing (ECAP), accumulative roll-bonding (ARB), and high-pressure torsion (HPT) and they are at present the most developed SPD processing techniques.

The method of ECAP was introduced by Segal *et al*. [4] in 1981 as illustrated in Fig. 1.1, it is designed to impose shear stress into billets. During ECAP processing, a billet is multiple pressed through a special die using an ECAP facility in which the angle of intersection of two channels is usually 90^{o}. During repetitive processing, billet is deformed with shear introduced by die angle. Equivalent strain can be calculated by the following equation [5].

$$\varepsilon = \frac{N}{\sqrt{3}}\left[2\cot\left(\frac{\Phi}{2}+\frac{\Psi}{2}\right)\right] + \Psi\mathrm{cosec}\left[\left(\frac{\Phi}{2}+\frac{\Psi}{2}\right)\right] \quad (1.2)$$

where N is the number of passes through the die, Φ is the angle between the two parts of the channel and Ψ is the angle for the outer arc of curvature. For the channel angle $\varphi = 90°$ and a corner angle approximately $\psi = 20°$, the equivalent strain for each pass subjected to each specimen is about 1.05 [4].

ARB was developed by Saito *et al*. in 1998. The principle of the ARB process is schematically illustrated in Fig. 1.2. The ARB is a kind of SPD process using rolling deformation. In the ARB process, for example, a 2mm thick sheet is first rolled by 50% reduction in thickness.

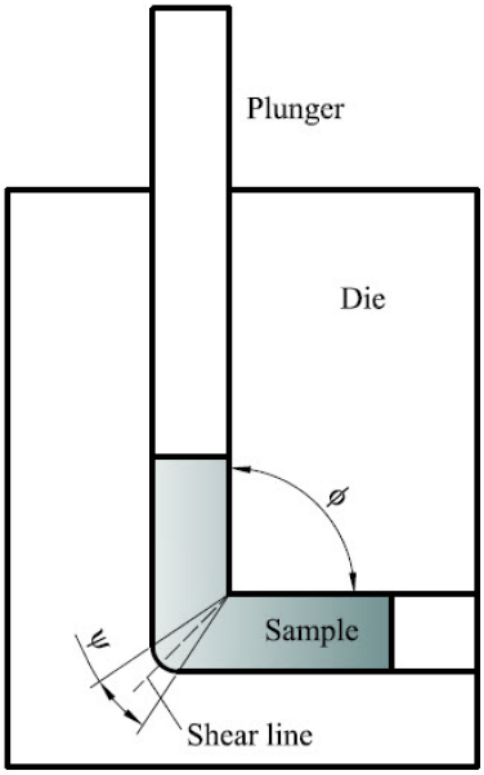

Figure 1.1. Schematic illustration for ECAP process [4].

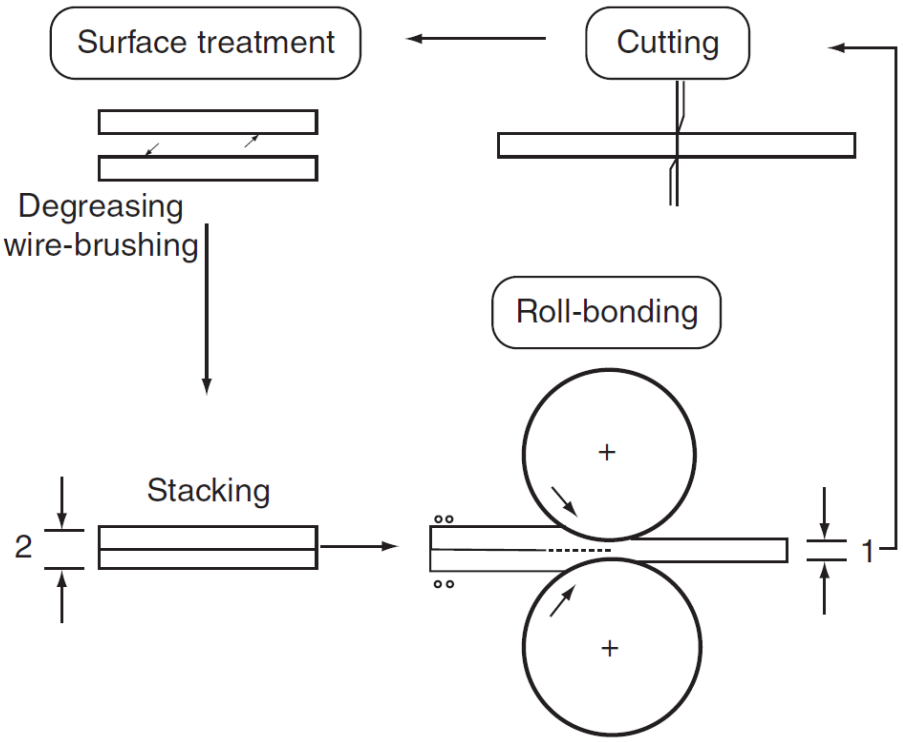

Figure 1.2. Schematic illustration for ARB process [6].

The rolled sheets are cut into two halves, stacked to obtain the initial dimensions and then rolled again. The equivalent strain after *n* cycles of the ARB can be expressed as [6]

$$\varepsilon = -\frac{2N}{\sqrt{3}}\, ln\frac{t}{t_0} = -\frac{2N}{\sqrt{3}} \ln (l - r) \tag{1.3}$$

where t_0, t, and r are initial thickness of the stacked sheets, the thickness after roll-bonding, and the reduction in thickness per cycle, respectively. When 1mm thickness samples are subjected to ARB process, equivalent strain can be described with $0.8n$ [6].

1.1.2. High-pressure torsion (HPT)

Basic concept of HPT process was introduced first by Bridgman in 1935 [7], as illustrated in Fig. 1.3(a). It was designed to introduce large strain into disk samples. A small thin disk is put between two hardened steel anvils and shear strain is introduced by rotating the two anvils with respect to each other. In order to achieve high pressures, a modified facility is usually used for HPT [8]. As illustrated in Fig.1.4, the modified facility consists of massive upper and lower anvils having a shallow flat-bottomed hole at the center. A small thin disk is placed in the shallow hole of the lower anvil and the lower anvil is raised to contact the upper. A high hydrostatic pressure is applied to the sample and intense shear strain is introduced by rotating the lower anvil with respect to the upper anvil. Here, the equivalent strain is given by [9]

$$\varepsilon = \frac{2\pi rN}{\sqrt{3}t} \tag{1.4}$$

where *r* is the distance from the disk center, *N* is the number of revolutions and *t* is the thickness of the disk. Figure 1.5 shows an HPT facility which used for this study and sample after HPT processing. There are some advantages of HPT process compared to other SPD processes.

1) HPT process can produce smaller grains with enhanced mechanical properties because of its extremely large strain.
2) During HPT process, fracture or crack propagation is suppressed because of its high pressure.
3) Material selection for HPT process has less limitation even in hard-to-deform materials such as refractory metals (V, Cr, Nb, Mo [10, 11], W [12], ceramics Al2O3 [13] and intermetallics Ni3Al [14]).
4) The application of HPT process has been extended not only to bulk metals but also to powders [5, 16], composites [17, 18], ceramic powders [19] and Amorphous compounds [20, 21], *etc*.

Despite these advantages, HPT process has one disadvantage in scaling up sample size when compared with other SPD processes. Thus some attempts have been conducted to scale up the sample size and developed with new methods such as ring-HPT [22] and continuous HPT [23].

1.1.3. Strengthening of metals

There are four methods of increasing the hardness of metallic materials

(i) Work hardening

(ii) Solid-solution hardening,

(iii) Precipitation hardening

(iv) Grain refinement hardening

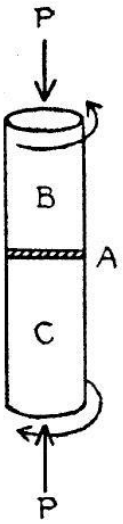

Figure 1.3. Schematic illustration of Bridgeman anvil.

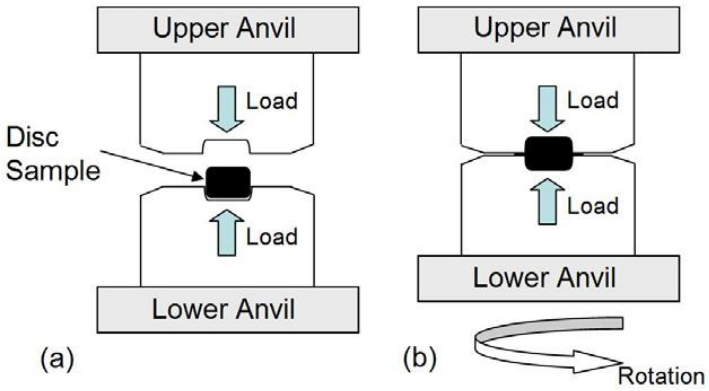

Figure 1.4. Schematic illustration for modified HPT facility.

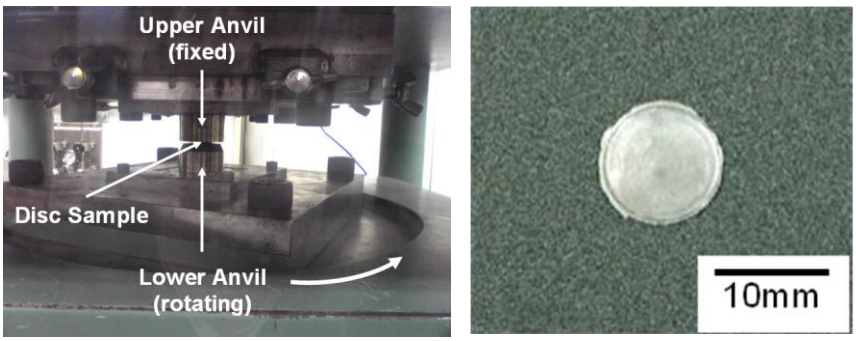

Figure 1.5. HPT facility used in this study (left) and Al sample after HPT processing (right).

Work hardening

The primary species responsible for work hardening are dislocations. Dislocations interact with each other by generating stress fields in the material. The interaction between the stress fields of dislocations can impede dislocation motion by repulsive or attractive interactions. Additionally, if two dislocations cross, dislocation line entanglement occurs, causing the formation of a jog which opposes dislocation motion. These entanglements and jogs act as pinning points, which oppose dislocation motion. As both of these processes are more likely to occur when more dislocations are present, there is a correlation between dislocation density and stress flow [24, 25]

$$\tau = \alpha G b \sqrt{\rho} \tag{1.5}$$

where α is a constant in the range of 0.3-1.0, G is the shear modulus, b is the Burgers vector, and ρ is the dislocation density. Increasing the dislocation density leads to an increase in the flow stress flow which results in a higher shear stress required to move the dislocations. This process is easily observed while working a material.

Solid solution strengthening

For this strengthening mechanism, solute atoms of one element are added to another, resulting in either substitutional or interstitial point defects in the crystal. The solute atoms cause lattice distortions that impede dislocation motion, increasing the yield stress of the material. Solute atoms have stress fields around them which can interact with those of dislocations. The presence of solute atoms imparts compressive or tensile stresses to the lattice, depending on solute size, which interfere with nearby dislocations, causing the solute atoms to act as potential barriers to dislocation

propagation and/or multiplication. The shear stress required to move dislocations in a material is [26]

$$\Delta\tau = Gb\sqrt{c}\varepsilon^{3/2} \tag{1.6}$$

where c is the solute concentration and ε is the strain on the material caused by the solute. Increasing the concentration of the solute atoms will increase the yield strength of a material, but there is a limit to the amount of solute that can be added, and one should look at the phase diagram for the material and the alloy to make sure that a second phase is not created. In general, the solid solution strengthening depends on the concentration of the solute atoms, shear modulus of the solute atoms, size of solute atoms, valence of solute atoms (for ionic materials), and the symmetry of the solute stress field.

Precipitation hardening

In most binary systems, alloying more than solidus compositions in the equilibrium phase diagram will cause the formation of a second phase. A fine dispersion of second phase particles can also be created by mechanical or thermal treatments. The fine particles that compose the second phase formed by precipitation through aging act as pinning points to dislocation motion in a similar manner to solutes, though the particles are not necessarily single atoms.

The dislocations in a material can interact with the precipitate atoms in one of two ways in Fig. 1.6. If the precipitate atoms are small, the dislocations would cut through them. As a result, new surfaces, Fig. 1.6, of the particle would be exposed to the matrix

and the particle/matrix interfacial energy would increase. For larger or harder precipitate particles, looping or bowing of the dislocations would occur which results in dislocations getting longer.

Grain refinement

In grain refinement hardening, the grain boundaries act as pinning points impeding further dislocation propagation. Since the lattice structure of adjacent grains differs in orientation, it requires more energy for a dislocation to change directions and move into the adjacent grain. The grain boundary is also much more disordered than inside the grain, which also prevents the dislocations from moving in a continuous slip plane. Impeding this dislocation movement will hinder the onset of plasticity and hence increase the yield strength of the material. Under an applied stress, dislocations are generated by Frank-Read Sources [27]. Dislocations will move through a crystalline lattice until encountering a grain boundary, where the large atomic mismatch between different grains creates a repulsive stress field to oppose continued dislocation motion. As more dislocations propagate to this boundary, dislocation 'pile up' occurs as dislocations are unable to move past the boundary. Decreasing grain size decreases the amount of possible pile up at the boundary, increasing the amount of applied stress necessary to move a dislocation across a grain boundary.

There is an advantage to adopt grain refinement strengthening when compared to other strengthening methods. Other methods, work hardening, solid solution hardening and precipitation hardening are shown all decrease elongation and toughness, although strength is increased. In contrast, hardening by grain refinement does not have this undesirable effect. The effect of grain size on hardening by grain refinement can be

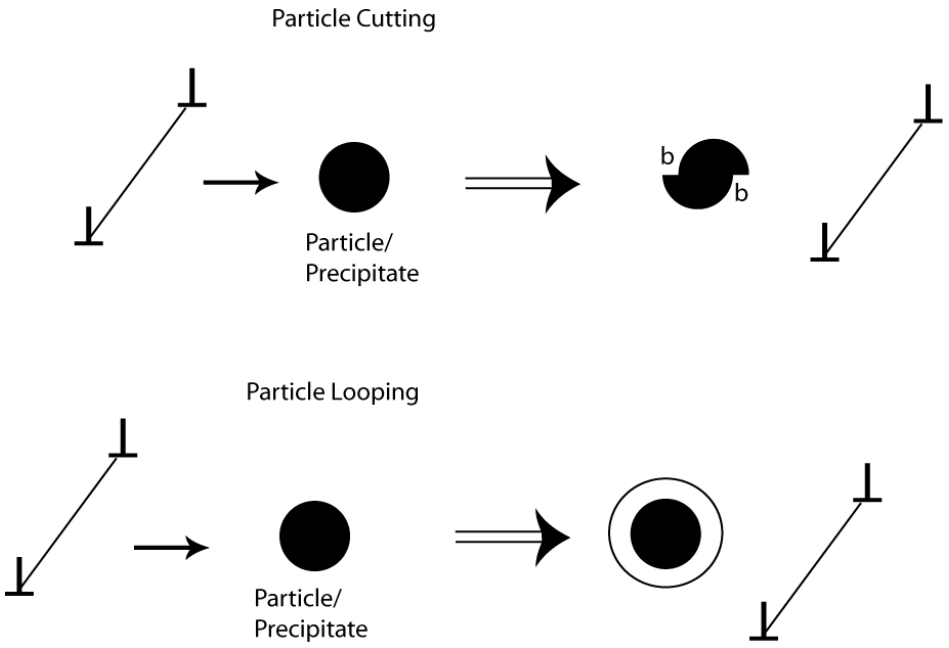

Figure 1.6. Dislocation interaction with particle.

expressed by the Hall-Petch relationship as given in Eq .1.1.

Strengthening of refractory metals by grain refinement

The metals of groups Va and VIa of the periodic system of elements are commonly called "refractory metals". They are vanadium, niobium and tantalum, and chromium, molybdenum and tungsten. They all have high melting points, Table 1.1, which is why their mechanical properties can be exploited to much higher temperatures than those of the common metals and alloys.

The majority of investigations about SPD process, both experimental and theoretical, have concentrated on metals with face-centered cubic (fcc) structures. In this regard, Al, Cu, Ni and its alloys have received maximum attention owing to the ease in making ultrafine- grain and nanocrystalline structure of these metals [28].

Much less publication can be found on processing and properties of ultrafine-grain and nanocrystalline structured metals with body-centered cubic (bcc) structures. It is well defined that the deformation mechanism and microstructure evolution of Cu, fcc structured, during HPT process [29]. In the case of bcc structured metals, only a few reports are available on processing and testing of ultrafine- grain and nanocrystalline structured Fe before 2004 [12].

The primary reason is believed to be the difficulty in producing fully dense bcc metal. Most representative bcc metals are refractory metals, and are very susceptible to interstitial impurities and their yield strength is usually higher than fcc structured metals, in Fig. 1.7. However, using HPT process, it is possible to produce ultrafine-grain and nanocrystalline structure because of its higher capacity for applying strain and suppressing the crack propagation during pressing when compared to other SPD process.

Table 1.1 Important physical properties and mechanical room-temperature properties of pure refractory metals [30].

Property	Group Va			Group VIa		
	V	Nb	Ta	Cr	Mo	W
Structure	b.c.c.	b.c.c.	b.c.c.	b.c.c.	b.c.c.	b.c.c.
Density (g/cm^3)	6.1	8.6	16.6	7.2	10.2	19.3
Melting point (°C)	1920 ± 20	2470 ± 20	3000 ± 30	1920 ± 20	2620 ± 20	3380 ± 20
Modulus of elasticity (GPa)	130–150	100–120	180–190	220–280	320–360	390–410
Poisson's ratio	0.37	0.40	0.34	0.21–0.28	0.30	0.30
Vickers hardness HV10;						
recrystallized (min.)	70	80	80	100	150	350
as-worked (max.)	200	200	200	300	500	650
Minimum UTS (MPa)						480 °C
recrystallized	300	300	300	300	550	600
DBTT (°C), bending						
recrystallized (min.)	−100	−200	−269	+200	−20	+400

Therefore, in the case of refractory metals, more investigation is needed. We will deal with deformation behavior, microstructure evolution and its mechanical properties after HPT process in Chapter. 2.

1.1.4. Strengthening due to both grain refinement and fine precipitation

Grain refinement is an important process to increase the strength of metallic materials. It is also well established that a fine dispersion of precipitate particles during aging enhances the strength of alloys. The general comments are already mentioned in Chapter 1.1.3. However, it is generally difficult to achieve combined effects of both grain refinement and fine dispersion of precipitates. This is because grain refinement to the submicrometer range is not easy in practice in alloys with supersaturated conditions using conventional thermo mechanical treatment. Provided that such a supersaturation is achieved in an ultrafine-grained alloy, another important task is to make fine precipitation within the fine grains by subsequent aging while keeping the grain size small.

The process of severe plastic deformation (SPD) offers a good opportunity for the grain refinement in any type of metallic materials regardless of internal states.

There are a few reports aiming at the combined effects of grain refinement with ECAP process and fine precipitation in age-hardenable alloys [32-39]. However, there is no publication about combining two strengthening methods both grain refinement and precipitation hardening after HPT process. HPT process is powerful method to generate small grains, defects and dislocations which can be used as pathway for diffusion. Post aging behavior after HPT process will be dealt with Chapter. 3.

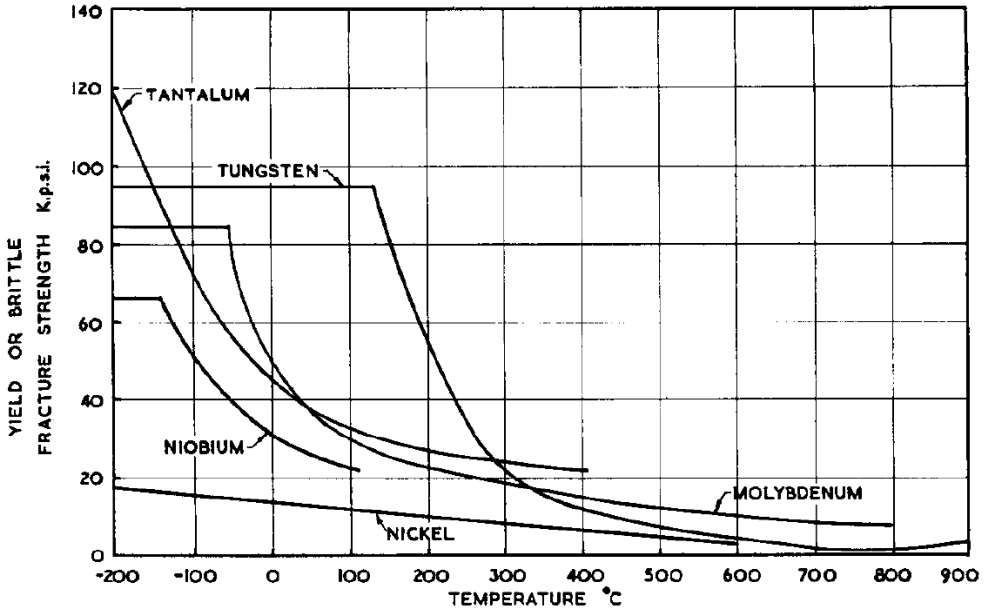

Figure 1.7. Effect of temperature on yield strength [31].

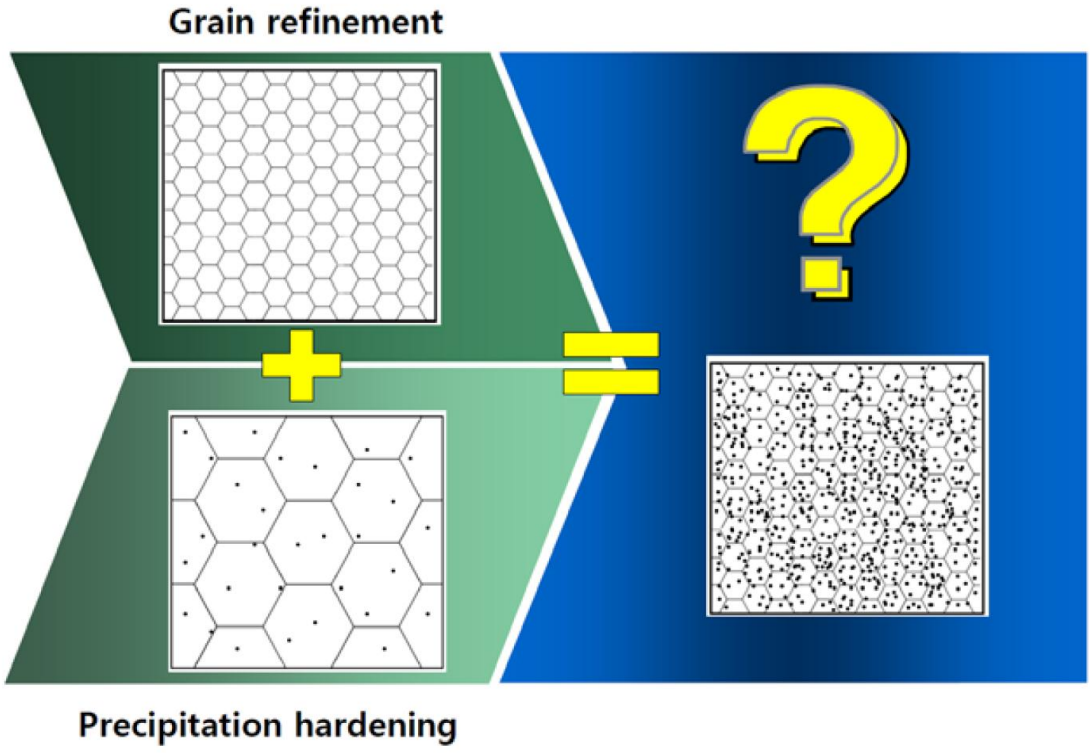

Figure 1.8. Concept of combining two different strengthening methods.

1.2. Objectives of thesis

HPT process has been applied to a wide range of metals and alloys for its large capacity of applicable strain. It gives a chance to produce ultrafine/ nano structured bcc refractory materials. It is well known that they are hard to deform with conventional deforming methods at room temperature.

Combining two different strengthening methods both grain refinement and precipitation hardening is very interesting field. It is not easy to predict the possibility of combining two methods because of grain coarsening.

In this present investigation, some bcc refractory metals are subjected to HPT process with various conditions. Their mechanical properties and microstructural evolutions are investigated. Age-hardenable alloys, Al-Ag alloy and Al 2091 and FeNi alloy are used to evaluate their annealing behavior after HPT processing.

References

1. E.O. Hall, Proc. Phys. Soc. London Sect. B 64 (1951) 747-753.

2. N.J. Petch, J. Iron Steel Inst. 173 (1953) 25-28.

3. R.Z. Valiev, R.K. Islamgaliev, I.V. Alexandrov, Prog. Mater. Sci. 45 (2000) 103-189.

4. M. Segal, V.I. Reznikov, A.E. Dobyshevskiy, V.I. Kopylov, Russian Metall. 1 (1981) 115-123.

5. Y. Iwahashi, J. Wang, Z. Horita, M. Nemoto, T.G. Langdon, Scripta Mater. 35 (1996) 143-146.

6. Y. Saito, N. Tsuji, H. Utsunomiya, T. Sakai, R.G. Hong. Scripta Mater. 39 (1998) 1221–1227.

7. P.W. Bridgman, Phys. Rev. 48 (1935) 825-847.

8. A. Vorhauer, R. Pippan, Scripta Mater. 51 (2004) 921-925.

9. R.Z. Valiev, Y.V. Ivanisenko, E.F. Rauch, B. Baudelet, Acta Mater. 44 (1996) 4705-4712.

10. S. Lee, K. Edalati, Z. Horita, Mater. Trans. 51 (2010) 1072-1079

11. S. Lee, Z. Horita, Mater. Trans. 53 (2012) 38-45.

12. Q. Wei, H.T. Zhang, B.E. Schuster, K.T. Ramesh, R.Z. Valiev, L.J. Kecskes, R.J. Dowding, L. Magness, K. Cho, Acta Mater. 54 (2006) 4079-4089.

13. K. Edalati, Z. Horita, Scripta Mater. 63 (2010) 174-177.

14. A.V. Korznikov, G. Tram, O. Dimitrov, G.F. Korznikova, S.R. Idrisova , Z. Pakiela, Acta Mater. 49 (2001) 663-671.

15. H. Shen, B. Guenther, A.V. Koanikov, R.Z. Valiev, Nunostruct. Mater. 6 (1995) 385-388.

16. R.Z. Valiev, R.S. Mishra, J. Groza, A.K. Mukherjee, Scripta Mater. 34 (1996) 1443-1448.

17. I.V. Alexandrov, Y.T. Zhu, T.C. Lowe, R.K. Islamgaliev, R.Z. Valiev, Metall. Mater. Trans. A 29 (1998) 2253-2260.

18. V.V. Stolyarov, Y.T. Zhu, T.C. Lowe, R.K. Islamgaliev, R.Z. Valiev, Mater. Sci. Eng. A 282 (2000) 78-85.

19. K. Edalati, Z. Horita, Scripta Mater. 63 (2010) 174-177.

20. A.R. Yavari, W.J. Botta, C.A.D. Rodrigues, C. Cardoso, R.Z. Valiev, Scripta Mater. 46 (2002) 711-716.

21. J. Sort, D.C. Ile, A.P. Zhilyaev, A. Concustell, T. Czeppe, M. Stoica, S. Surinach, J. Eckert, M.D. Baro, Scripta Mater. 50 (2004) 1221-1225.

22. Y. Harai, Y. Ito, Z. Horita, Scripta Mater. 58 (2008) 469-472.

23. K. Edalati, Z. Horita, J. Mater. Sci. 45 (2010) 4578-4582.

24. G.I. Taylor. Proc Roy Soc A145 (1934) 362-387.

25. U.F. Kocks, H. Mecking. Prog Mater Sci, 48 (2003) 171-273.

26. T. Kan, P. Haasen. Mater. Sci. Eng. A 5 (1970) 176-178.

27. W. T. Read Jr., Dislocations in crystals, McGraw-Hill Book Co. Inc., New York, 1953.

28. M.A. Meyers, A. Mishra, D.J. Benson, Prog. Mater. Sci. 51 (2006) 427-556.

29. K. Edalati, T. Fujioka, Z. Horita: Mater. Sci. Eng. A 497 (2008) 168-173.

30. E. Pink, R. Eck, In: Materials Science and Technology 8, Eds. R.W. Cahn, P. Haasen, E.J. Kramer, Ed. K. Matucha, VCH-Verlag, Weinheim-New York (1996) 589-641.

31. L. Northcott, J. Less-Common Metals 3 (1961) 125-148.

32. J.K. Kim, H.G. Jeong, S.I. Hong, Y.S. Kim, W.J. Kim, Scripta Mater. 45 (2001) 901-907.

33. Z. Horita, K. Ohashi, T. Fujita, K. Kaneko, T.G. Langdon, Adv. Mater. 17 (2005) 1599-1602.

34. E. Cerri, P. Leo, Mater. Sci. Eng. Mater. Sci. Eng. A 410–411 (2005) 226-229.

35. K. Ohashi, T. Fujita, K. Kaneko, Z. Horita, T.G. Langdon, Mater. Sci. Eng. A 437 (2006) 240-247.

36. W.J. Kim, J.Y. Wang, Mater. Sci. Eng. A 464 (2007) 23-27.

37. H.J. Roven, M. Liu, J.C. Werenskiold, Mater. Sci. Eng. A 483-484 (2008) 54-58.

38. V. Vidal, Z.R. Zhang, B. Verlinden, J. Mater. Sci. 43 (2008) 7418-7425.

39. T. Radeti, M. Popovi, E. Romhanji, B. Verlinden, Mater. Sci. Eng. A 527 (2010) 634-644.

Chapter 2. Production of ultrafine structured refractory metals by high-pressure torsion

2.1. Production of ultrafine structured group V metals in periodic table by high-pressure torsion

2.1.1. Introduction

Materials with small grain sizes have several advantages over their coarse-grained counterparts because they have higher strength and better ductility. The significance of grain refinement by severe plastic deformation (SPD) was recognized almost 2 decades ago [1]. Several methods were developed for the SPD process, which include equal-channel angular pressing (ECAP), high-pressure torsion (HPT), accumulative roll bonding (ARB), multi directional forging (MDF), cyclic extrusion and compression (CEC) and repetitive corrugation and strengthening (RCS) [2]. In particular, the HPT process produces grain sizes finer than the other processes [3] and it is possible to apply to hard materials and powder consolidation without heating process [4, 5]. The principle of the HPT processing is that the sample, in the form of a disk or a ring, is placed between two anvils which are rotated with respect to each other under application of compressive pressure, P, of several GPa to create a torsional strain in the sample [6]. Using the HPT process, researches were conducted on many face-centered cubic (fcc) metals and alloys [7, 8] including hexagonal-closed packed (hcp) metals and alloys [9]. However, except for Fe and its alloys, there are few researches on body-centered cubic (bcc) metals and alloys and thus, it should be worth investigating grain refinement

behavior of bcc structure materials using the HPT process.

There are twelve kinds of bcc metals according to periodic table. Among them, it is possible to apply practically the HPT process to 7 metals such as V^{23}, Cr^{24}, Fe^{26}, Nb^{41}, Mo^{42}, Ta^{73} and W^{74} in 5, 6 groups and 4, 5, 6 periods on the periodic table. For the other 5 bcc metals such as Na^{11}, K^{19}, Rb^{37}, Cs^{55} and Ba^{56}, it is not easy to apply the HPT process because they have low melting points and are susceptible to oxidation at room temperature. Although many reports are available for Fe [10-13], very limited applications have been reported on the bcc metals using the HPT process [14-19]. In this research, three bcc refractory metals in 5 group, V^{23}, Nb^{41}, and Ta^{73}, are selected.

2.1.2. Experimental materials and procedures

The materials used in this research were high purity V (99.9%), Nb (99.9%) and Ta (99.9%). They were purchased in a form of 10×10×1 mm^3 chips and these chips were rolled down to a thickness of 0.85 mm. Disks of 0.85mm thickness and 10 mm diameter were then cut by a wire-cutting electric discharge machine (EDM). The disks were processed by HPT under a selected pressure of 2, 4 and 6 GPa with 1/4, 1, 2 or 5 revolutions at a rotation speed of 1 rpm at room temperature. The alignment around the rotation axis of the upper and lower axes was adjusted to well within ±0.01 mm. Slippage between the disk and the anvils was measured after 1/4 revolutions as described in Ref [20, 21].

The disks were mechanically polished to a mirror-like surface and then the Vickers microhardness was measured along 12 radial directions at every 0.5 mm from the disk center to the edge. The average was calculated from the twelve separate measurements at the same distances from the center. The disk processed for 5

revolutions at each pressure was cut to two halves and polished to a mirror-like surface and the hardness measurements were further conducted across the thickness on the cross sectional plane at every 0.08 mm from one surface to the other. Each hardness measurement was conducted by using a load of 200 g for a duration time of 15 s.

After processing by HPT, the disks were mechanically polished to a thickness of ~0.50 mm and tensile specimens were cut from the polished disks using an electric discharge machine (EDM) at the 2mm off-center position as illustrated in Fig.2.1.1 with the dimensions of 1.5mm gauge lengths and 0.7mm widths. The tensile specimens were pulled to failure at a room temperature using a testing machine operating at a constant rate of cross-head displacement with the initial strain rate of 3.0×10^{-3} s^{-1}. The fracture surface was observed by a Keyence VE7800 scanning electron microscope (SEM) and Hitachi S-4300SE (FE-SEM) operating at 20 kV.

Disks with 3mm diameter were punched out from the center and edge parts of HPT-processed disks as illustrated in Fig.2.1.1. They were ground to a thickness of 0.15 mm and then thinned using a twin-jet electro-polishing facility in a solution of 90vol% CH_3COOH and 10vol% $HClO_4$ at room temperature with an application of 29 V for V, a solution of 4vol% H_2SO_4 and 96vol% CH_3OH at 263K with an application of 20 V for Nb and a solution of 5vol% H_2SO_4, 2vol%HF and 93vol%CH_3OH at 258K for Ta. The microstructures were observed using a Hitachi H-8100 transmission electron microscope (TEM) operating at 200 kV. Selected area electron diffraction (SAED) patterns were taken from regions having diameters of 6.3 μm.

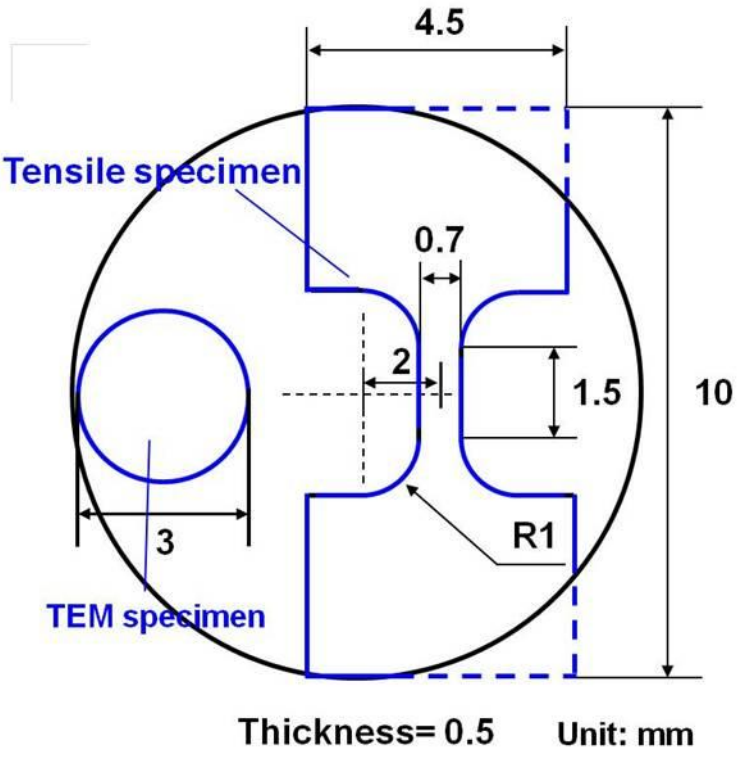

Figure 2.1.1. Dimensions of disk sample including positions for TEM disks and tensile specimen.

2.1.3. Results and discussions

2.1.3. (1) Hardness measurement

The average values of Vickers microhardness are plotted in Fig.2.1.2 as a function of the distance from the disk center after HPT processing for *N*= 1, 2 and 5 revolutions under the pressures of 2 and 6 GPa. For all V, Nb and Ta, Vickers microhardness increases with the distance from the disk center for all numbers of revolutions under both pressures but the hardness saturates to constant levels. In all cases, there is no changing in hardness after reaching the saturation level. Saturation levels are 240 Hv, 230Hv and 400Hv for V, Nb and Ta, respectively. These results are similar to Mo and V as described in chapter 2.2. The reason for this should be due to the difference in shear modulus. Earlier study showed that when hardness is plotted against equivalent strain divided by shear modulus, a universal plot is attained [23]. Thus under a given pressure, the sample with larger shear modulus requires more strain to reach a steady state than the sample with smaller shear modulus.

All Vickers microhardness values in Fig. 2.1.3 are plotted as a function of the equivalent strain in Fig. 2.1.3. Here, the following equation is used for the calculation of the equivalent strain [18].

$$\varepsilon = (1 - \mathrm{s}) \int_0^N \frac{2\pi r}{\sqrt{3}t(N)} dN \qquad (2.1.1)$$

where r is the distance from the disk center, N is the number of revolutions, s is the fraction of slippage and $t(N)$ is the disk thickness as a function of N during HPT processing. The value of s was measured at each pressure for all metals using a procedure as described earlier [18] and was found to be in the rage of 0.1 to 0.2. The

form of $t(N)$ was determined as a function of N by measuring the thicknesses after several different revolutions as in Ref. [9]. It is apparent that the microhardness data fall on a single curve. Microhardness increases with increasing equivalent strain at an initial stage of straining and saturates to steady-state levels at high strains where the hardness remains unchanged with further straining.

To investigate homogeneity of the HPT-processed disks, hardness measurement was conducted across the thickness on the cross sectional plane cut along the diameter of each disk. Figure 2.1.4 plots hardness against the distance from the disk surface at the disk center and at the distances of 2 and 4 mm located from the disk center.

Microhardness is almost constant across the thickness, although the hardness levels become higher with increasing distance from the disk center in consistence with hardness variations shown in Figs. 2.1.2 and 2.1.3. These results demonstrate that the samples after HPT processing are homogeneously deformed throughout the thickness at any location from the center.

2.1.3. (2) Tensile tests

Strain-stress curves are displayed in Fig. 2.1.5 for V, Nb and Ta from tensile testing conducted at room temperature with an initial strain rate of 3.0×10^{-3} s^{-1}. The tensile strength is significantly increased by the HPT processing in all materials when compared with the as-received conditions with an elongation to failure retained to some extent. It should be noted that V, Nb and Ta exhibit almost the same tensile strength for both pressures of 2 and 6 GPa and this is consistent with Figs. 2.1.2 and 2.1.3 where the hardness levels are the same once they reach the saturation.

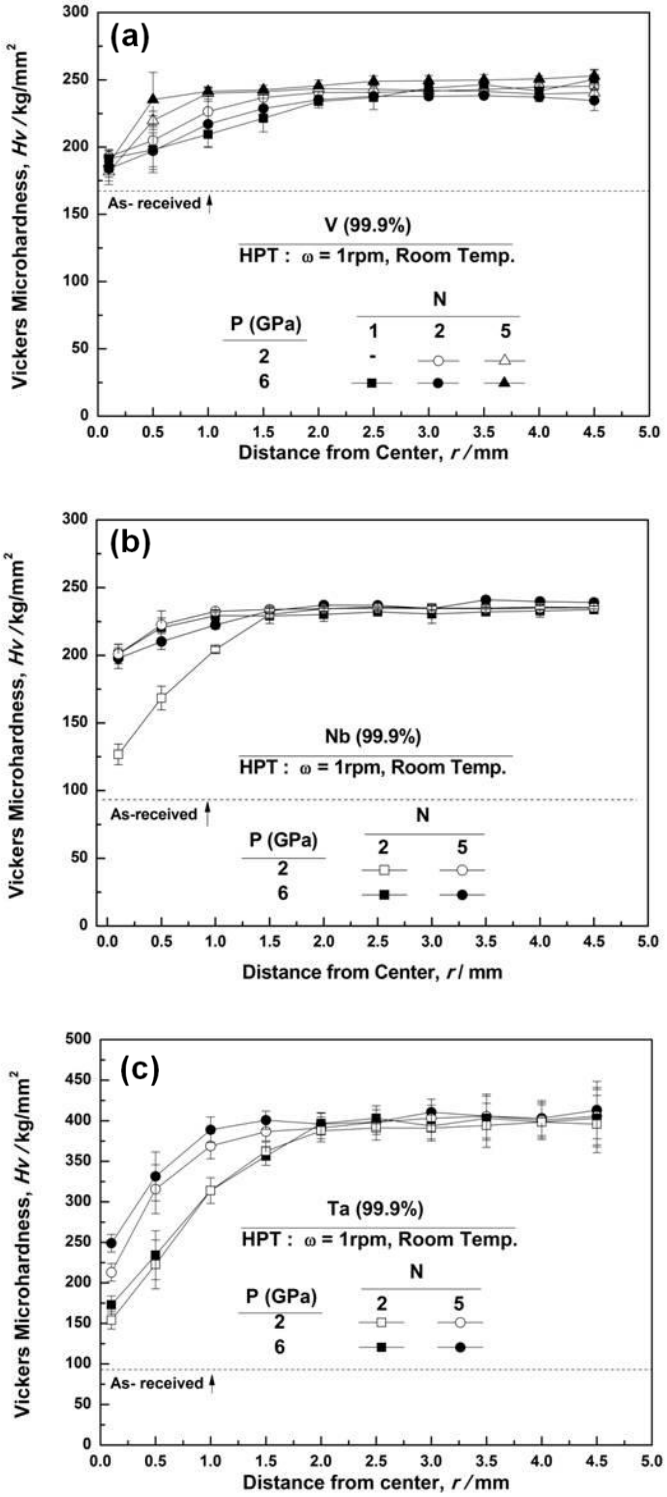

Figure 2.1.2. Vickers microhardness plotted against distance from center for V, Nb and Ta after HPT processing under 2 and 6 GPa for various revolutions.

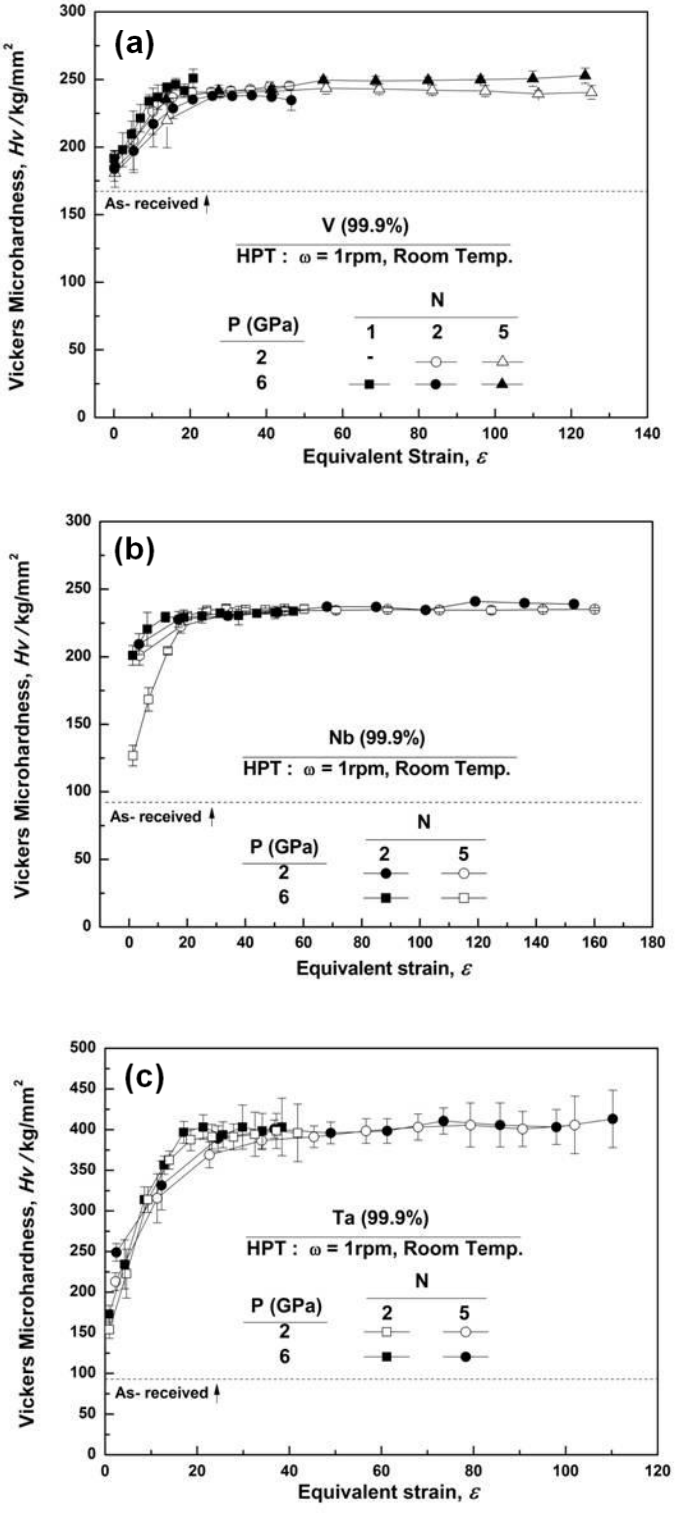

Figure 2.1.3. Vickers microhardness plotted against equivalent strain for V, Nb and Ta after HPT processing under 2 and 6 GPa for various revolutions.

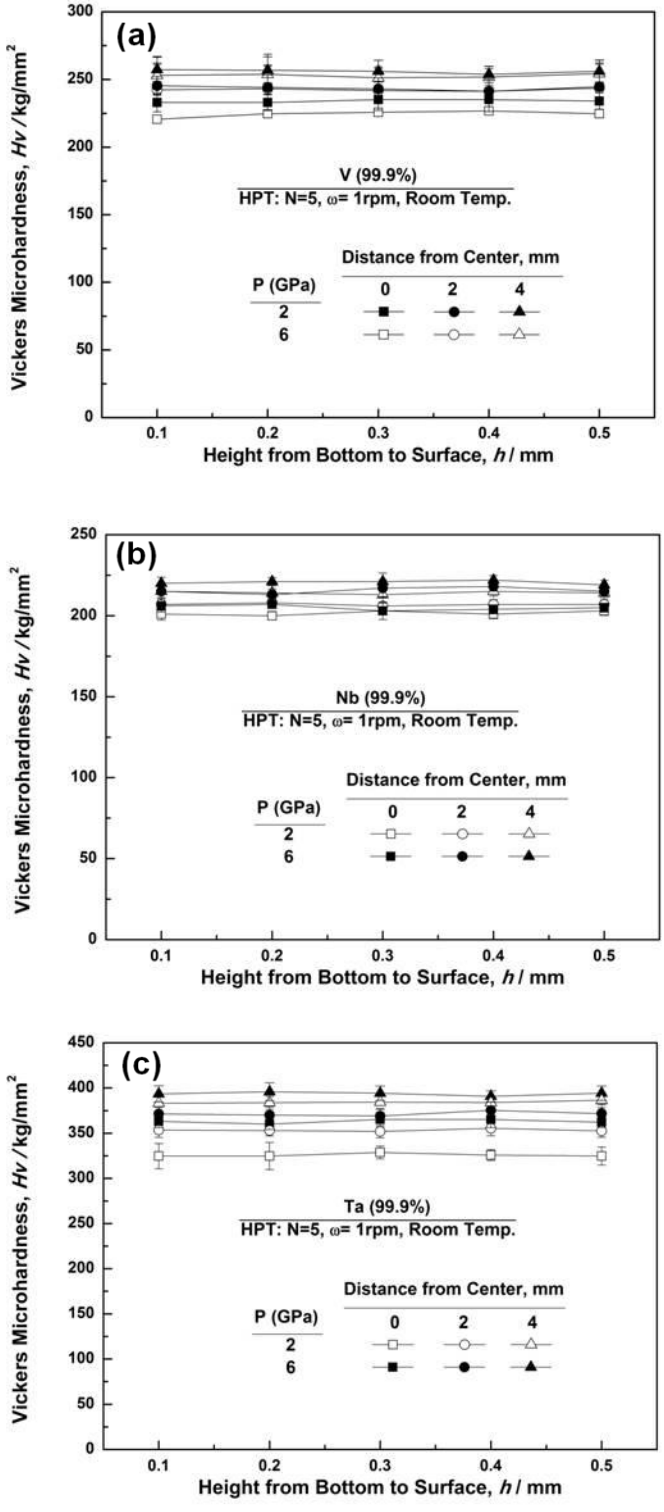

Figure 2.1.4. Vickers microhardness plotted against height from bottom on cross sectional plane for V, Nb and Ta.

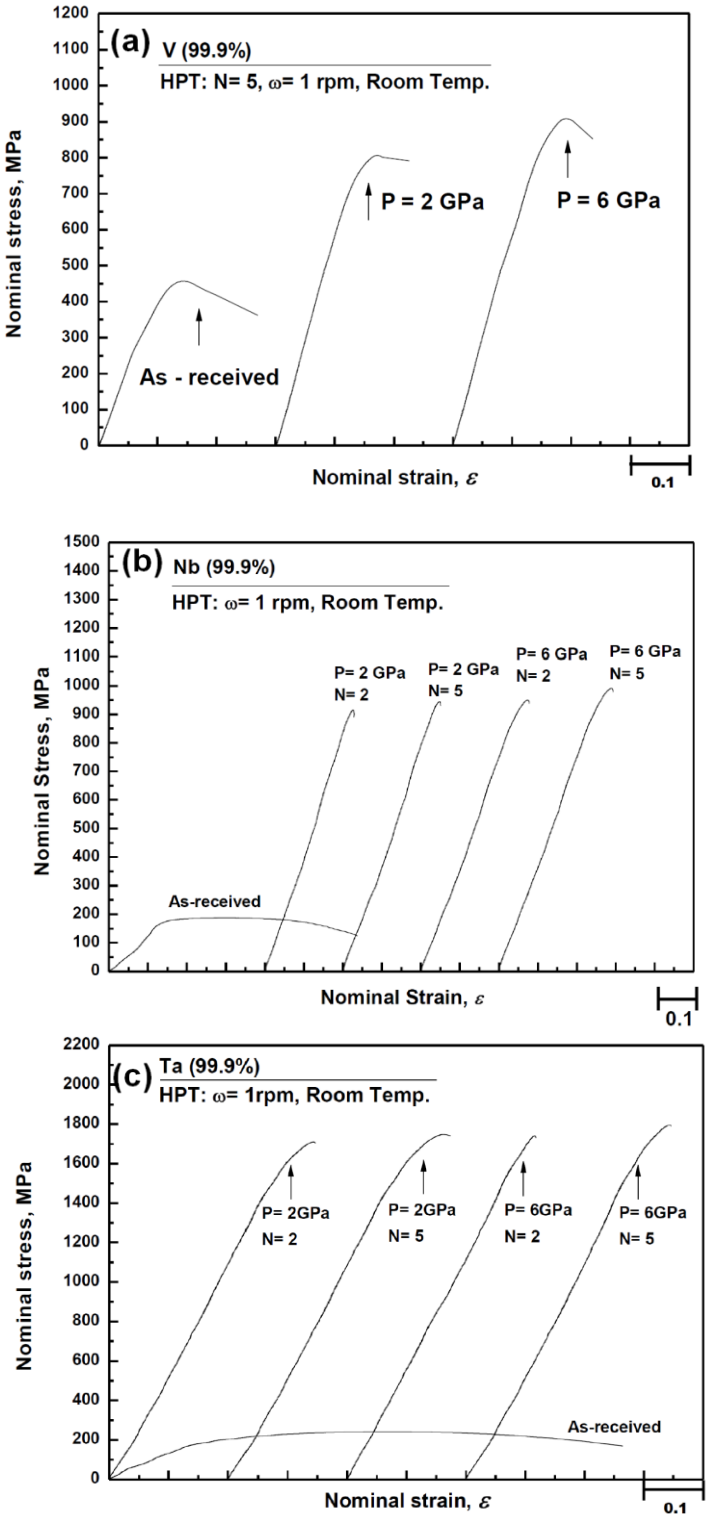

Figure 2.1.5. Nominal stress versus nominal strain curves for V, Nb and Ta under pressures of 2 and 6 GPa.

2.1.3. (3) Fractography

The fracture surfaces after tensile testing of individual specimens are shown in Figs. 2.1.6, 2.1.7 and 2.1.8 for V, Nb and Ta, respectively, where (a) corresponds to as-received specimen, (b) and (c) correspond to the specimens processed at 2 and 6 GPa. Higher magnification views are shown on the right side of the overall views of the fracture surfaces where the selected square regions correspond to the magnified images. Fractographs in Figs. 2.1.6, 2.1.7 and 2.1.8 shows that there appears to be little difference in the surface morphology between the samples as-received and processed at 2 and 6 GPa. HPT processed samples contain some regions having fine dimple structures on the fracture surfaces and these features are consistent with the stress-strain curves exhibiting some extent of ductility as shown in Fig. 2.1.5. It is considered that the fine structures after fracture appear to reflect ultrafine-grained structures produced by HPT processing.

2.1.3. (4) Transmission electron microscopy

Figures 2.1.9, 2.1.10 and 2.1.11 show TEM micrographs including SAED patterns of V, Nb and Ta processed for 5 revolutions under 2 and 6 GPa, respectively: in each figure, bright-field images on the left, dark-field images on the center and the SAED patterns on the right. The dark field images were taken with the diffracted beams indicated by arrows in the SAED patterns. The microstructures obtained under 2 GPa are shown in (a) N=2, (b) N=5 and those under 6 GPa are in (c) N=2, (d) N=5 for each of Figs. 2.1.9, 2.1.10 and 2.1.11. As illustrated in Fig. 2.1.1, the microstructures were taken from the edge parts of disks corresponding to the saturation of hardness. The grain size distributions are shown in Fig. 2.1.12 for V, Nb and Ta, respectively,

where Fig. 2.1.12 (a), (c) and (e) are for 2 GPa and Fig. 2.1.12 (b), (d) and (f) are for 6 GPa. The average grain sizes are given in Table 2.1.1. Grain size is decreased with increasing the applied pressure. Inspection of the SAED patterns indicates that the misorientation angle of the grain boundary increases with straining because the patterns tend to form rings. This is consistent with reports that the microstructure evolves from subgrains with low angle boundaries to grains with high angle boundaries with straining by severe plastic deformation [8].

2.1.4. Summary and Conclusions

Vickers microhardness data of V, Nb and Ta fall well on a single curve when they are plotted against equivalent strain. The hardness increases with strain and saturates to a constant level. TEM observation reveals that the grain size is reduced to 240~380 nm at the saturation level throughout the sample. The tensile test shows that the strength significantly increases with some ductility reserved. This ductility is consistent with the fractography showing the presence of fine dimples on the fracture surface.

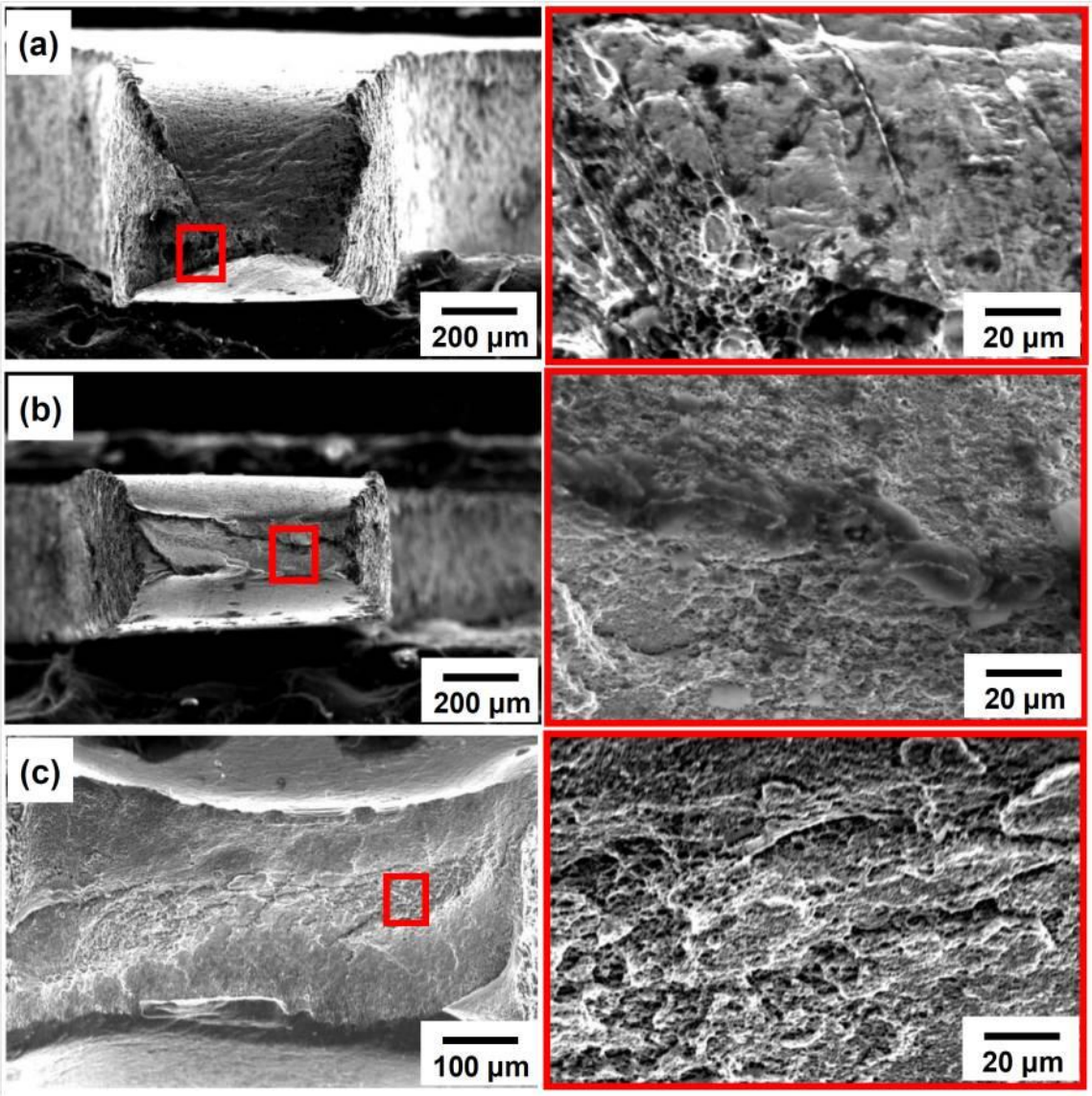

Figure 2.1.6. SEM fractographs for V: (a) As-received, (b) HPT under P=2 GPa and (c) HPT under P=6 GPa. Left: overall views. Right: magnified view from square areas in overall views.

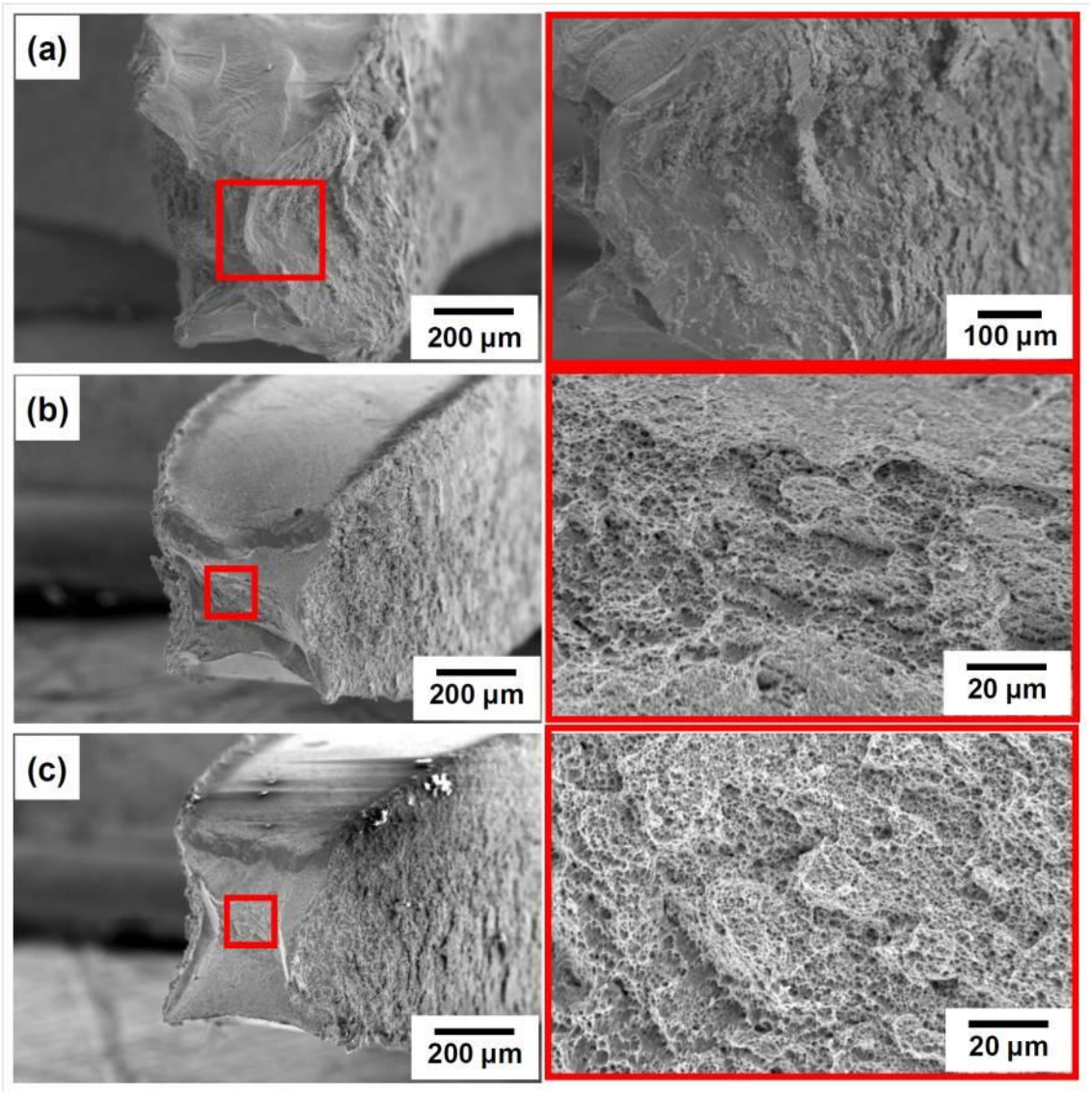

Figure 2.1.7. SEM fractographs for Nb: (a) As-received, (b) HPT under P=2 GPa and (c) HPT under P=6 GPa. Left: overall views. Right: magnified view from square areas in overall views.

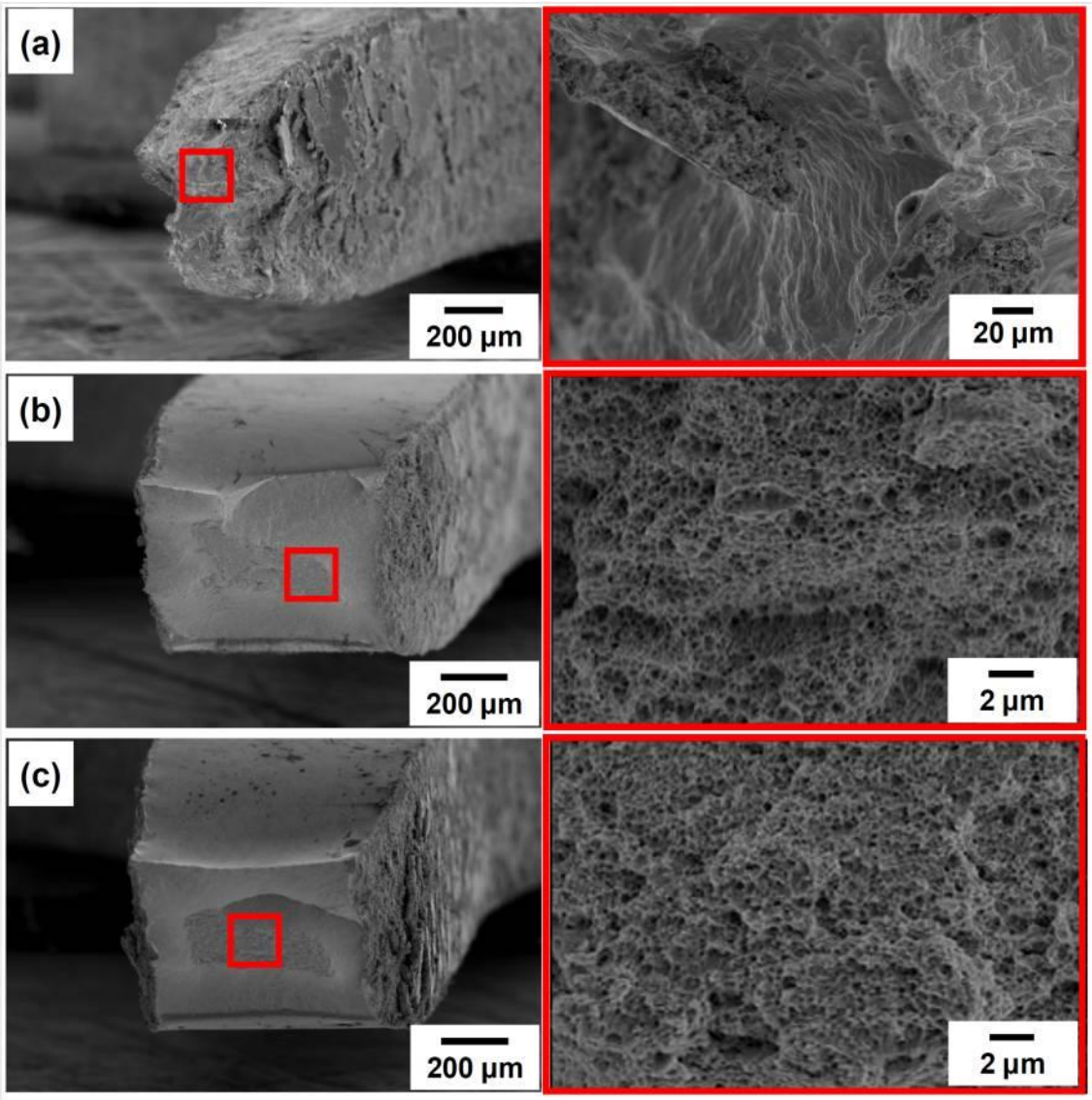

Figure 2.1.8. SEM fractographs for Ta: (a) As-received, (b) HPT under P=2 GPa and (c) HPT under P=6 GPa. Left: overall views. Right: magnified view from square areas in overall views.

Table 2.1.1 Grain sizes for V, Nb, and Ta after HPT process.

Pressure and revolution	V (99.9%)	Nb (99.9%)	Ta (99.9%)
P=2 GPa, N=5	380 nm	250 nm	330 nm
P=6 GPa, N=5	330 nm	240 nm	310 nm

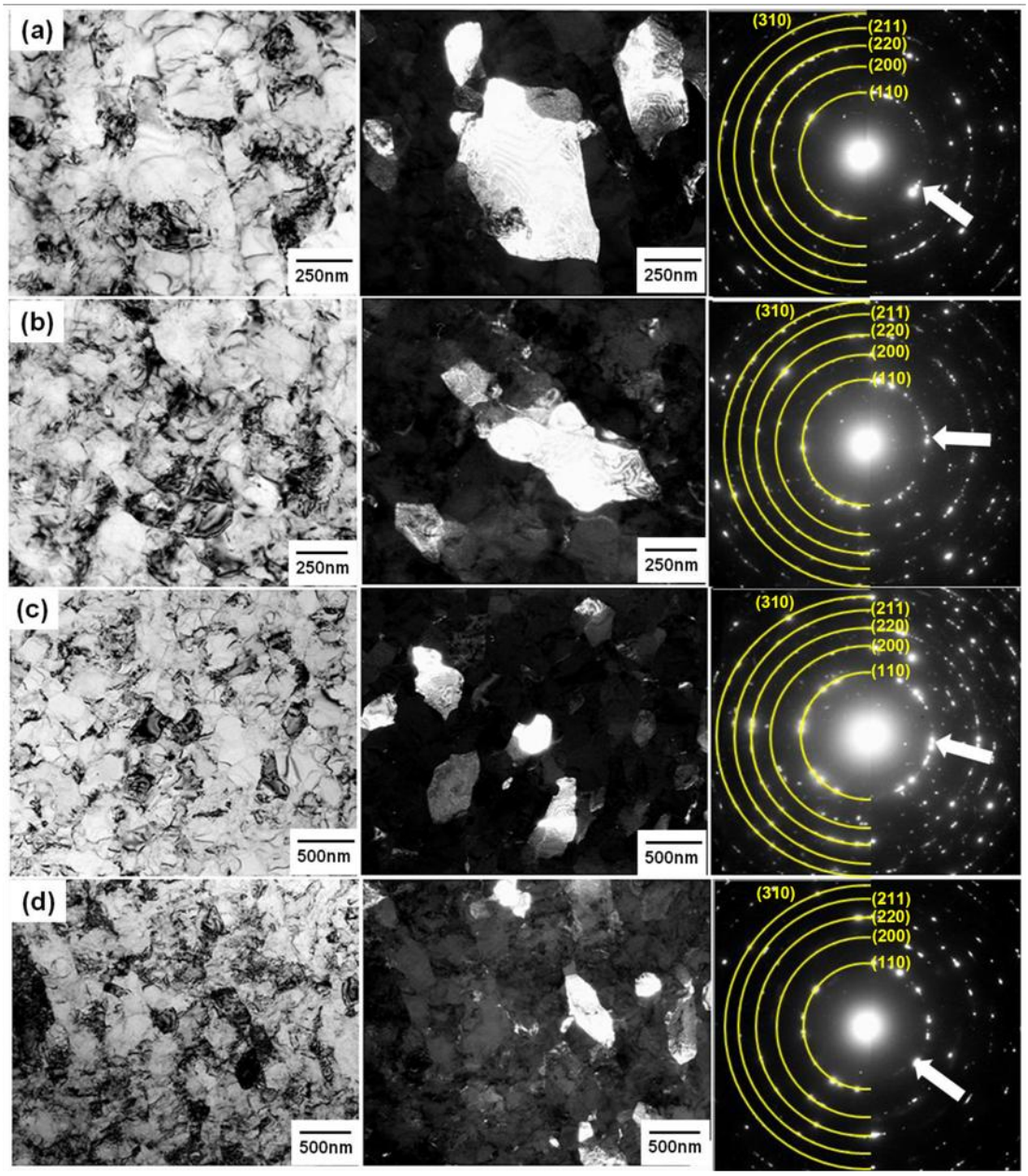

Figure 2.1.9. TEM micrographs and SAED patterns of V: under P= 2 GPa for (a) N=2 and (b) N=5 and under P= 6 GPa for (c) N=2 and (d) N=5.

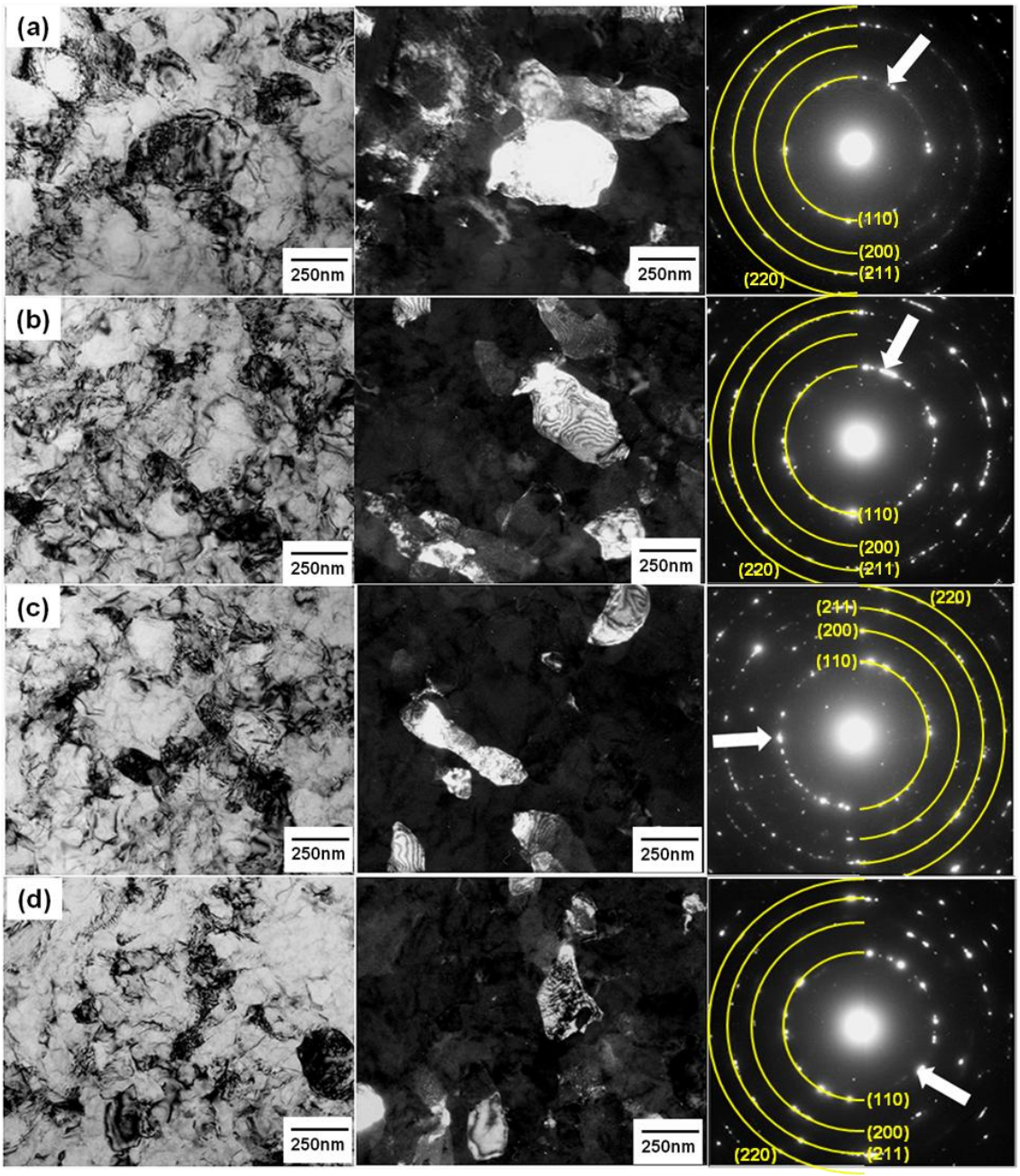

Figure 2.1.10. TEM micrographs and SAED patterns of Nb: under P= 2 GPa for (a) N=2 and (b) N=5 and under P= 6 GPa for (c) N=2 and (d) N=5.

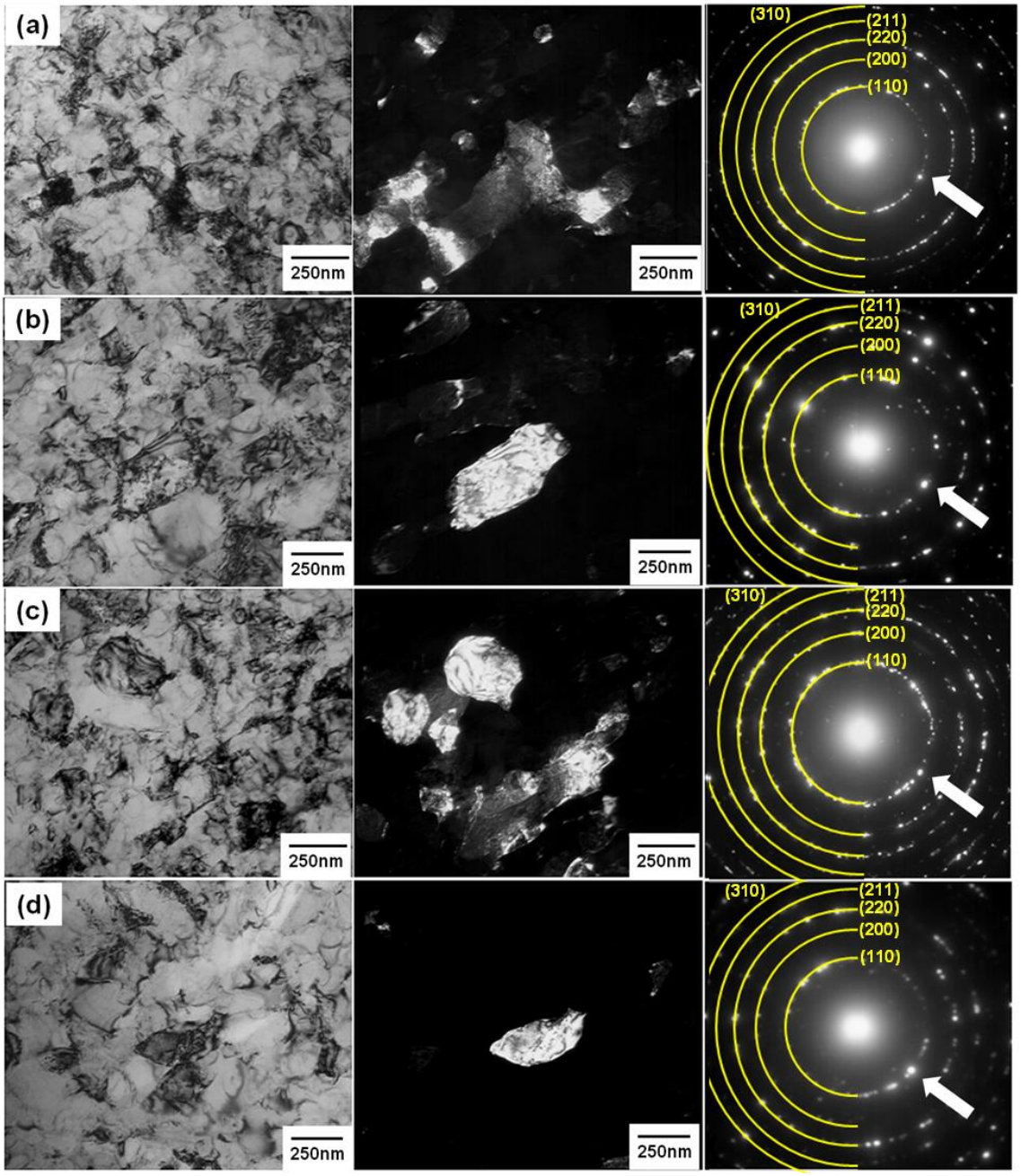

Figure 2.1.11. TEM micrographs and SAED patterns of Ta: under P= 2 GPa for (a) N=2 and (b) N=5 and under P= 6 GPa for (c) N=2 and (d) N=5.

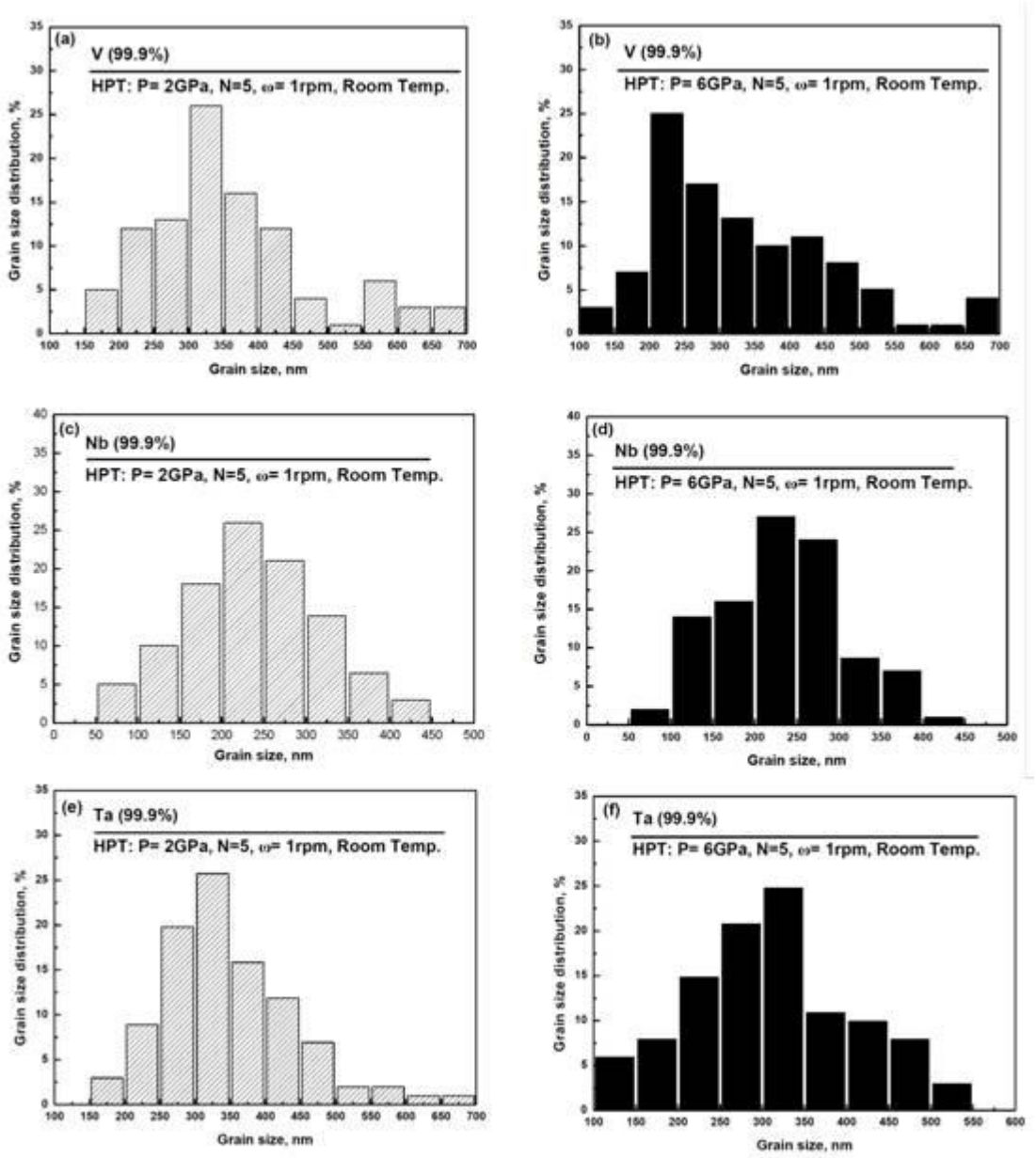

Figure 2.1.12. Grain size distribution of (a)(b) for V, (c)(d) for Nb, and (e)(f) for Ta.

References

1. R.Z. Valiev, R.K. Islamgaliev, I.V. Alexandrov, Prog. Mater. Sci. 45 (2000) 103-189.

2. R.Z. Valiev, Y. Estrin, Z. Horita, T. G. Langdon, M. J. Zehetbauer, Y. T. Zhu, JOM 58 (2006) 33-39.

3. G. Sakai, K. Nkamura, Z. Horita, T.G. Langdon, Mater. Sci. Forum 503-504 (2006) 391-396.

4. N.A. Smirnova, V.I. Levit, V.I. Pilyugin, R.I. Kuznetsov, L.S. Davydova, V. A. Sazonova, Fiz. Met. Metalloved. 68 (1986) 1170-1177.

5. T. Hebesberger, H.P. Stuwe, A. Vorhauer, F. Wetscher, R. Pippan, Acta Mater. 53 (2005) 393–402.

6. A. P. Zhilyaev, T. G. Langdon, Prog. Mater. Sci. 53 (2008) 893-979.

7. K. Edalati, T. Fujioka, Z. Horita, Mater. Sci. Eng. A 497 (2008) 168-173.

8. Y. Ito, Z. Horita, Mater. Sci. Eng. A 503 (2009) 32-36.

9. J. Čížek, I. Procházka, B. Smola, I. Stulíková, R. Kužel, Z. Matěj, V. Cherkaska, R.K. Islamgaliev, O. Kulyasova, Mater. Sci. Eng. A 462 (2007) 121-126.

10. K. Edalati, T. Fujioka, Z. Horita, Mater. Trans. 50 (2009) 44-50.

11. R. Z. Valiev, Yu. V. Ivanisenko, E. F. Rauch, B. Baudelet, Acta Mater. 44 (1996) 4705-4712.

12. Y. Todaka, M. Umemoto, J. Yin, Z. Liu, K. Tsuchiya, Master. Sci. Eng. A 462 (2007) 264-268.

13. F. Wetscher, A. Vorhauer, R. Pippan, Master. Sci. Eng. A 410-411 (2005) 213-216.

14. A.V Korznikov, S.Idrisova, N. I. Noskova, Phys. Met. Metall. 85 (1998) 327-331.

15. Y. R. Kolobov, B. Kieback, K. V. Ivanov, T. Weissgaerber, N. V. Girsova, Y. I. Pochivalov, G. Grabovetskaya, M. B. Ivanov, V. U. Kazyhanov, I. V. Alexandrov, Int. J.

Refract. Met. Hard Mater. 21 (2003) 69-73.

16. R. Wadsack, R. Pippan, B. Schedler, Fusion Eng. Des. 66–68 (2003) 265-269.

17. E.N. Popova, V.V. Popov, E.P. Romanov, V.P. Pilyugin, Phys. Met. Metall. 103 (2007) 407-413.

18. E.N. Popova, V.V. Popov, E.P. Romanov, V.P. Pilyugin, Phys. Met. Metall. 101 (2006) 52-57.

19. Q. Wei, H.T. Zhang, B.E. Schuster, K.T. Ramesh, R.Z. Valiev, L.J. Kecskes, R.J. Dowding, L. Magness, K. Cho, Acta Mater. 54 (2006) 4079–4089.

20. K. Edalati, T. Fujioka , Z. Horita, Mater. Trans. 50 (2009) 44-50.

21. K. Edalati, Z. Horita , T. G. Langdon, Scripta Mater. 60 (2009) 9-12.

22. K. Edalati, E. Matsubara, Z. Horita, Mater. Sci. Eng. A 40(2009) 2079-2086.

23. K. Edalati, Z. Horita, S. Yagi, E. Matsubara, Mater. Sci. Eng. A 523(2009) 277-281.

24. K. Edalati, Z. Horita, Y. Mine, Mater. Sci. Eng. A 527 (2010) 2136-2141.

2.2. Production of ultrafine structured group VI metals in periodic table by high-pressure torsion

2.2.1. Introduction

Ultrafine/ nano grained materials have advantages with higher strength and better ductility over their coarse-grained ones. In recent years, much effort has been devoted to develop grain refinement methods and investigating their unusual mechanical properties. Several methods using severe plastic deformation (SPD) have been developed for last 2 decades and typical examples are equal-channel angular pressing (ECAP), high-pressure torsion (HPT) and accumulative roll bonding (ARB) [1, 2].

The fundamental concept of HPT was introduced by Bridgman, where intense shear strain was imparted under high applied pressure [3]. In the HPT processing, a thin disk is subjected to compression and torsion to produce much larger strain than other SPD methods like ECAP and ARB. It has been demonstrated that HPT is effective to refine the grain size not only of conventional metallic materials but also of hard and brittle materials [4]. HPT has two advantages over other SPD processes: first, it tends to produce both smaller grain sizes and higher fractions of high-angle grain boundaries and second, it is applicable to hard and brittle materials because application of high pressure prevents cracks from initiation and propagation during processing. It is then anticipated that it can be applicable to hard materials such as refractory metals as investigated in this study [5-7].

HPT has been applied to many face-centered cubic (fcc) metals and alloys [8, 9] and also, applied to some hexagonal-closed packed (hcp) metals and alloys [10-13]. Application of SPD processing to body-centered cubic (bcc) metals and alloys is rather

few [5, 14-18], especially to the metals in Group V and VI which have high melting points. It is well known that they are all hard-to-deform metals with higher yield strengths. Although a few reports are available for SPD processing on Cr and Nb [17, 19-21], they focused on their thermal properties for example, ductile to brittle transition temperature and annealing behavior after SPD processing. This study aims to investigate evolution of mechanical properties and microstructures on two bcc metals, Cr and Mo after HPT processing.

2.2.2. Experimental Materials and Procedures

High purity Cr (99.9%) and Mo (99.9%) were received in the form of 10×10×1 mm^3 chips and these chips were ground mechanically to a thickness of 0.85 mm. The average grain size was determined using the linear intercept method and they were of 70 μm and 250 μm for Cr and Mo, respectively. These disks were cut with diameter of 10 mm by a wire-cutting electric discharge machine (EDM). The disks were subjected to HPT under a selected pressure of 2 and 6 GPa for 1/4, 1, 2, 3, 4, 5 or 10 revolutions with a rotation speed of 1 rpm at room temperature. The alignment around the rotation axis of the upper and lower axes was adjusted to well within ±0.01 mm for HPT process. Slippage between the disk and the anvils was measured after 1/4 revolutions using the procedure described in Ref. [18, 19].

Vickers microhardness was measured along 12 radial directions at every 0.5 mm from the disk center to the edge on mechanically polished surface. Averages were taken from the twelve measurements at the same distances from the disk center. The disks processed for 4 and 5 revolutions in Cr and 5 revolutions in Mo at each pressure were cut to two halves and polished the cross sectional plane to a mirror-like surface.

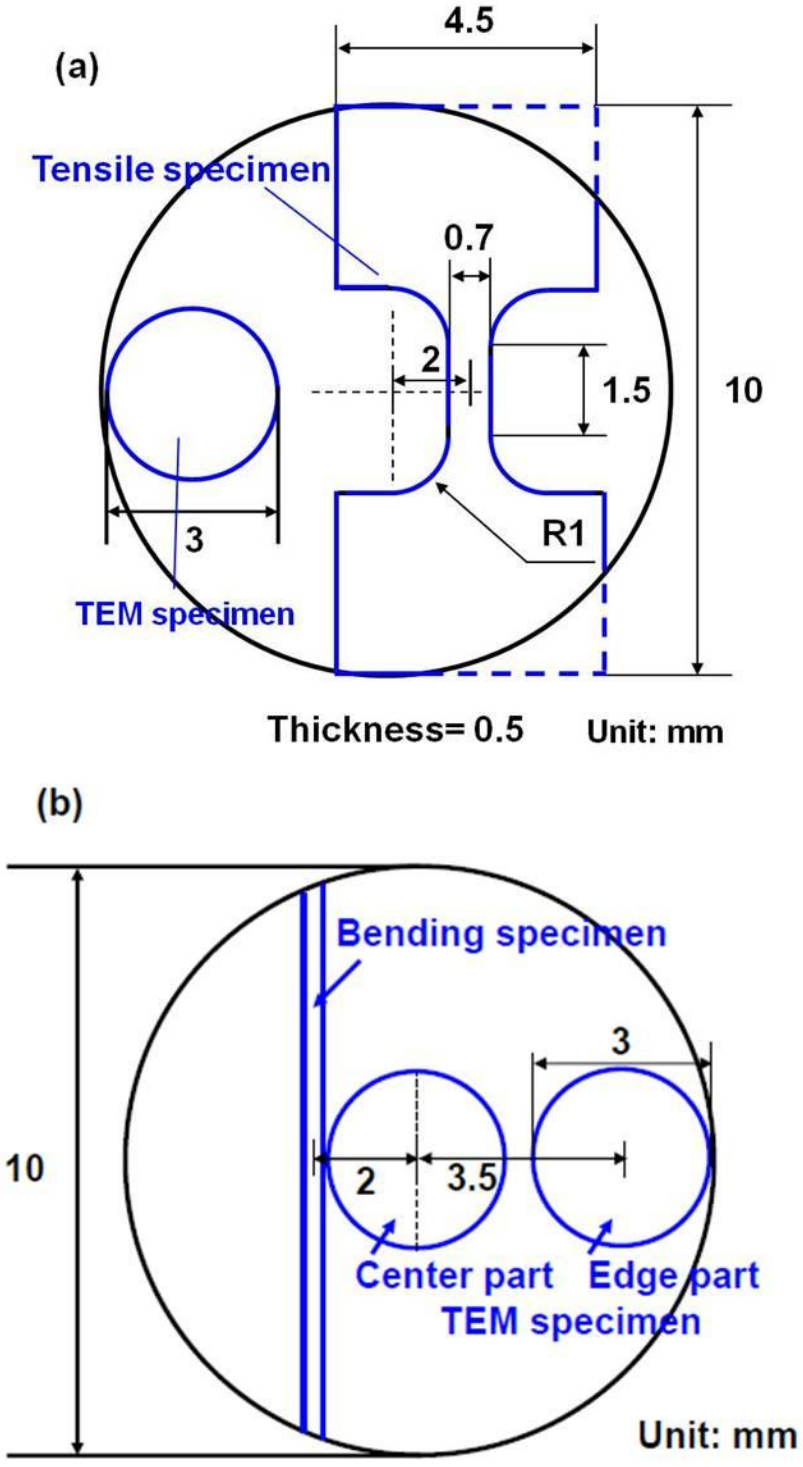

Figure 2.2.1. Dimensions of disk sample including positions for TEM disks and (a) tensile specimen and (b) bending specimen.

The hardness measurements were conducted across the thickness on the cross sectional plane at every 0.1 mm from one surface to the other. Each hardness measurement was conducted by using a load of 200 g for a duration time of 15 s.

After processing by HPT, the disks were mechanically polished to a thickness of ~0.50 mm and tensile specimens were cut from the polished disks using the EDM at the 2mm off-center position as illustrated in Fig. 2.2.1(a) with the dimensions of 1.5mm gauge lengths and 0.7mm widths. The tensile specimens were pulled to failure at room temperature using a testing machine operating at a constant rate of cross-head displacement with the initial strain rate of 3.0×10^{-3} s^{-1}.

In this study, bending tests were adopted to evaluate the ductility with inclusion of a compression mode. Bending specimens with dimensions of $0.5\times0.5\times9$ mm^3 rod were cut from the HPT-processed disks at the position 2 mm from the disk center as illustrated in Fig. 2.2.1(b). Three-point bending tests were conducted at room temperature with a cross-head speed of 0.5 mm/s using 8mm supporting span. Loading was undertaken toward the direction parallel to the pressing direction of the HPT samples. The bending stress σ was measured using the following Euler–Bernoulli beam theory [23]

$$\sigma = \frac{3Fl}{2wh^2} \tag{2.1.1}$$

where F is the bending load, l is the supporting span (8 mm), w and h are the width and length of the bending specimen (0.5 mm and 0.5 mm), respectively. With bending test, it is possible to apply compression component to sample, and therefore deformation in compression and tension is applied at the same time.

The fracture surfaces after the bending tests were observed using a Hitachi S-4300SE and JEOL JSM-5600 scanning electron microscope (SEM) operating at 20 kV.

Disks with 3mm diameter were punched out of the HPT-processed disks at 3.5 mm from the disk center as illustrated in Fig. 2.2.1(a) and (b). Samples for transmission microscopy (TEM) were made so as to represent the microstructures at midpoint of the thickness. They were ground to a thickness of 0.15 mm and then thinned using a twin-jet electro-polishing facility in a solution of 5vol% $HClO_4$ and 95vol% CH_3COOH at room temperature with an application of 10 V for Cr, and a solution of 10vol% H_2SO_4 and 90vol% CH_3OH at 253K with an application of 13.5 V for Mo. The microstructures were observed using a Hitachi H-8100 transmission electron microscope operating at 200 kV. Selected area electron diffraction (SAED) patterns were taken from regions having diameters of 6.3 μm.

2.2.3. Results and discussions

2.2.3. (1) Hardness measurement

The average values of Vickers microhardness are plotted in Fig. 2.2.2 as a function of the distance from the disk center after HPT processing for N= 1, 2, 3, 4, 5 or 10 revolutions under the pressures of 2 and 6 GPa. For both Cr and Mo, Vickers microhardness increases with the distance from the disk center for all numbers of revolutions under both pressures but the hardness saturates to constant levels. The hardness level at the saturation appears to be dependent on the applied pressure in Mo while it is almost the same in Cr irrespective of the pressure. In both cases, there is no changing in hardness after reaching the saturation level. Recent study showed that when hardness is plotted against equivalent strain divided by shear modulus, a universal

plot is attained [24]. Thus under a given pressure, the sample with larger shear modulus requires more strain to reach a steady state than the sample with smaller shear modulus. All Vickers microhardness values in Fig. 2.2.2 are plotted as a function of the equivalent strain in Fig. 2.2.3. Here, the following equation is used for the calculation of the equivalent strain [18].

$$\varepsilon = (1 - s) \int_0^N \frac{2\pi r}{\sqrt{3} t(N)} dN \qquad (2.2.2)$$

where r is the distance from the disk center, N is the number of revolutions, s is the fraction of slippage and $t(N)$ is the disk thickness as a function of N during HPT processing. The value of s was measured at each pressure for both metals using a procedure as described in Ref. [18] and was found to be in the rage of 0.1 to 0.2. The form of $t(N)$ was determined as a function of N by measuring the thicknesses after several different revolutions as in Ref. [9].

In the case of Cr, it is apparent that the microhardness data fall on a single curve. Microhardness increases with increasing equivalent strain at an initial stage of straining and saturates to steady-state levels at high strains where the hardness remains unchanged with further straining. Close examination reveals that the levels obtained at the applied pressures of 2 GPa and 4 GPa tend to increase with straining although the increase is very gradual. This suggests that, when the applied pressure is low, the microstructure gradually evolves with straining and reaches a steady state where a balance between hardening and softening is established as described in a report [19]. It should be noted that the evolution under the higher pressure of 6 GPa is similar to the one obtained in Cu, Fe and other metals and alloys [7, 10]. It is considered that the slow

evolution of hardness at the lower pressures can be due to insufficiency of the pressure when compared with Cr.

To check homogeneity of the HPT-processed disks, hardness measurement was conducted across the thickness on the cross sectional plane cut along the diameter of each disk. Figure 2.2.4 plots hardness against the distance from the disk surface at the disk center and at the distances of 2 and 4 mm located from the disk center. Microhardness is almost constant across the thickness, although the hardness levels become higher with increasing distance from the disk center in consistence with hardness variations shown in Figs. 2.2.2 and 2.2.3. These results demonstrate that the samples after HPT processing are homogeneously deformed throughout the thickness at any location from the center.

2.2.3. (2) Transmission electron microscopy

TEM micrographs are summarized in Figs. 2.2.5 and 2.2.6 including SAED patterns for Cr and Mo after HPT processing, respectively: in each figure, bright-field images on the left, dark-field images on the center and SAED patterns on the right. The dark field images were taken with the diffracted beams indicated by arrows in the SAED patterns. The microstructures obtained under 2 GPa are shown in Fig. 2.2.5 (a) and (b) for 2 and 5 revolutions and those under 6 GPa are in (c) and (d) for 2 and 4 revolutions in Cr. In the case of Mo, as illustrated in Fig. 2.2.1(b), the microstructures were taken from the center parts and edge parts of disks and they are shown in (a) and (c) for the center parts and in (b) and (d) for the edge parts for each of Fig. 2.2.6. The microstructures were taken from the regions corresponding to the steady-state, which are at 3 mm away from the disk center.

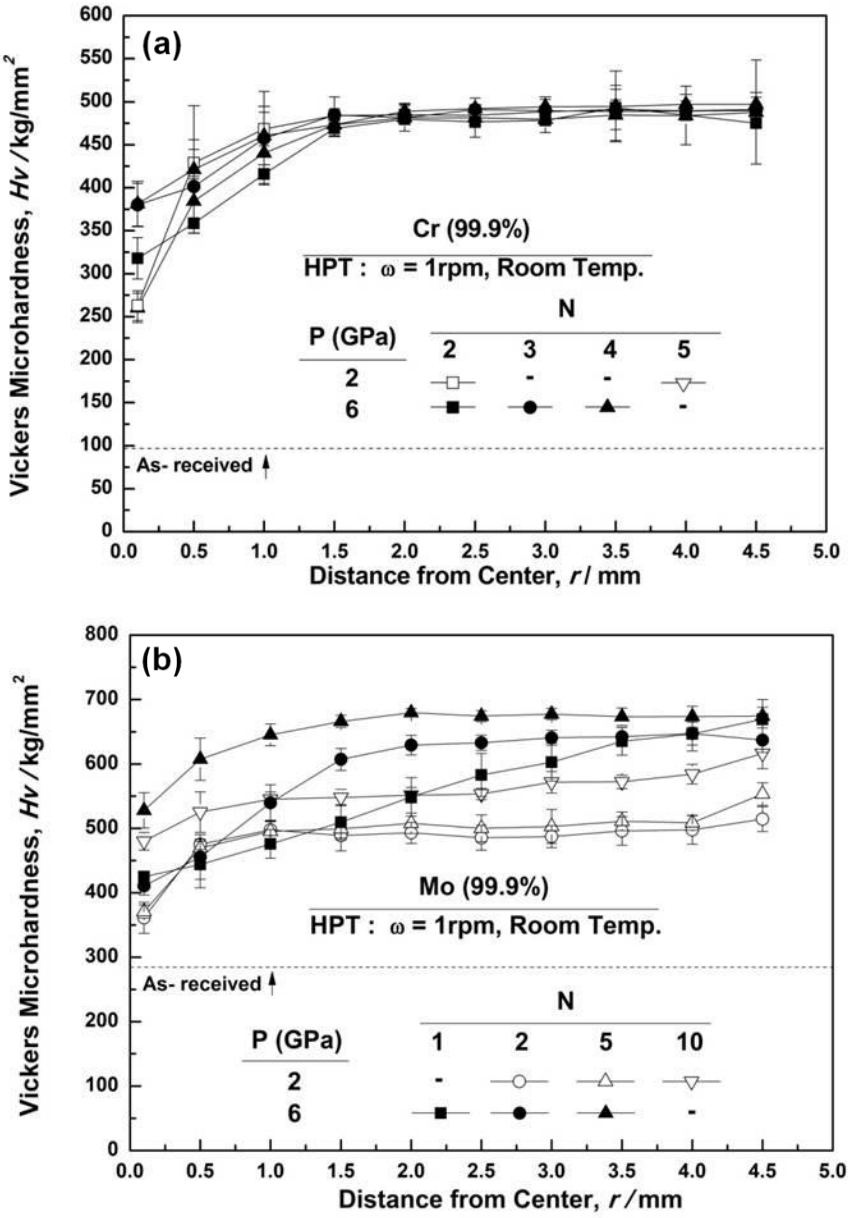

Figure 2.2.2. Vickers microhardness plotted against distance from center for Cr and Mo after HPT processing under 2 and 6 GPa for various revolutions.

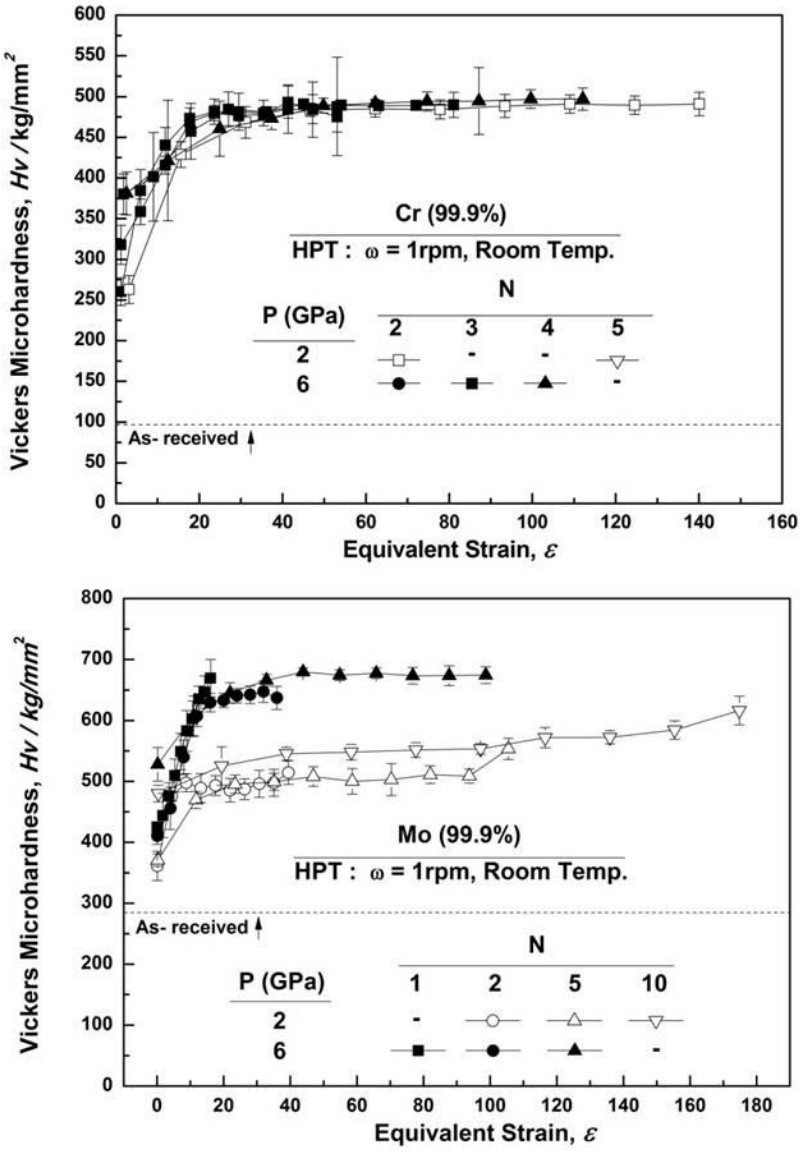

Figure 2.2.3. Vickers microhardness plotted against equivalent strain for Cr and Mo after HPT processing under 2 and 6 GPa for various revolutions.

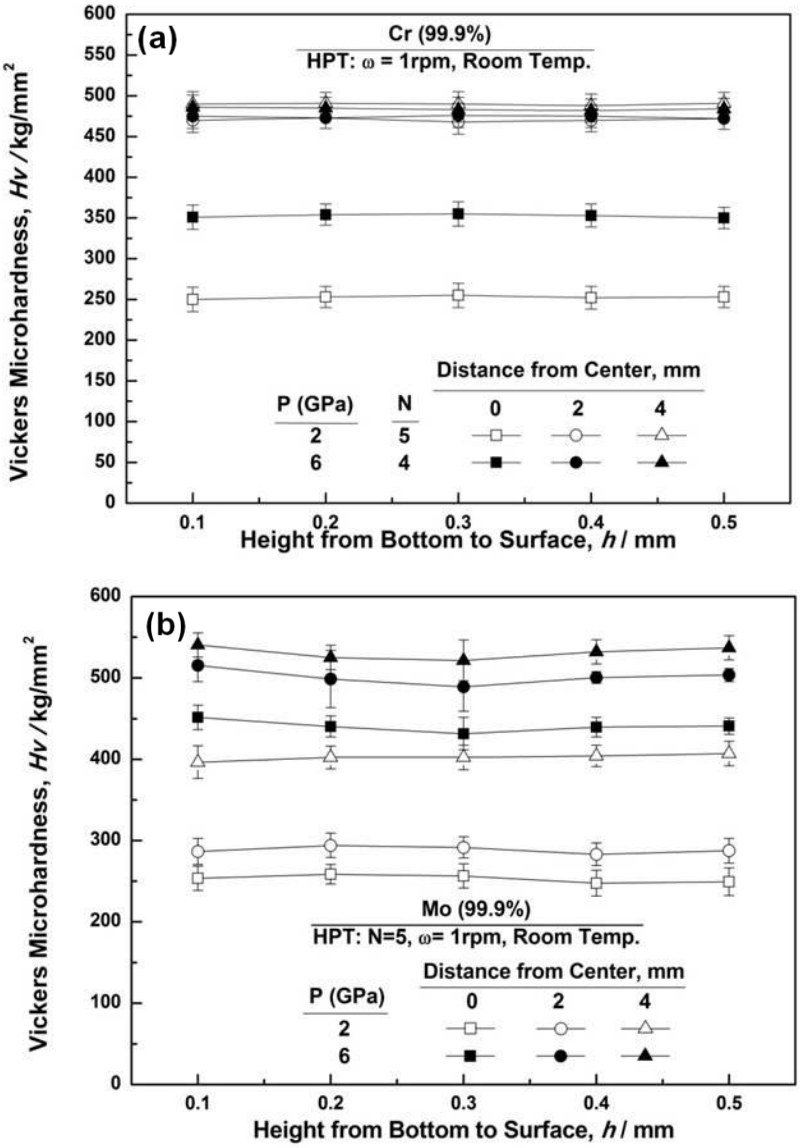

Figure 2.2.4. Vickers microhardness plotted against height from bottom on cross sectional plane for (a) Cr and (b) Mo.

The microstructures were taken from the regions corresponding to the steady-state, which are at 3 mm away from the disk center. The grain size distributions are shown in Figs. 2.2.7 and 2.2.8 at each HPT condition in Cr and Mo, respectively, where (a), (b) is for 2 GPa and (c), (d) for 6 GPa. The average grain sizes and standard deviations are summarized in Table 2.2.1. The grain size was obtained from the dark-field images as in Figs. 2.2.5 and 2.2.6 where the two orthogonal axes of the bright areas were measured for a total of more than 100 grains.

With these results, it is found that the average grain size becomes slightly smaller with increasing pressure and increasing number of revolutions. Inspection of the SAED patterns shows also that the misorientation angle of the grain boundary increases with shear straining because the patterns tend to form a net type under 2 GPa in both metals as shown in Figs. 2.2.5(a) and 2.2.6(a). Thus, the microstructures after processing by HPT under 2 GPa for 2 revolutions consists of grains with low angle boundaries (subgrains) with the average sizes of ~250 nm in Cr. In Figs. 2.2.5(b), (c) and (d), and 2.2.6(c) and (d), ring types of SAED patterns form and thus the angles between two neighboring grains becomes high. The grain size decreases to the size of ~200 nm in Cr and ~350 nm in Mo with many dislocations within the grains. Inspection of the SAED patterns indicates that the misorientation angle of the grain boundary increases with straining because the patterns tend to form a net at the center part and a ring at the edge part. This is consistent with reports that the microstructure evolves from subgrains with low angle boundaries to grains with high angle boundaries with straining by severe plastic deformation [9].

In Figs. 2.2.5(b), (c), (d) and 2.2.6(c), (d), ring types of SAED patterns form and thus the angles between two neighboring grains becomes high.

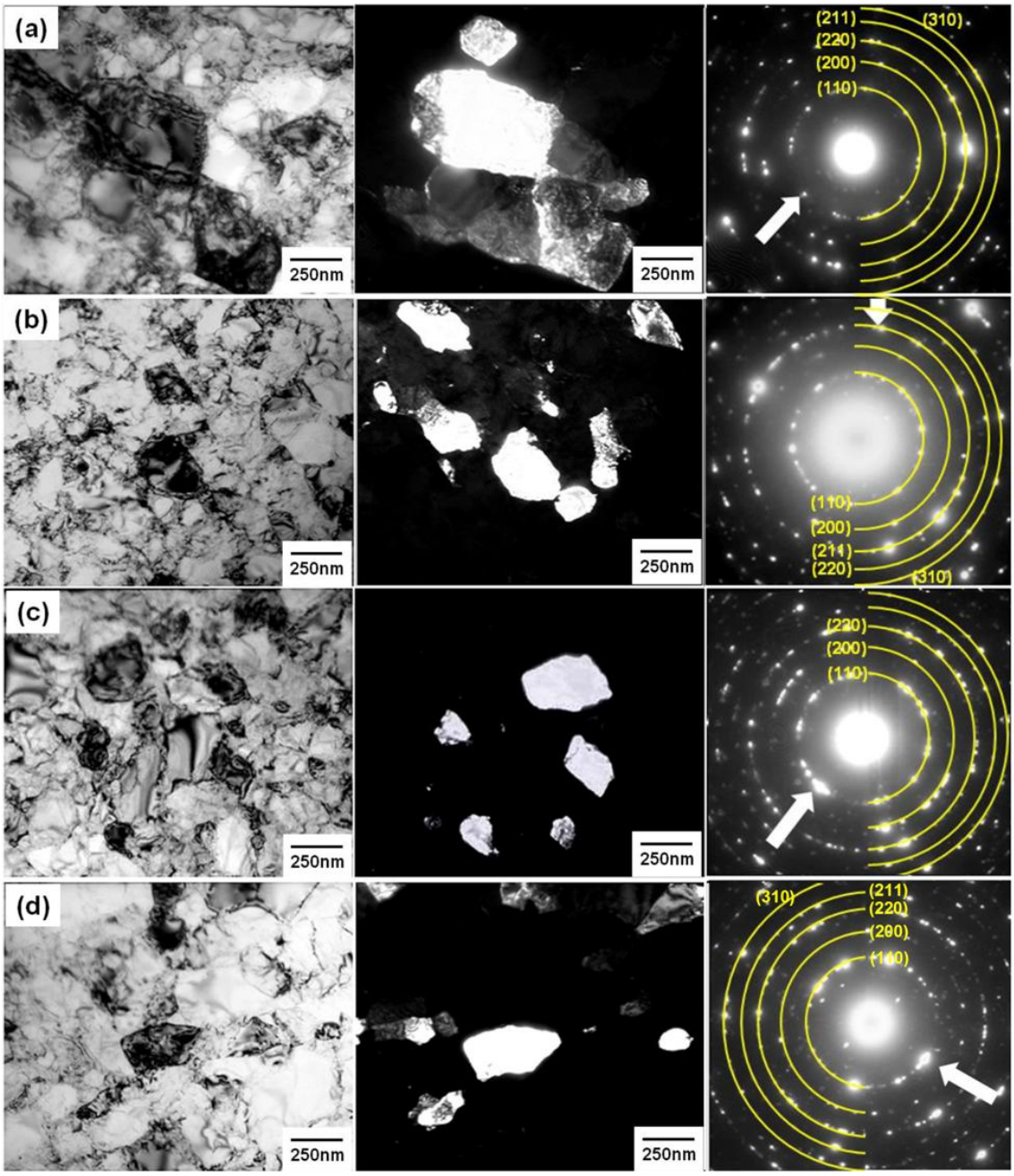

Figure 2.2.5. TEM micrographs and SAED patterns of Cr: under P= 2 GPa for (a) 2 revolutions and (b) 5 revolutions, and under P= 6 GPa for (c) 2 revolutions and (d) 4 revolutions.

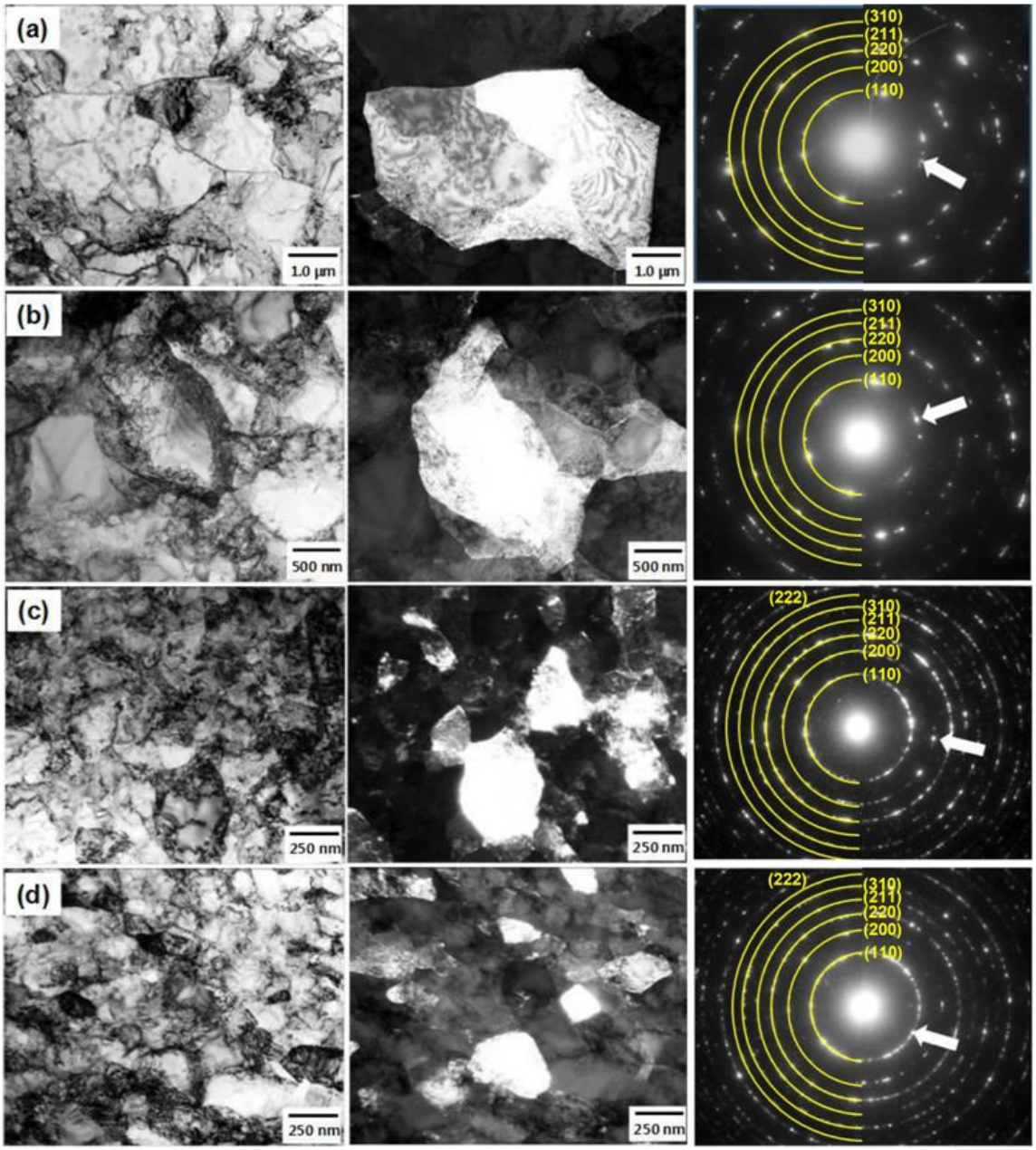

Figure.2.2.6.TEM micrographs and SAED patterns of Mo: after 5 revolutions under P= 2 GPa near (a) center part and (b) edge part, and under P= 6 GPa near (c) center part and (d) edge part.

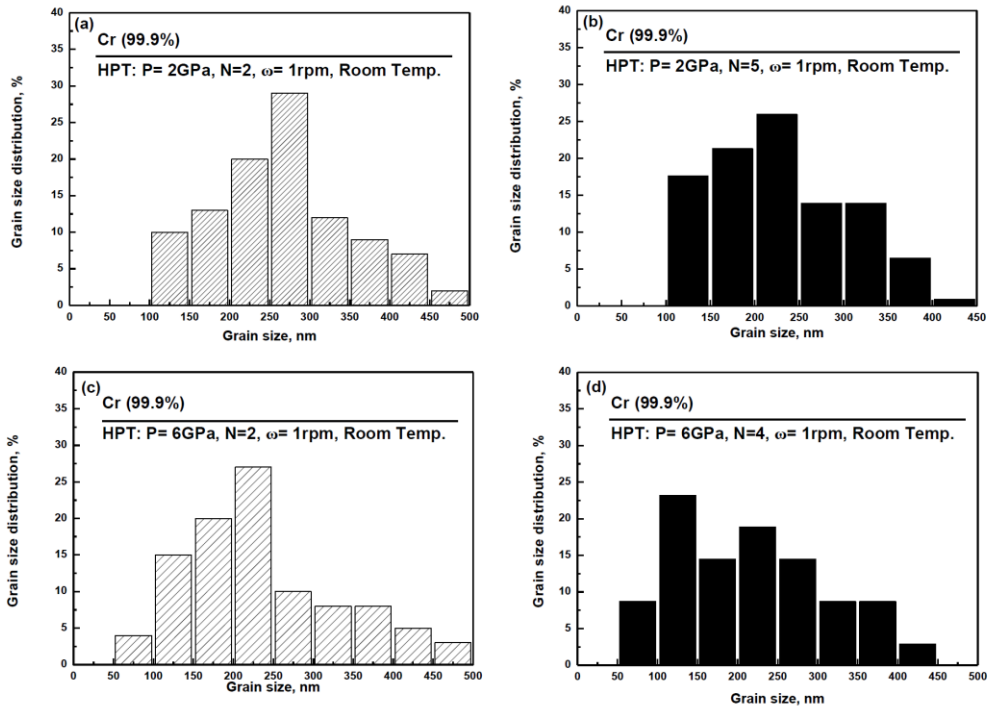

Figure 2.2.7. Grain size distribution of Cr: under P= 2 GPa for (a) 2 revolutions and (b) 5 revolutions, and under P= 6 GPa for (c) 2 revolutions and (d) 4 revolutions.

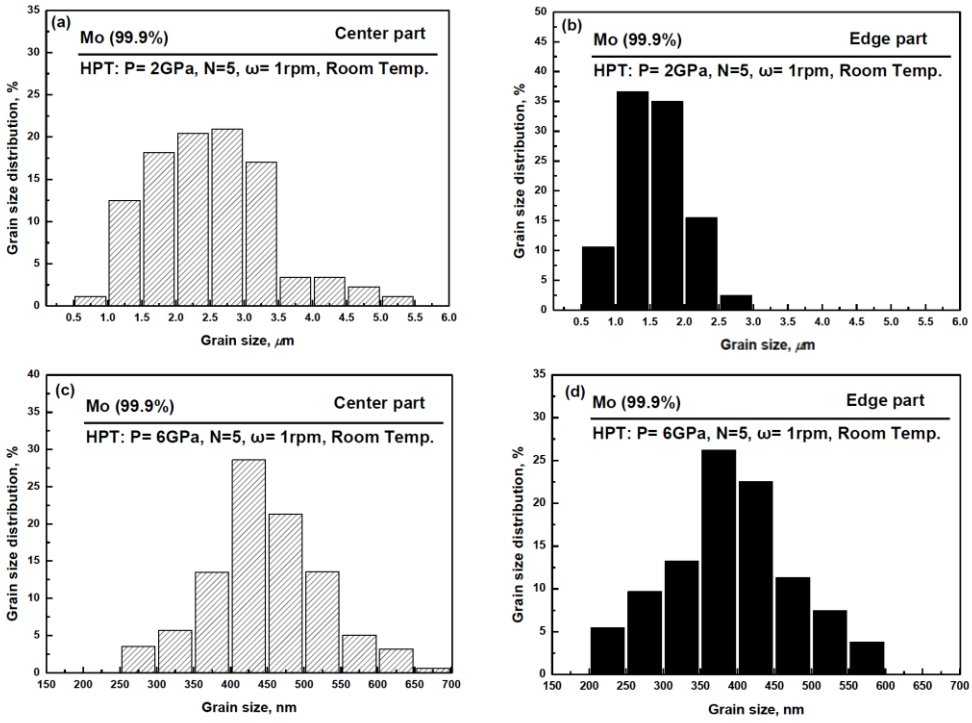

Figure 2.2.8. Grain size distribution of Mo: under P= 2 GPa with 5 revolutions for (a) center part and (b) edge part, and under P= 6 GPa with 5 revolutions for (c) center part and (d) edge part.

Table 2.2.1 Grain sizes for Cr and Mo after HPT process.

Pressure (P)	2 GPa		6 GPa		
Revolution (N)	2	5	2	4	5
Cr (99.9%)	240nm	210 nm	220nm	200nm	-
Mo (99.9%)	-	1,580 nm	-	-	340 nm

The grain size decreases to the size of ~200 nm in Cr and ~350 nm in Mo with many dislocations within the grains. Inspection of the SAED patterns indicates that the misorientation angle of the grain boundary increases with straining because the patterns tend to form a net at the center part and a ring at the edge part. This is consistent with reports that the microstructure evolves from subgrains with low angle boundaries to grains with high angle boundaries with straining by severe plastic deformation [9].

Comparison of the microstructures between Cr and Mo indicates that the effect of the applied pressure is different: it is little on Cr so that the microstructure including the grain size formed at 2 GPa is almost the same as the one formed at 6 GPa, but the difference is significant between the two pressures in Mo. It is apparent that subgrain structures well develop not only in the center part but also in the edge part in Mo under the pressure of 2 GPa and the grain size is more than 5 times larger under 2 GPa than 6 GPa. This microstructural observation is in accordance with the difference in the hardness levels observed at the two pressures. It is then confirmed that the microstructural evolution is slow in Mo at the applied pressure of 2 GPa. It is considered that this slow evolution of the microstructure is attributed to lower applied pressure with respect to the high yield strength in Mo. Thus, the generation of dislocation is not sufficient to refine the grain size. It was shown that dislocations play an important role to form grain boundaries with high angle of misorientations [7]. More intense generation of dislocations and less recovery lead to finer grain sizes during severe plastic deformation [8]. It should be discussed why the microstructure becomes finer in Mo as the applied pressure is higher despite the fact the total strain is the same. It is well established that the strain is determined in proportion to the product of dislocation density and slip distance. Under a high-pressure constrained condition,

dislocations are forced to be generated more but at the same time they are forced to be annihilated. This should be less likely when the pressure is low. The saturation level is determined by the balance between dislocation generation and annihilation. The case of larger dislocation density and shorter slip distance at the high-pressure constrained condition yields the same strain as the case of smaller dislocation density and longer slip distance at the low-pressure constrained condition. The difference between the two conditions is that the grain size becomes smaller with higher angle boundaries in the former because the generated dislocations are more annihilated at grain boundaries. The difference in the microstructure as well as the saturation level arises from the difference in dislocation activity such as generation and annihilation which is more intense at a high-pressure constrained condition than at a low-pressure constrained condition.

2.2.3. (3) Tensile and Bending Tests

Stress-strain curves after tensile tests are delineated in Fig. 2.2.9(a) and (b) for Cr and Mo, respectively. For Cr, all tensile specimens were failed during loading except the as-received specimen. For Mo, the tensile strength significantly increased to ~1450 MPa with some ductility. The results after bending tests are shown in Fig. 2.2.10 to delineate nominal stress-displacement curves for Cr. Both tensile tests and bending tests are well consistent, where no ductility is present in the HPT-processed Cr. It is shown that bending stress is increased with increasing in applied pressure. Little ductility in Cr can be due to the effect of invisible cracks generated during the HPT process despite application of high pressure.

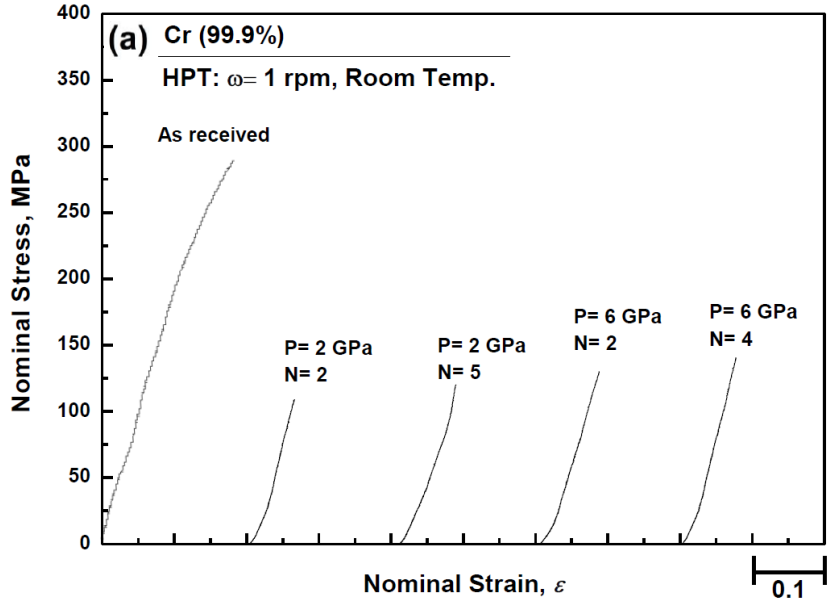

Figure 2.2.9. (continue)

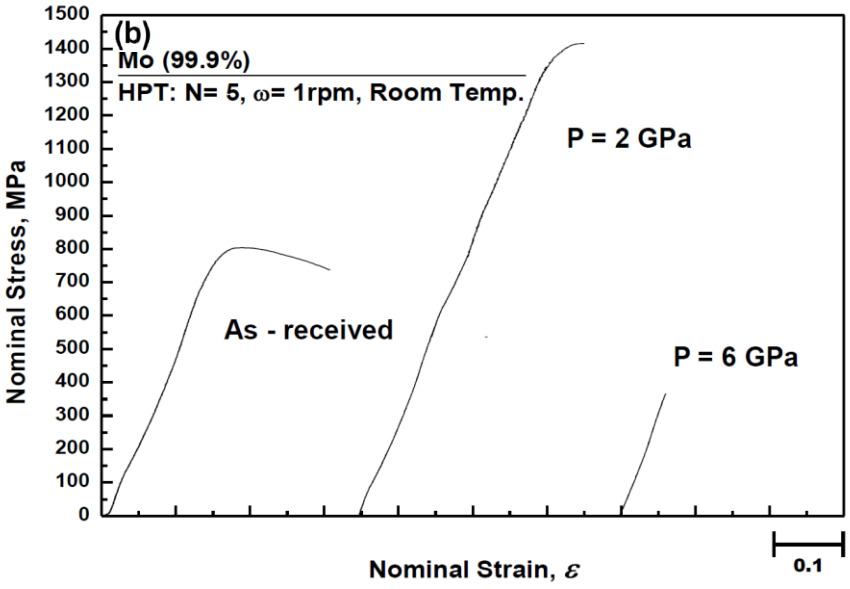

Figure 2.2.9. Nominal stress versus nominal strain curves after tensile testing for (a) Cr and (b) Mo under pressures of 2 and 6 GPa.

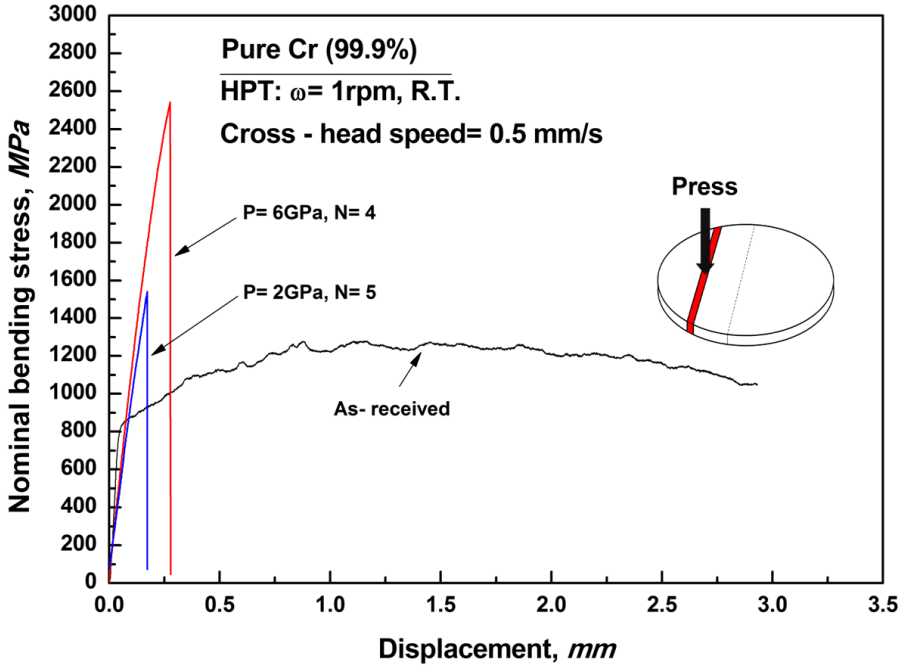

Figure.2.2.10. Nominal bending stress versus displacement curves after bending testing for Cr under pressures of 2 and 6 GPa.

2.2.3. (4) Fractography

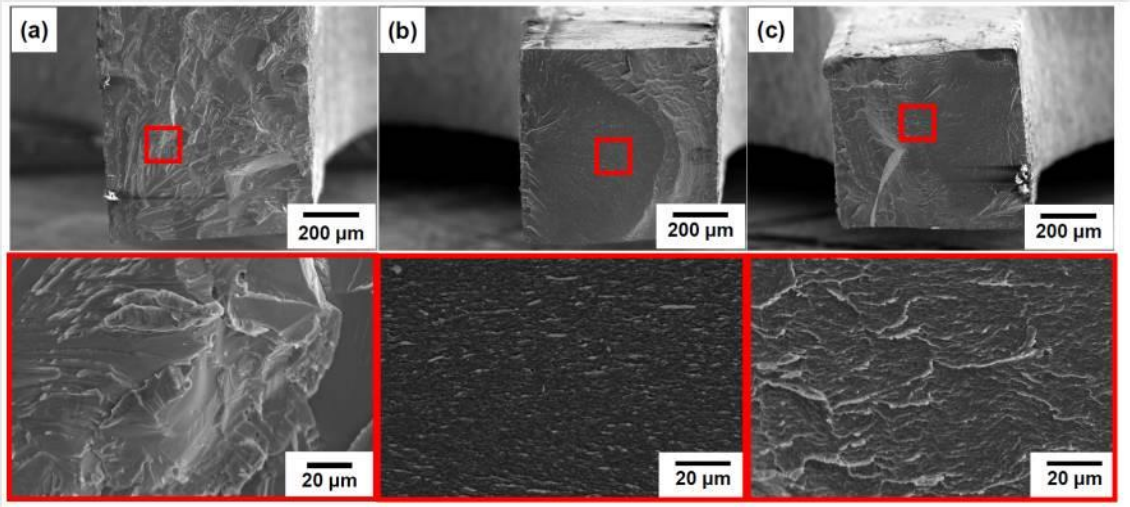

Figure 2.2.11. SEM fractographs after tensile testing for Cr: (a) as-received sample, (b) HPT-processed sample under P=2 GPa for N= 5 and (c) HPT-processed sample under P=6 GPa for N=4. Magnified views are shown from selected square areas in overall views.

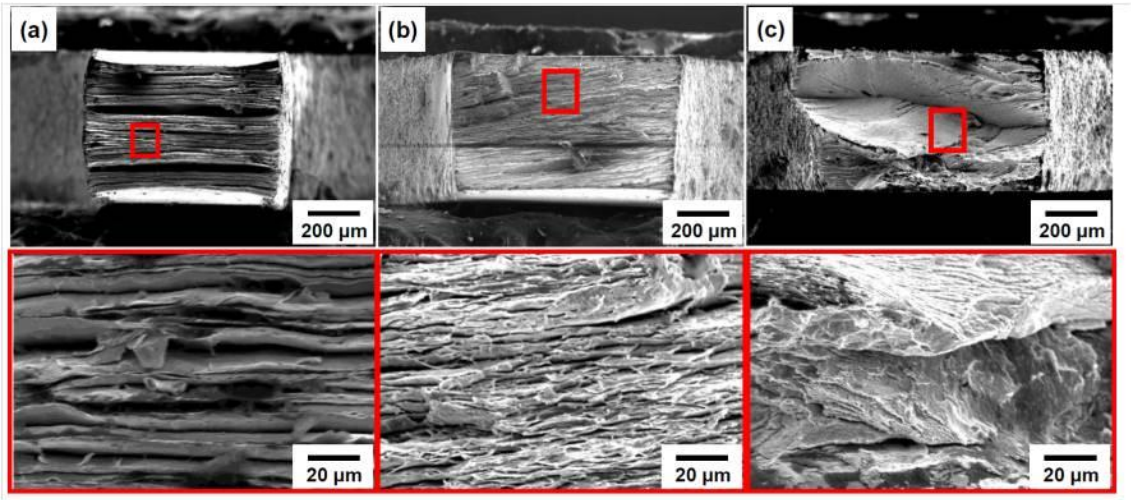

Figure 2.2.12. SEM fractographs after tensile testing for Mo: (a) as-received sample, (b) HPT-processed sample under P=2 GPa for N= 5 and (c) HPT-processed sample under P=6 GPa for N=5. Magnified views are shown from selected square areas in overall views.

Fractographs after tensile testing are displayed in Figs. 2.2.11 and 2.2.12 for Cr and Mo, respectively, where (a) represents the as-received sample and (b) and (c) correspond to HPT-processed samples under the pressures of 2 and 6 GPa for the largest number of revolutions. Figure 2.2.11 shows a brittle type of fracture in both as-received and HPT-processed specimens. The fracture surfaces of the as-received specimen are rough in the low magnification view but many smooth areas are visible in the high magnification view. For the HPT-processed specimens, the surfaces are smooth with sharp edges on the cross sections in the low magnification view but roughness finely appears on the fractured surfaces as found in the high magnification view. This fine roughness is then considered to be attributed to the fine-grained structure obtained by HPT.

The difference in the fractography is prominent between the fracture surfaces of the specimens processed at 2 and 6 GPa as shown in Fig. 2.2.12. Fine dimple patterns are visible for the specimen processed at 2 GPa but the smoother surface exhibits cleavage for the sample at 6 GPa. The latter surface appears because the specimen becomes hardened by intense straining and thus cracks form and propagate through the specimen. These features are then consistent with the fracture modes with some ductility in the former and brittleness in the latter as shown in Fig. 2.2.9(b).

2.2.4. Summary and Conclusions

1. Vickers microhardness data fall on a single curve when plotted as a function of equivalent strain for only Cr after HPT processing.
2. The hardness increases with increasing in the equivalent strain at an early stage of straining and reaches into a steady-state where the microhardness remains

unchanged even further straining.

3. TEM observation reveals that the grain size is reduced to 200~250 nm in Cr and ~350 nm in Mo at the saturation level throughout the sample. It is consistent with the tendency of microhardness plotting and grains are arranged along the torsion direction during HPT process
4. The hardness behavior of Mo is different from Cr. The hardness values lie on a single curve when the applies pressure is high as 6 GPa but, when it is lower, the hardness increase is gradual to the saturation level, and the hardness level deviates far below the saturation level as the pressure becomes lower. TEM observation reveals that the grain size is reduced to ~350 nm at the saturation level but the microstructure becomes coarser as the applied pressure is lower. The high tensile strength of ~1.4 GPa is achieved at a lower applied pressure as 2 GPa with some ductility but the tensile specimen fractures in a brittle manner when it is processed at the higher pressure of 6 GPa. The difference in the tensile behavior is well reflected in the fractography with fine dimples on the former but with smooth and cleaved surface on the latter.
5. The slower evolution of microstructure as well as of hardness to the saturation level observed in Mo is due to the applied pressure which is lower than the yield stress so that the dislocation activity is not sufficient to refine the grain size.

References

1. R.Z. Valiev, R.K. Islamgaliev, I.V. Alexandrov, Prog. Mater. Sci. 45 (2000) 103-189.

2. R.Z. Valiev, Y. Estrin, Z. Horita, T. G. Langdon, M. J. Zehetbauer, Y. T. Zhu, JOM 58 (2006) 33-39.

3. P.W. Bridgman, Phys. Rev. 48 (1935) 825-847.

4. G. Sakai, K. Nakamura, Z. Horita, T. G. Langdon, Mater. Sci. Forum 503-504 (2006) 391-396.

5. S. Lee, K. Edalati, Z. Horita, Mater. Trans. 51 (2010) 1072-1079.

6. N.A. Smirnova, V.I. Levit, V.I. Pilyugin, R.I. Kuznetsov, L.S. Davydova, V.A. Sazonova, Fiz. Met. Metalloved. 68 (1986) 1170-1177.

7. T. Hebesberger, H.P. Stuwe, A. Vorhauer, F. Wetscher, R. Pippan, Acta Mater. 53 (2005) 393-402.

8. K. Edalati, T. Fujioka, Z. Horita, Mater. Sci. Eng. A 497 (2008) 168-173.

9. Y. Ito, Z. Horita, Mater. Sci. Eng. A 503 (2009) 32–36.

10. K. Edalati, Z. Horita, Y. Mine, Mater. Sci. Eng. A 527 (2010) 2136-2141.

11. K. Edalati, Z. Horita, S. Yagi, E. Matsubara, Mater. Sci. Eng. A 523 (2009) 277-281.

12. K. Edalati, E.Matsubara, Z. Horita, Metall. Mater. Trans. A 40 (2009) 2097-2086.

13. K. Edalati, A. Yamamoto, Z. Horita , T. Ishihara, Scripta Mater. 64 (2011) 880-883.

14. F. Wetscher, A. Vorhauer, R. Pippan, Master. Sci. Eng. A 410-411 (2005) 213-216.

15.Y.R. Kolobov, B.Kieback, K.V. Ivanov, T.Weissgaerber, N.V. Girsova, Y.I. Pochivalov, G. Grabovetskaya, M.B. Ivanov, V.U. Kazyhanov and I.V. Alexandrov, Int. J. Refract. Met. Hard Mater. 21 (2003) 69-73.

16. Q. Wei, H.T. Zhang, B.E. Schuster, K.T. Ramesh, R Z. Valiev, L.J. Kecskes, R.J. Dowding, L. Magness, K. Cho, Acta Mater. 54 (2006) 4079-4089.

17. R. Wadsack, R. Pippan. B. Schedler, Fusion Eng. Des. 66–68 (2003) 265-269.

18. K. Edalati, T. Fujioka, Z. Horita, Mater. Trans. 50 (2009) 44-50.

19. K. Edalati, Z. Horita , T. G. Langdon, Scripta Mater. 60 (2009) 9-12.

20. E.N. Popova, V.V. Popov, E.P. Romanov, V.P. Pilyugin, Phys. Met. Metall. 103

(2007) 407-413.

21. E.N. Popova, V.V. Popov, E.P. Romanov, V.P. Pilyugin, Phys. Met. Metall. 101 (2006) 52-57.

22. V.V. Popov, E.N. Popova, A.V. Stolbovskiy, V.P. Pilyugin, Master. Sci. Eng. A 528 (2011) 1491-1496.

23. ASTM E290, Standard Test Methods for Bend Testing of Material for Ductility, ASTM International, West Conshohocken, PA, 2009.

24. K. Edalati, Z. Horita, Mater. Trans. 51 (2010) 1051-1054.

Chapter 3. Simultaneous strengthening of Al alloys through grain refinement and fine precipitation using high-pressure torsion and subsequent aging

3.1. Enhancement of strength and ductility of Al-Ag alloys processed by high-pressure torsion and aging

3.1.1. Introduction

In 1938, Gunier [1] and Preston [2] reported so-called GP zones in Al-rich, fcc Al-Cu plate-like precipitates and later Al-Ag spherical precipitates [3]. Precipitation in Al-Ag alloys was studied by Guinier, Geisler and Köster and their various collaborators [4]. Hardy and Heal [5] suggested that the most probable sequence of precipitation is spherical G.P. zones (possibly ordered) → γ` plates (Ag_2Al, formed on stacking faults or faulted during growth) → γ (formed by discontinuous precipitation, a solute-rich hexagonal-close-packed (hcp) phase inside of face-centered-cubic (fcc) solid solution). Strength of the alloys is improved along with such a well dispersed fine precipitation sequence during aging.

Grain refinement also increases the strength of metallic materials through the Hall-Petch relation [6, 7].

$$\sigma = \sigma_0 + kd^{-1/2} \tag{3.1.1}$$

where σ_o is the friction stress required to move a dislocation and k is a material-

dependent intensity factor related to hardening by grain boundaries. According to this equation, hard-materials can be produced by refining the grain size. However, it is not easy to achieve strengthening due to grain refinement and precipitation hardening simultaneously because grain refinement by a conventional deformation - recrystallization process (so-called thermomechanical treatment) is difficult while maintaining a supersaturated state for the subsequent precipitation through aging. It is well established that severe plastic deformation (SPD) process achieves grain refinement regardless of sample states including supersaturation. There are a few reports aiming at the combined effects of grain refinement and fine precipitation in age-hardenable alloys. Horita *et al.* [8] showed that age hardening is feasible in an Al-11wt%Ag alloy after grain refinement using equal-channel angular pressing (ECAP). It was also shown that not only tensile strength but also ductility is improved by such a dual effect of grain refinement and precipitate dispersion. In this research, one of the SPD processes, high-pressure torsion (HPT) [9,10] is adopted for grain refinement because a finer grain size is attained by intense shear strain using HPT. The objective of this research is thus to investigate hardening behavior due to the dual effect of grain refinement and fine dispersion of precipitates in Al-Ag alloys.

3.1.2. Materials and experimental procedures

Ingots of Al-Xwt%Ag (X= 5, 11 and 20) alloys were fabricated by arc-melting using high purity Al (99.99%) and Ag (99.99%) chips in argon atmosphere. The ingots were subjected to homogenization treatment at 500^{o}C for 24 hours in glass tubes filled with argon gas. The ingots were sliced to thicknesses of 1 mm and ground to 0.85 mm. Disks with 10mm diameter were cut from the slices by a wire-cutting electric discharge

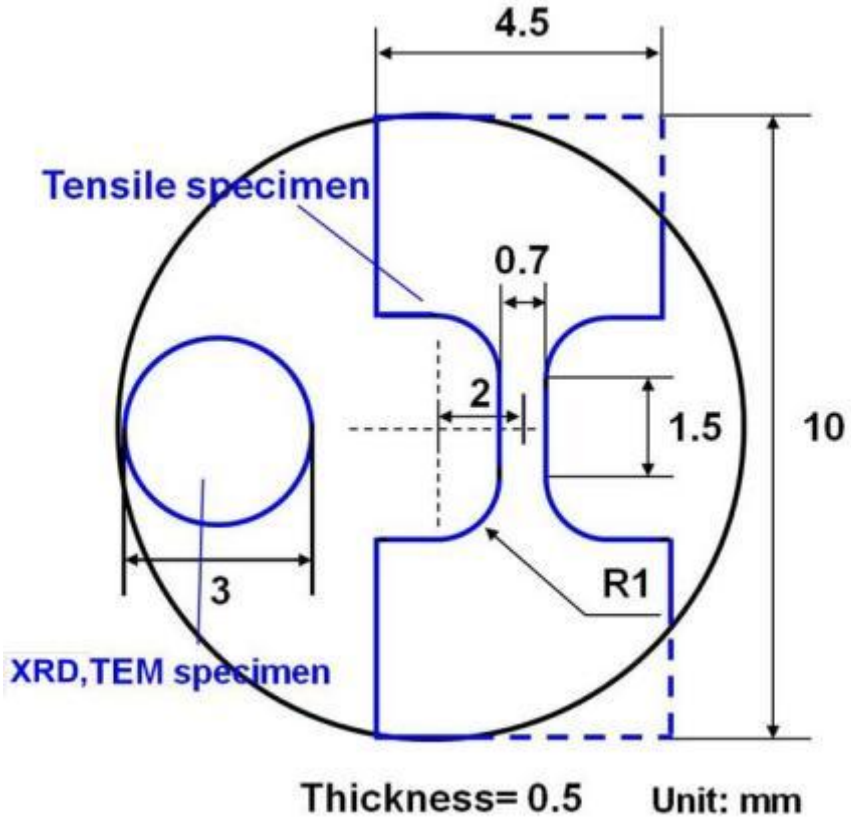

Figure 3.1.1. Dimensions of tensile and TEM specimens extracted from HPT disk.

machine (EDM). Solution treatment was then carried out at 550^{o}C for 1 hour before HPT processing.

The disks were processed by HPT under a pressure of 6 GPa for 1, 5 and 10 revolutions with a rotation speed of 1 rpm at room temperature. Slippage between the disk and the anvils was measured after 1/2 revolutions as described earlier [11]. After HPT processing, the disks were mechanically polished to a mirror-like surface and the Vickers microhardness was measured along 12 radial directions at every 0.5 mm from the disk center to the edge. Then, hardness values are averaged and plotted against the distance from the disk center and the equivalent strain.

After processing by HPT, aging treatments were conducted at 50^{o}C, 75^{o}C and 100^{o}C from 10 sec to 3.9 days. Hardness measurement was conducted on the aged samples as for the HPT processed samples along 4 radial directions. The average hardness was calculated from the four separate measurements at the same distances from the disk center.

The disks were mechanically polished to a thickness of ~0.50 mm and tensile specimens were cut from the polished disks using the EDM at a 2mm off-center position as illustrated in Fig. 3.1.1 with the dimensions of 1.5mm gauge lengths and 0.7mm widths. The tensile specimens were pulled to failure at a room temperature using a testing machine operating at a constant rate of cross-head displacement with the initial strain rate of 3.0×10^{-3} s^{-1}. The fracture surface was observed by a Hitachi S-4300SE field emission scanning electron microscope (FE-SEM) operating at 20 kV.

Disks with 3mm diameter were punched out from the center and edge parts of the HPT-processed disks as illustrated in Fig.3.1.1. They were ground to a thickness of 0.15 mm and thinned in a solution of 20%HNO_3 and 80%CH_3OH at 263 K using a

twin-jet electrochemical polisher under application of 15 V. The microstructures were observed using a Hitachi H-8100 transmission electron microscope (TEM) operating at 200 kV. Selected area electron diffraction (SAED) patterns were taken from regions having diameters of 6.3 μm. High resolution images were taken with JEOL JEM-2010FEF energy filter electron microscope after ion milling to remove an oxide layer of the sample for operating time of 5 min.

3.1.3. Results and discussion

3.1.3. (1) Hardness variations

After HPT processing, the hardness increases significantly when compared to solution treated samples and it saturates to constant levels regardless of Ag contents as shown in Fig. 3.1.2(a). It is shown that the samples after HPT processing are homogeneously deformed even near the center area. The hardness after the HPT processing is also plotted against equivalent strain and the hardness values fall on one single line regardless of the number of revolutions as shown in Fig. 3.1.2(b). Here, the following equation is used for the calculation of the equivalent strain.

$$\varepsilon = (1 - \mathrm{s}) \int_0^N \frac{2\pi r}{\sqrt{3}t(N)} dN \qquad (3.1.2)$$

where r is the distance from the disk center, N is the number of revolutions, s is the fraction of slippage and $t(N)$ is the disk thickness after HPT processing. The value of s was measured using a procedure as described earlier [12] and was found to be in the value of 0.1. The form of $t(N)$ was determined as a function of N by measuring the thicknesses after several different revolutions [13].

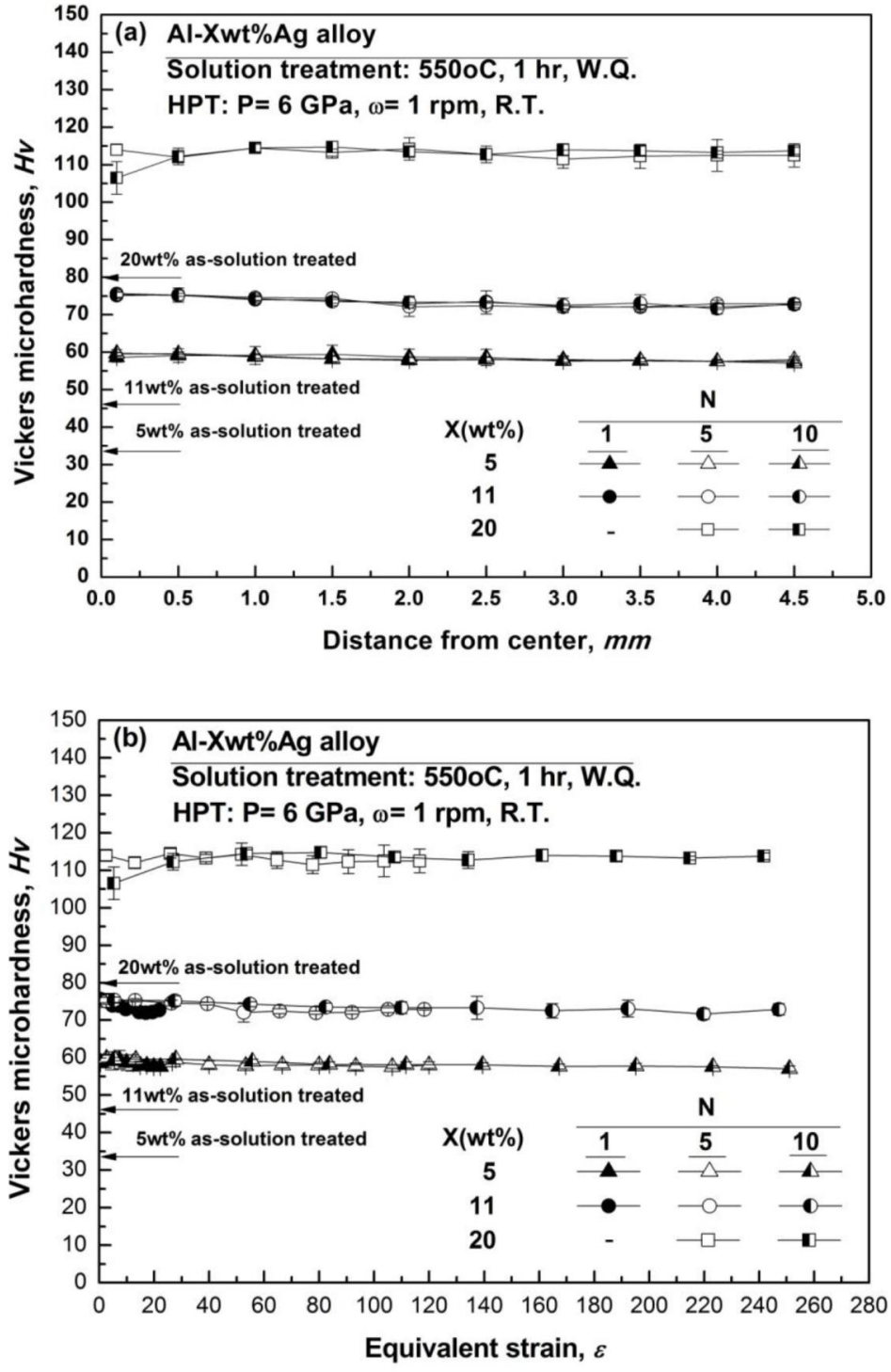

Figure 3.1.2. Vickers microhardness plotted against (a) distance from disk center and (b) equivalent strain after HPT processing under 6 GPa for 1, 5 and 10 revolution.

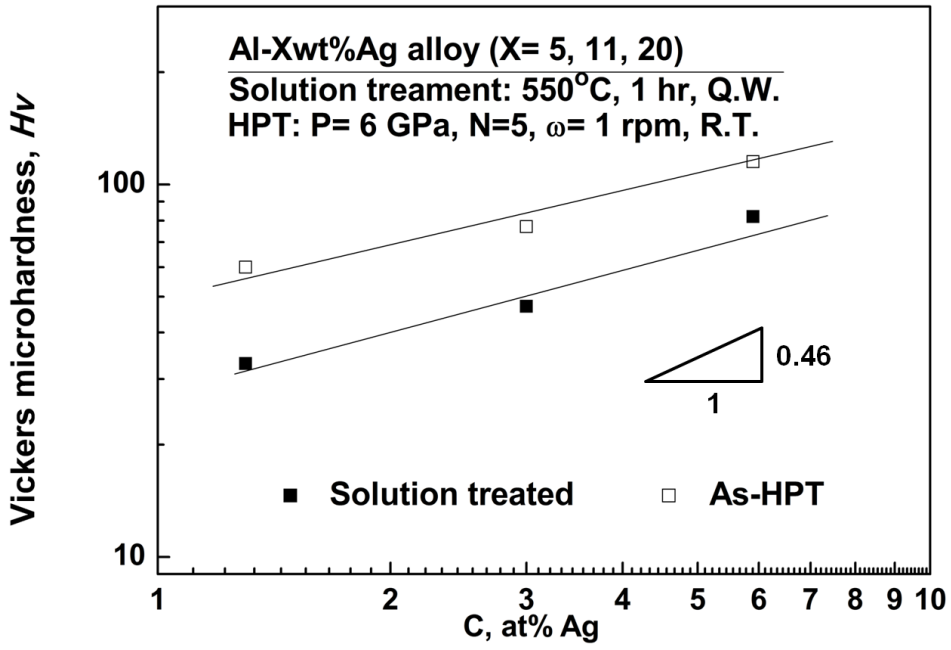

Figure 3.1.3. Vickers microhardness plotted against atomic concentration of Ag in Al after HPT processing under 6 GPa for 5 revolutions.

The hardness at the saturation in Fig. 3.1.2 is plotted as a function of Ag content in Fig. 3.1.3. The hardness increases with the Ag content for both solution treated and HPT-processed samples. This increase follows two straight lines in the double logarithmic plots, indicating that the concentration dependence of the hardness is expressed through the following relationship.

$$Hv \propto C^{1/2} \tag{3.1.3}$$

where *Hv* is the Vickers microhardness and *C* is the atomic concentration of Ag in Al. Because the extent of the hardness increase is almost the same between the solution treated sample and the HPT-processed sample, the effect of Ag is not affected by the severe plastic deformation.

3.1.3. (1-a) Hardness variations after HPT processing and aging

Figure 3.1.4 shows hardness plotted against the distance from the disk after different periods of aging at 100°C for (a) Al-5%Ag, (b) Al-11%Ag and (c) Al-20%Ag. Similar plots were also attempted after aging at 50 °C and 75 °C for the three Ag contents. For all cases, hardening occurs with aging but softening follows after prolonged aging. The aging behavior should be more clearly documented in Fig. 3.1.5 for the three compositions at the three different aging temperatures. Here, it is noted that the hardness data are taken from the values at the saturation in the plots of Fig. 3.1.4. As the aging temperature increases the time to reach the hardness peak becomes shorter in consistence with general aging behavior.

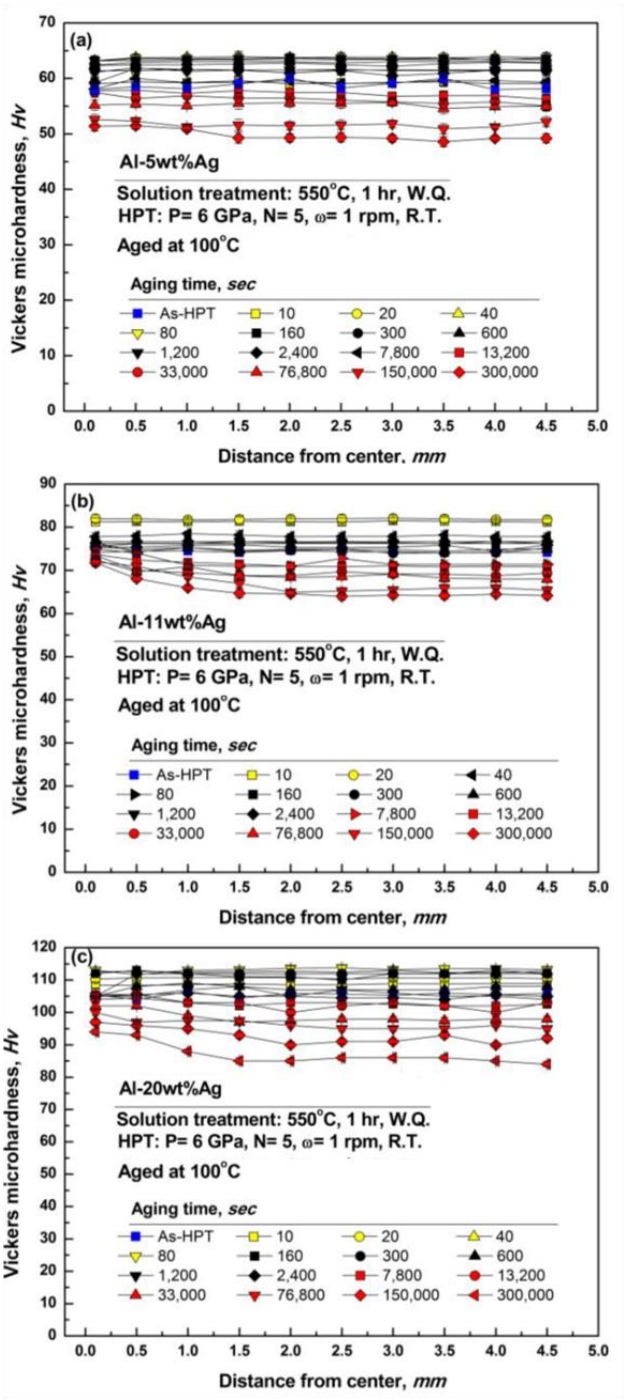

Figure 3.1.4. Hardness variation with distance from disk center for various aging periods at 100 °C after HPT processing under 6 GPa for 5 revolutions in (a) Al-5%Ag, (b) Al-11%Ag and (c) Al-20%Ag.

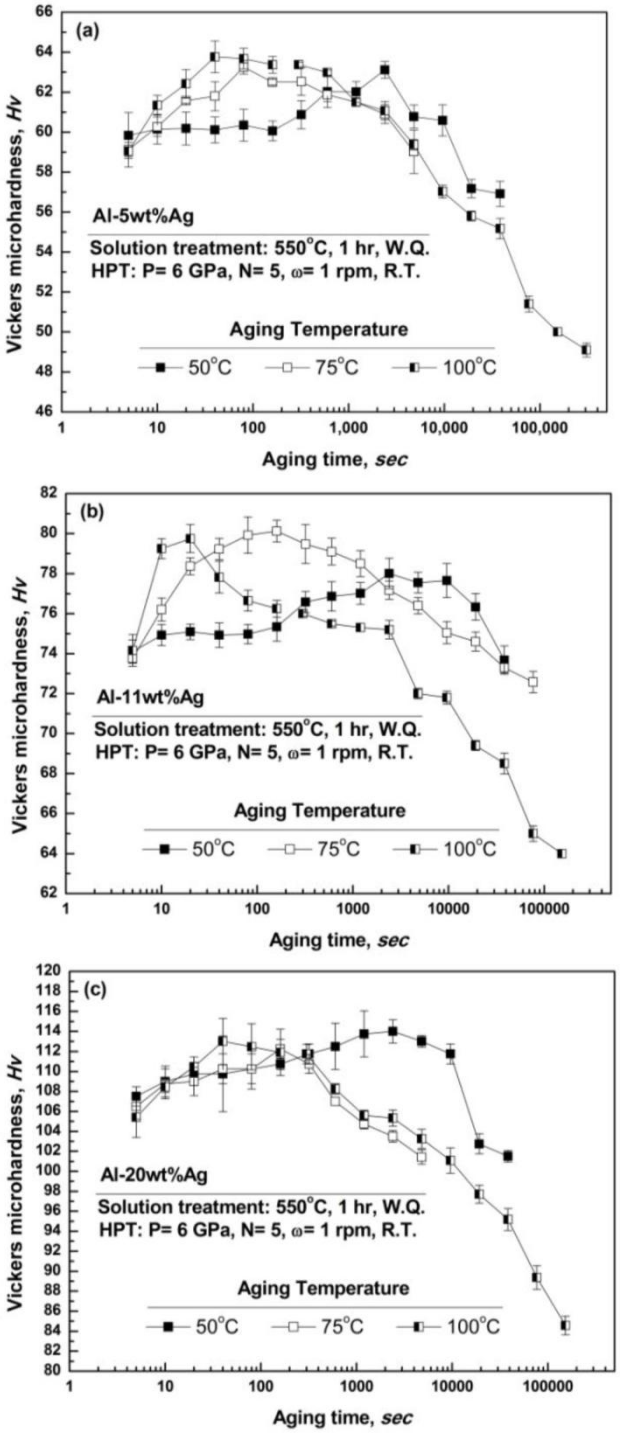

Figure 3.1.5. Hardness variation with aging time at 50, 75 and 100 °C in (a) Al-5%Ag, (b) Al-11%Ag and (c) Al-20%Ag.

Table 3.1.1 Time for reaching to peak aging and their amount of hardness increasing.

	50°C (Time / Δ*Hv*)	75°C (Time / Δ*Hv*)	100°C (Time / Δ*Hv*)
5wt%	2,400 / 3.4	80 / 3.5	40 / 3.9
11wt%	2,400 / 3.9	80 / 5.6	20 / 6.1
20wt%	2,400 / 6.5	160 / 6.4	40 / 7.1

$\Delta Hv = Hv_{peak\ aged} - Hv_{as\text{-}HPT}$

Unit: sec / Hv

The peak hardness and the time to the peak value are summarized in Table 3.1.1. Figure 3.1.6 shows a comparison between the Al-11%Ag samples after HPT and ECAP followed by aging at 100°C. The aging proceeds faster in the HPT-processed sample than in the ECAP-processed sample so that the peak hardness reaches after 20 seconds in the former but after 100 hours in the latter. It is considered that this is due to the difference in strain imposed by HPT and ECAP: equivalent strain is well above 20 in the HPT but ~8 in the ECAP. Therefore, more lattice defects are formed in the HPT-processed samples than in the ECAP-processed samples to enhance the aging behavior.

3.1.3. (2) Tensile testing

Tensile tests were conducted with an initial stain rate of 3.0×10^{-3} s^{-1} at room temperature. Dimensions of the tensile specimen are delineated in Fig. 3.1.1. Stress-strain curves are plotted in Figs. 3.1.7, 3.1.8 and 3.1.9 for the Al-5%Ag, Al-11%Ag and Al-20%Ag alloys, respectively. In consistence with the hardness measurements, the peak aging leads to the highest ultimate tensile strength (UTS) for all alloys at any aging temperatures. However, the over aging results in a decrease in the flow stress regardless of the alloys and aging temperatures without exception. The total elongation to failure also remains high and, in particular, it is highest among the samples after the peak aging at the aging temperatures in the Al-5%Ag alloy and after the peak aging at the aging temperature of 100°C in the Al-11%Ag alloy. It can be concluded that the strength and high ductility are achieved by grain refinement and subsequent aging in consistence with an earlier report using ECAP [8].

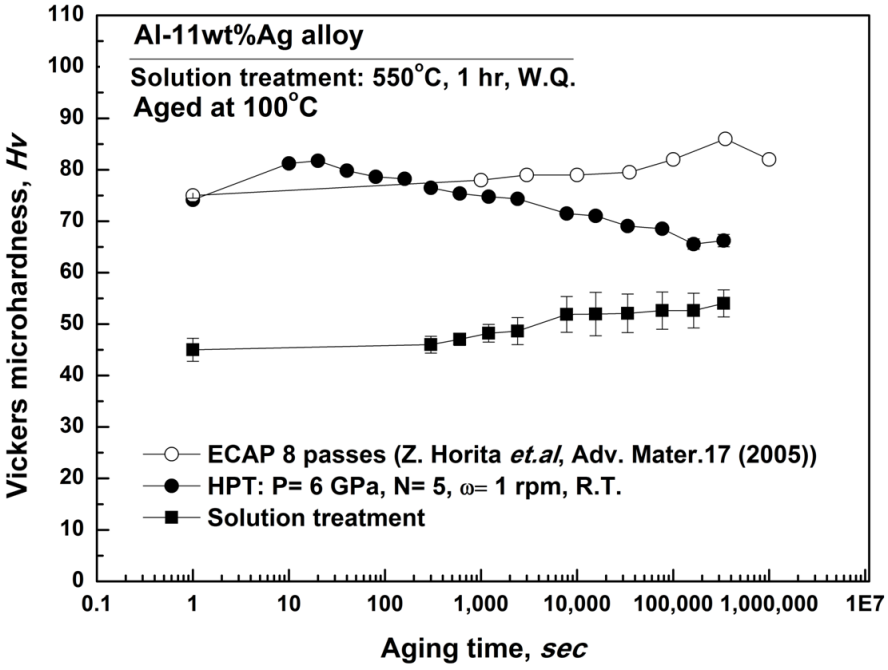

Figure 3.1.6. Hardness variation with aging at 100°C for samples after solution treatment, ECAP processing and HPT processing in Al-11wt%Ag alloy.

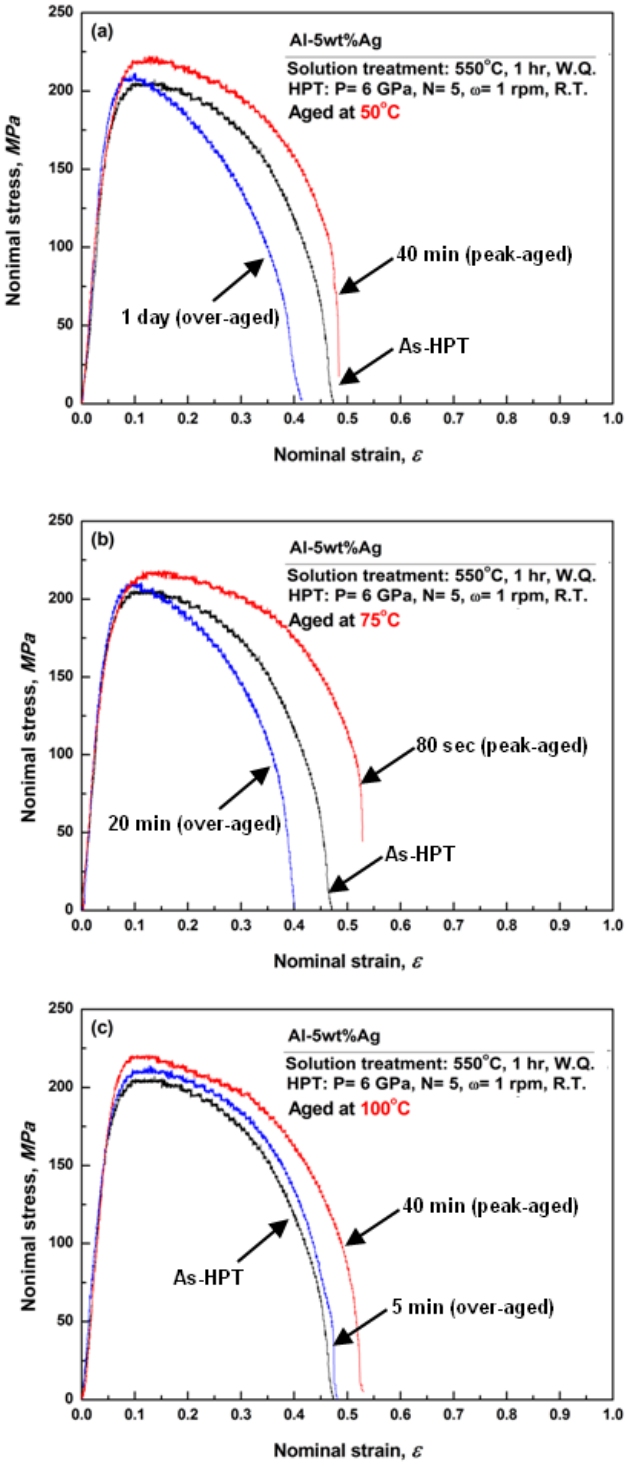

Figure.3.1.7. Strain- stress curves of Al-5%Ag alloy after HPT processing and aging at (a) 50°C, (b) 75°C and (c) 100°C.

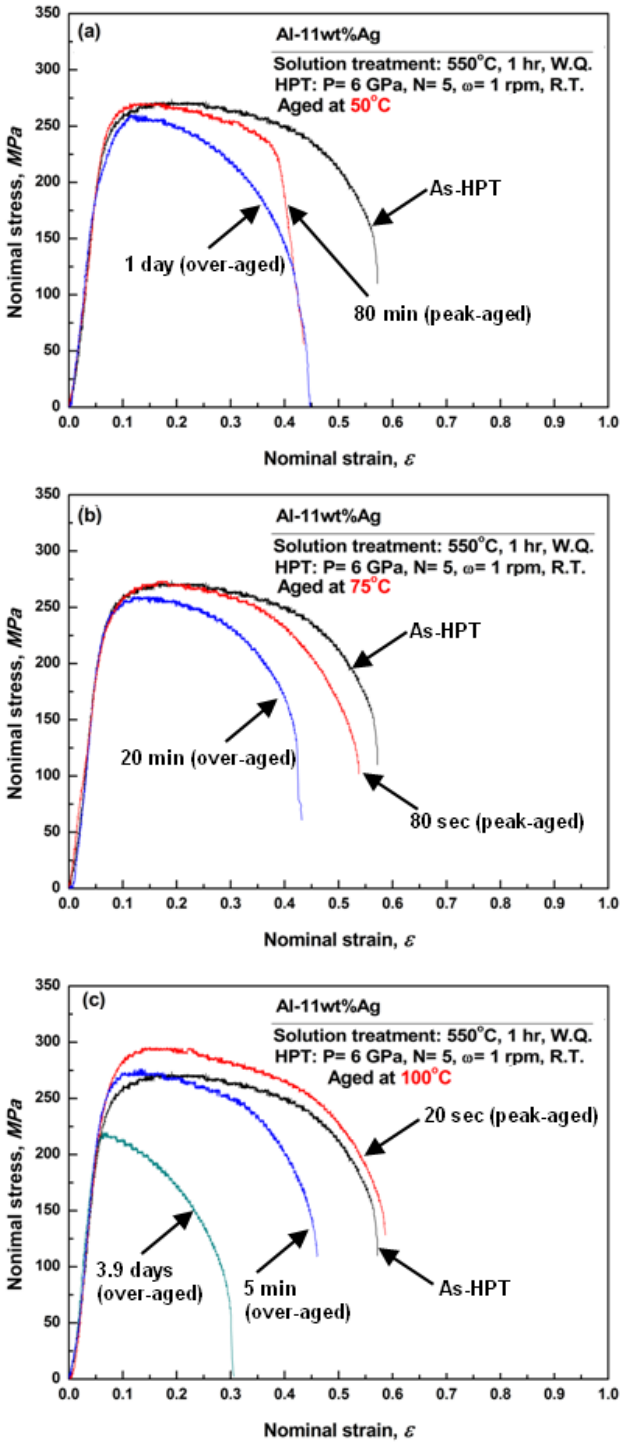

Figure 3.1.8. Strain- stress curves of Al-11%Ag alloy after HPT processing and aging at (a) 50°C, (b) 75°C and (c) 100°C.

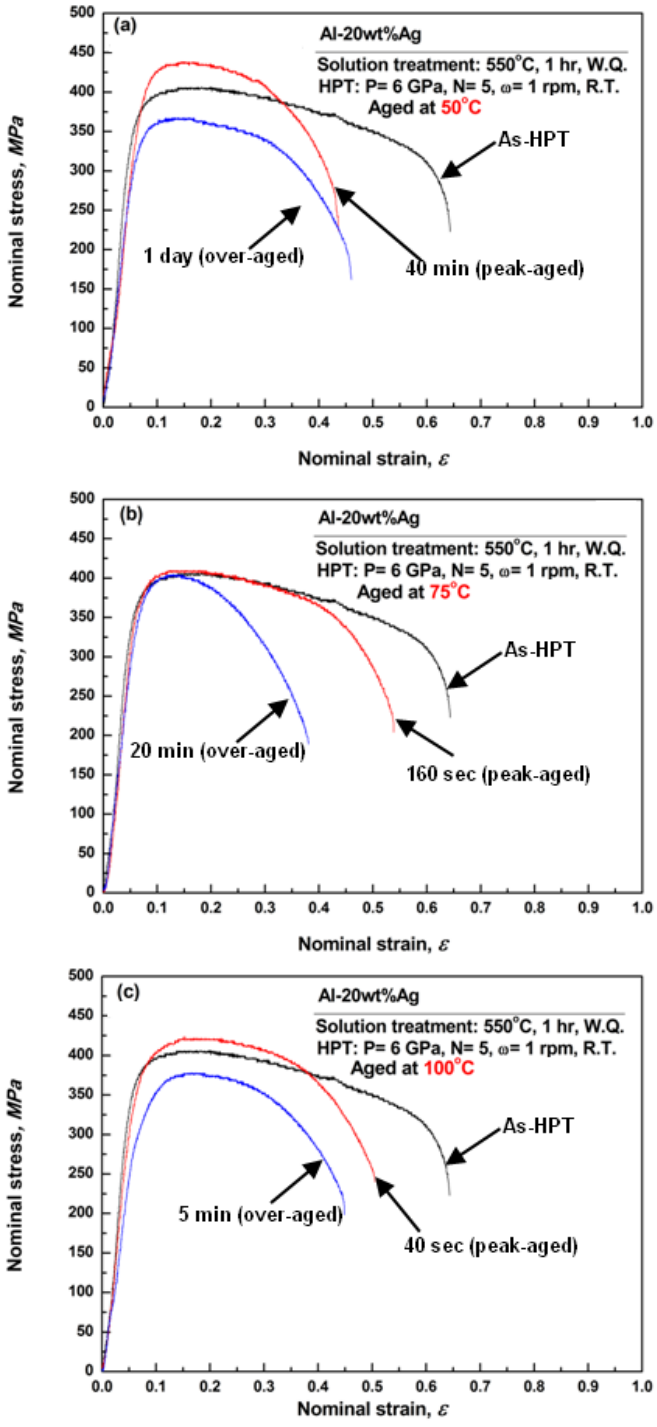

Figure 3.1.9. Strain- stress curves of Al-20%Ag alloy after HPT processing and aging at (a) 50°C, (b) 75°C and (c) 100°C.

Table 3.1.2 Ultimate tensile strength (UTS), yield strength (YS) and Elongation in Al-Ag alloy after tensile test.

			Aging time (sec)	UTS (MPa)	YS (MPa)	Elongation (%)
5wt%Ag		as -HPT	-	207	159	47
	50°C	peak aged	2,400	222	129	48
		over aged	86,400	211	156	41
	75°C	peak aged	80	217	118	53
		over aged	1,200	209	130	40
	100°C	peak aged	40	221	129	53
		over aged	300	213	159	48
11wt%Ag		as -HPT	-	272	189	57
	50°C	peak aged	2,400	270	194	44
		over aged	86,400	259	172	45
	75°C	peak aged	80	272	194	54
		over aged	1,200	259	209	43
	100°C	peak aged	20	294	174	59
		over aged	300	275	202	46
		over aged	300,000	218	191	31
20wt%Ag		as -HPT	-	405	254	64
	50°C	peak aged	2,400	436	291	44
		over aged	86,400	367	273	47
	75°C	peak aged	160	408	247	54
		over aged	1,200	402	305	38
	100°C	peak aged	40	420	267	50
		over aged	1,200	376	265	45

3.1.3. (3) Fractographs

Figure 3.1.10 shows representative images of the fracture surfaces observed with FE-SEM for samples after the tensile testing. Figure 3.1.10 (a) and (b) correspond to the Al-5wt%Ag sample at the HPT-processed condition, Fig. 3.1.10 (c) to the Al-11wt%Ag sample aged for 20 sec at 100^{o}C, Fig. 3.1.10 (d) to the Al-20wt%Ag sample aged for 160 sec at 75^{o}C where both Fig. 3.1.10 (c) and (d) are at peak-aged conditions. Figure 3.1.10 (e) and (f) are fracture surfaces of over aged samples where (e) is the Al-11wt%Ag sample aged for 3.9 days at 100^{o}C and (f) is the Al-20wt%Ag sample aged for 20 min at 75^{o}C. Figure 3.1.10 (a) shows an overall view of a fractured specimen exhibiting ductile fracture with area and thickness reduction.

Intergranular fracture patterns with different dimple sizes are confirmed on the fracture surfaces in Fig.3.1.10. Many micro-dimples are visible with the size of ~300 nm in Fig. 3.1.10 (c) and (d), and they are well comparable to the average grain sizes observed by TEM (as described later in Figs. 3.1.11 and 3.1.12). Even for the fracture surfaces of the over-aged sample, many dimples are observed, while some torn holes having the size of ~5 μm are visible. These holes are observed typically in the over aged samples. It is considered that the torn holes arise from coarsened incoherent γ precipitates.

UTS, Yield strength and elongation data were summarized in Table 3.1.2.

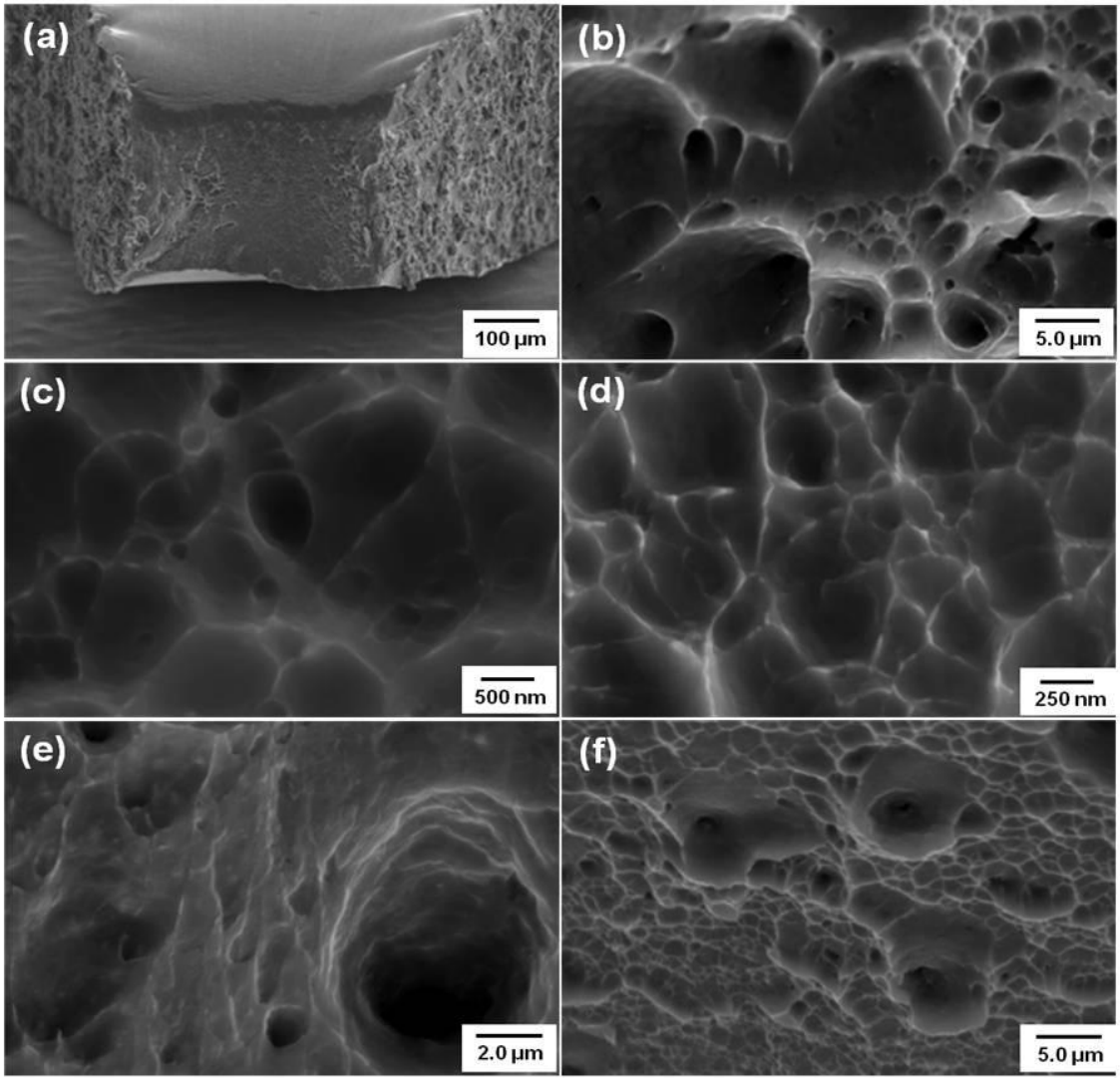

Figure 3.1.10. Fractographs after tensile testing : (a) overall view, (b) enlarged image of (a) in HPT-processed sample, (c) peak-aged (20 sec) at 100^{o}C in HPT-processed Al-11wt%Ag alloy, (d) peak-aged (80 sec) at 75^{o}C in HPT-processed Al-20wt% alloy, (e) over-aged (3.9 days) at 100^{o}C in HPT-processed Al-11wt%Ag alloy and (f) over-aged (20 min) at 75^{o}C in HPT-processed Al-20wt% alloy.

3.1.3. (4) TEM microstructure

Figure 3.1.11 (a) and (b) show representative microstructures including selected area electron diffraction (SAED) patterns after HPT processing without aging for the Al -5wt%Ag and Al-20wt% Ag alloys, respectively: in both figures, bright- field (BF) images on the left and dark-field (DF) images on the right. The DF images were taken with the diffracted beams indicated by arrows in the SAED patterns. Grain refinement was achieved with sizes of ~430 nm in all compositions of the alloys. Inspection of the SAED patterns reveals that the alloys consist of grains with high-angle grain boundaries. There are no extra spots in the SAED patterns other than the fundamental from the Al matrix, indicating that no intermetallic particles exist.

Representative TEM microstructures after peak aging are shown together with SAED patterns in Fig. 3.1.12 (a) and (b) for the Al-5wt%Ag and Al-20wt%Ag alloys, respectively.

Fine grains are retained during the aging. The DF images in Fig. 3.1.12 (a) and (b) were taken from selected spots in the SAED patterns as marked by arrows. Precipitate particles are not visible in the images at least at this magnification for both alloys. High resolution TEM reveals that spherical η-zones with a size of ~10 nm are formed in the Al-11wt%Ag alloy as shown in Fig.3.1.13 after HPT processing under 6 GPa for 5 revolutions and peak-aging at 100^{o}C. The fine precipitation of such η-zones is then responsible for the age hardening above the hardness level achieved by the HPT processing.

Figure 3.1.14 shows typical microstructures and an SAED pattern the Al-20wt%Ag alloy processed by HPT under 6 GPa for 5 revolutions and over-aged at 100^{o}C for 5 min. In the BF image, there are many small spherical or elliptical particles

along the grain boundaries. Close inspection reveals that these particles are γ precipitates, and the particles from the γ (101) reflection are brightened in the DF image with a size of ~20 nm with arrows. Coarsened γ precipitates with the elliptical shape are observed with the size of ~100 nm. Figure 3.1.15 shows microstructures of the Al-11wt%Ag alloy processed by HPT for 5 revolutions under 6 GPa and over-aged for 3.9 days at 100°C. Because of the prolonged aging, the precipitation proceeded for the particle to grow as large as ~500 nm in the size as shown in Fig. 3.1.15 (a). Diffraction analysis using dark-field images in Fig. 3.1.15(b), (c) and (d) reveals that the precipitate particles are stable γ phase. It is now reasonable to understand that the formation of such large stable γ particles gave rise to the decrease in tensile strength and the reduction in ductility as shown in Figs 3.1.7, 3.1.8 and 3.1.9.

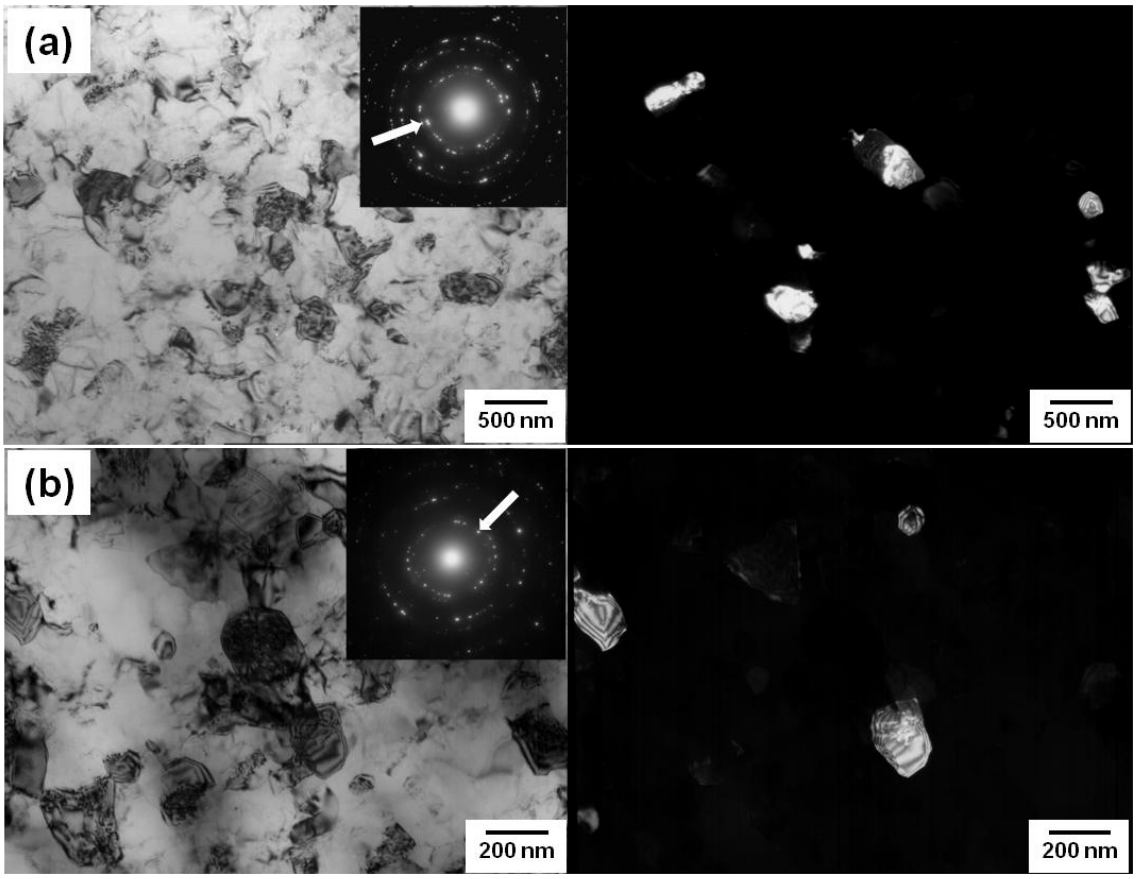

Figure 3.1.11. TEM micrographs and SAED patterns of as-HPT sample processed for 5 revolutions under 6 GPa in (a) Al-5wt%Ag alloy and (b) Al-20wt%Ag alloy.

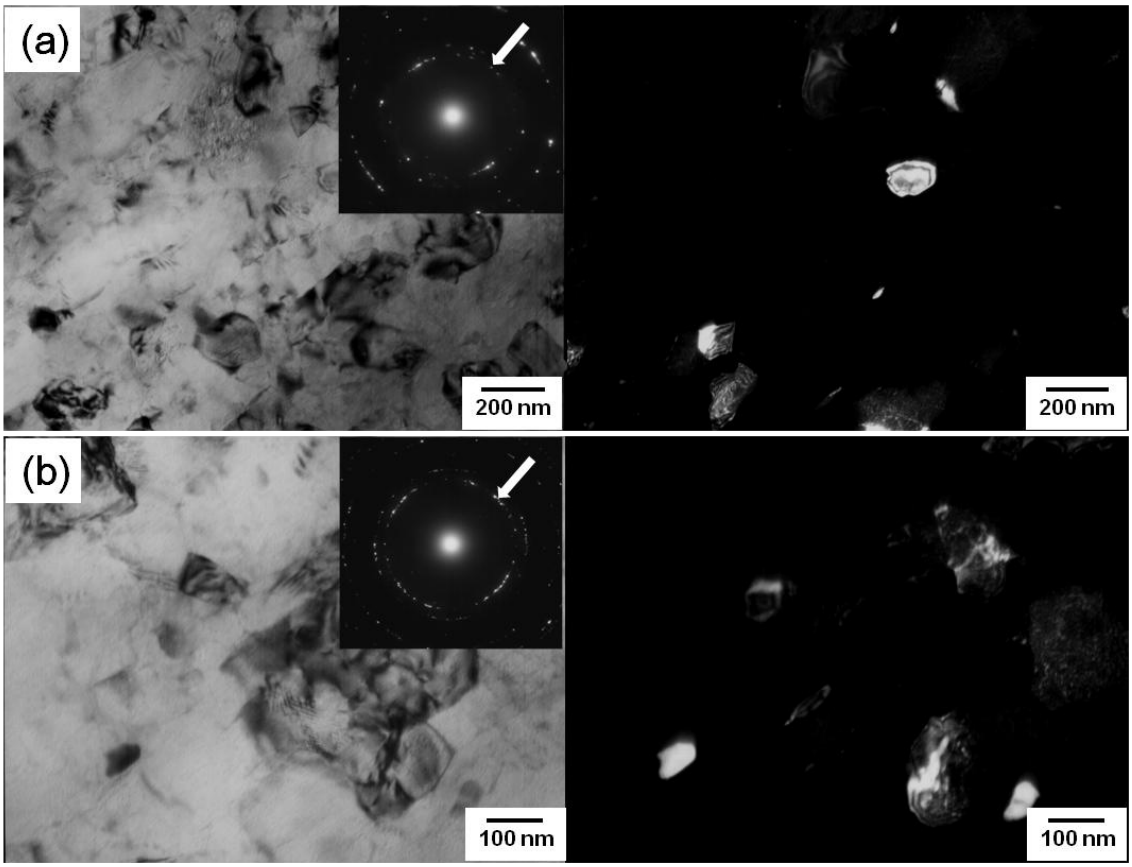

Figure 3.1.12. TEM micrographs and SAED patterns of peak-aged at 100^{o}C specimen processed for 5 revolutions under 6 GPa in (a) Al-5wt%Ag alloy and (b) Al-20wt%Ag alloy.

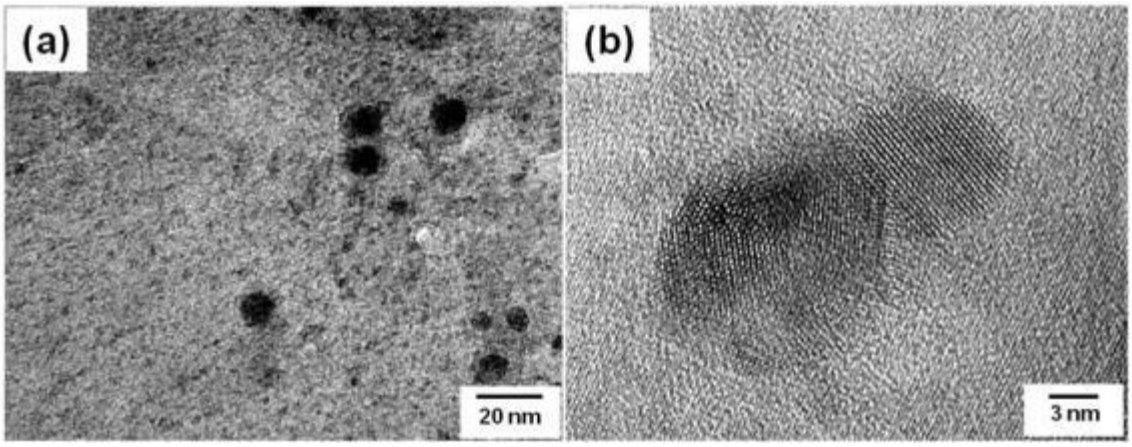

Figure 3.1.13. High resolution TEM micrographs of Al-11wt%Ag alloy processed for 5 revolutions under 6 GPa and peak-aged at 100^{o}C: (a) overall image and (b) η-zones.

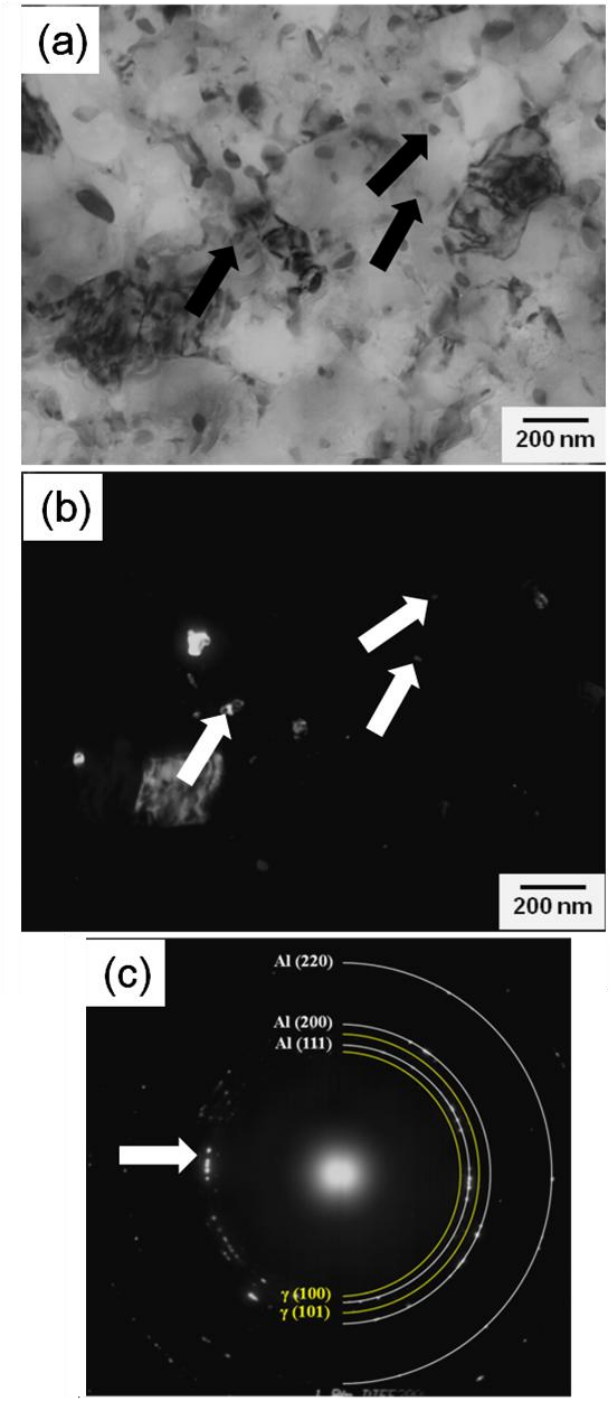

Figure 3.1.14. TEM micrographs and SAED pattern of Al-20wt%Ag alloy processed for 5 revolutions under 6 GPa and over-aged at 100^{o}C for 5 min: (a) bright-field image, (b) dark-field image and (c) SAED pattern.

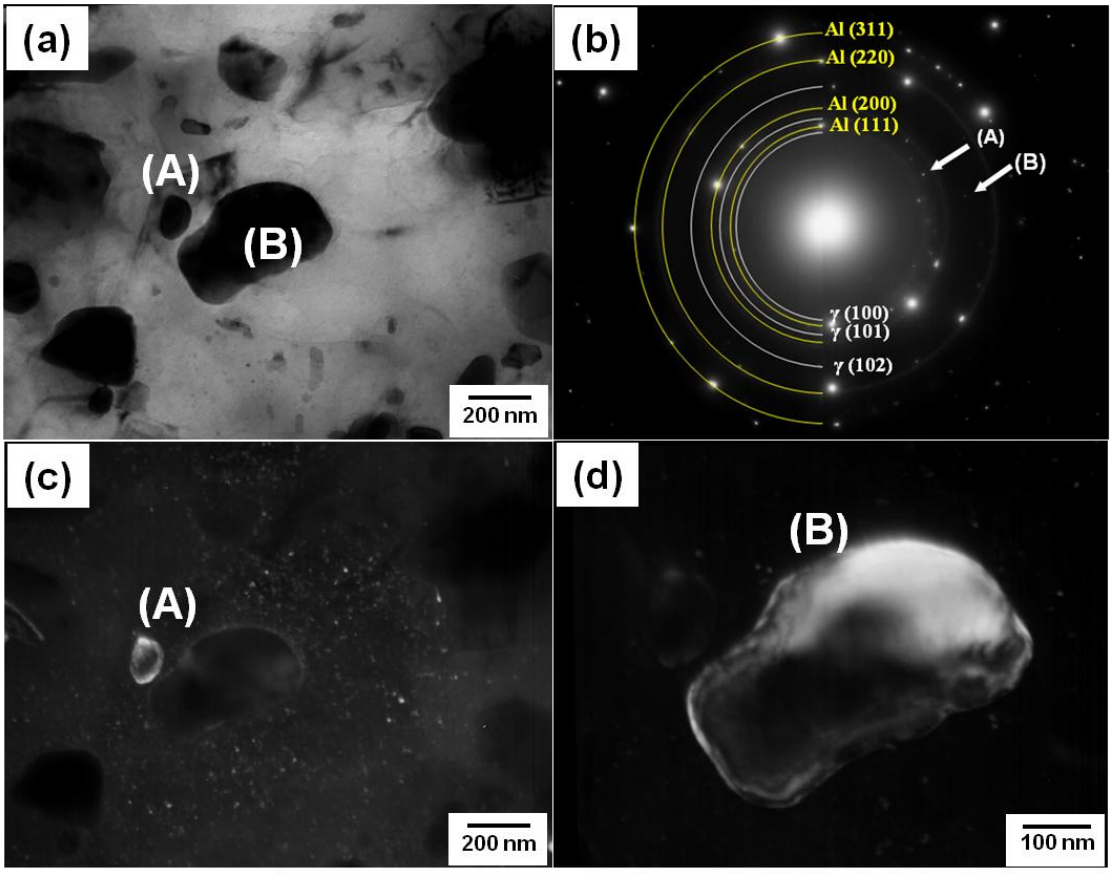

Figure 3.1.15. TEM micrographs and SAED pattern of Al-11wt%Ag processed for 5 revolutions under 6 GPa and over-aged at 100^{o}C for 3.9 days: (a) bright-field image, (b) SAED pattern with selected spots A and B, (c) dark-field image of A and (d) dark-field image of B.

3.1.4. Summary and conclusions

Hardening due to grain refinement and fine precipitation is attained in Al- X wt%Ag (X= 5, 11 and 20) alloys by application of high-pressure torsion (HPT) and subsequent aging at lower temperatures.

1. After HPT processing, grains are refined to an average size of ~300 nm. Grain refinement leads to a significant increase in hardness.
2. Following aging of the HPT-processed samples, the hardening was confirmed. The hardness reaches a peak much faster than ECAP because of more strain imposed by the HPT process.
3. High-resolution TEM analysis reveals that a fine dispersion of spherical η zone with the size of ~10 nm is formed in the matrix having ultrafine-grained structure.
4. This study has presented a dual effect of grain refinement and fine precipitation on the enhancement of the strength. It has also been shown that at peak-aged condition, the tensile strength is enhanced while maintaining considerable ductility.

References

1. A. Guinier, Nature 142 (1938) 569.

2. G.D. Preston, Nature 142 (1938) 570.

3. A. Guinier, J. Phys. Radium 3 (1942) 124-136.

4. R.B. Nicholson, J. Nutting, Acta Metall. 9 (1961) 332-343.

5. H.K. Hardy, T.J. Heal, Progr. Met. Phys. 5 (1954) 143-278.

6. E.O. Hall, Proc. Phys. Soc. London Sect. B 64 (1951) 747-753.

7. N.J. Petch, J. Iron Steel Inst. 173 (1953) 25-28.

8. Z. Horita, K. Ohashi, T. Fujita, K. Kaneko, T.G. Langdon, Adv. Mater. 17 (2005) 1599-1602.

9. P.W. Bridgman, Phys. Rev. 48 (1935) 825-847.

10. R.Z. Valiev, R.K. Islamgaliev, I.V. Alexandrov, Prog. Mater. Sci. 45 (2000) 103-189.

11. K. Edalati, T. Fujioka, Z. Horita, Mater. Trans. 50 (2009) 44-50.

12. Y. Todaka, J. Sasaki, T. Moto, M. Umemoto, Scripta Mater. 59 (2008) 615-618.

13. Y. Ito, Z. Horita, Mater. Sci. Eng. A 503 (2009) 32-36.

14. K. Edalati, T. Fujioka, Z. Horita, Mater. Sci. Eng. A 497 (2008) 168-173.

15. S. Lee, K. Edalati, Z. Horita, Mater. Trans. 51 (2010) 1072-1079.

16. K. Edalati, E. Matsubara, Z. Horita, Mater. Sci. Eng. A 40(2009) 2079-2086.

17. W.Q. Cao, C.F. Gu, E.V. Pereloma, C.H.J. Davies, Mater. Sci. Eng. A 492 (2008) 74-79.

18. K. Ohashi, T. Fujita, K. Kaneko, Z. Horita, T.G. Langdon: Mater. Sci. Eng. A 437 (2006) 240-247.

19. J.M. Silcock, T.J. Heal, H. K. Hardy, J. Inst. Met. 82 (1953-1954) 239-248.

20. C. Laird, H.I. Aaronson, Acta Metall. 17 (1969) 505-519.

3.2. Age- hardening of Al-Li-Cu-Mg Alloy (2091) processed by high-pressure torsion

3.2.1. Introduction

Lithium (Li) is the lightest metal found in nature (density is 0.53g/cm^2) and its addition to aluminum significantly reduces the density of alloys with high strength [1]. These Al-Li alloys are strengthened by aging treatment through a fine dispersion of precipitate particles. The precipitation in the Al-Li alloys occurs two step processes as follows [2] but the first process is far more important for the strengthening.

α (super saturated solid solution)→ δ` (Al_3Li)→ δ (AlLi)

Grain refinement is also an important process to increase the strength of metallic materials. About 2 decades ago, severe plastic deformation (SPD) process was shown to be effective for the grain refinement typically to the submicrometer and/or nanometer scale [3]. Although several SPD methods are available, the process of high-pressure torsion (HPT) produces the grain sizes finer than the other methods [4]. However, it is generally difficult to achieve combined effects of both grain refinement and fine dispersion of precipitates. This is because grain refinement to the submicrometer range is not easy in practice in alloys with supersaturated conditions using conventional thermomechanical treatment. Provided that such a supersaturation is achieved in an ultrafine-grained alloy, another important task is to make a fine precipitation within the fine grains by subsequent aging while keeping the grain size small.

There are a few reports aiming at the combined effects of grain refinement and fine precipitation in age-hardenable alloys [5-7]. The objective of this research is to investigate a possibility of achieving the simultaneous effect of grain refinement and fine precipitation using an Al-Li-Cu-Mg alloy (2091) which is well known as a typical

age-hardenable alloy [8-11]. HPT is adopted for grain refinement and aged for various time and temperatures because it is applicable to many metallic materials without heating process [13].

3.2.2. Experimental materials and procedures

This study used a 1.6mm cold-rolled sheet of a 2091 alloy (Al-2.09%Li-1.99%Cu-1.55%Mg-0.12%Zr-0.03%Si-0.05%Fe-0.03%Ti in mass%).

Disks of 10mm diameter were cut from the sheet by an electrical discharge machine (EDM). They were subjected to solution treatment at 505^{o}C for 30 minutes and quenched in cold water. These disks were ground to a thickness of 0.85 mm and were subjected to HPT under a pressure of 6 GPa for 1/4, 1/3, 2 or 5 revolutions with a rotation speed of 1 rpm at room temperature. The alignment around the rotation axis of the upper and lower axes was adjusted to well within ±0.01 mm for the HPT process. Slippage between the disk and the anvils was measured after 1/4 revolutions using the procedure as in Ref. [14]. Aging treatment was undertaken on the HPT-processed alloy at 100, 150 and 190^{o}C for the total periods up to 9.3 days. A piece of the as-received sheet was also solution-treated and subsequently rolled by 50% at room temperature. This was then followed by aging at the same conditions as for the HPT-processed disks for comparison. Vickers microhardness was measured along 12 radial directions at every 0.5 mm from the disk center to the edge on mechanically polished surface. Averages were taken from the twelve measurements at the same distances from the disk center. Each hardness measurement was conducted by using a load of 50 g for a duration time of 15 s.

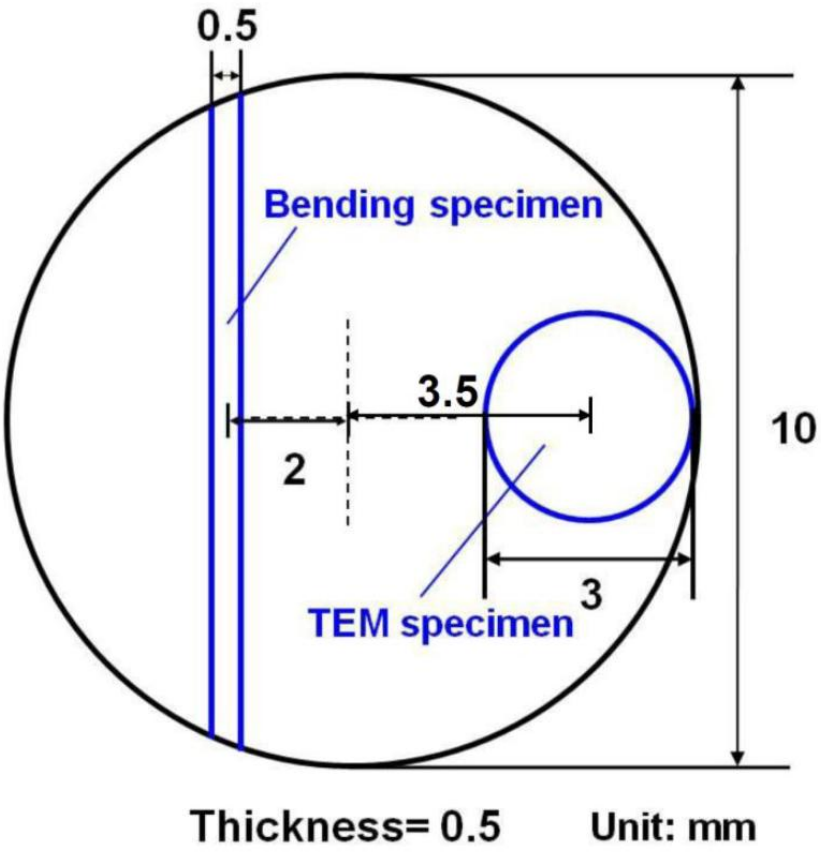

Figure 3.2.1. Dimensions of disk sample including positions for TEM disks and bending specimen.

After processing by HPT, the disks were mechanically polished to a thickness of ~0.50 mm and bending specimens were cut to dimensions with a 0.5mm×0.5mm×9mm rod at 2 mm from the disk center, as illustrated in Fig. 3.2.1. Three-point bending tests were conducted at room temperature with a cross-head speed of 0.5 mm/s using an 8 mm supporting span. The loading during bending tests was made parallel to the pressing direction in HPT. The Euler–Bernoulli beam theory was used to estimate the bending stress [15]

$$\sigma = \frac{3Fl}{2wh^2} \tag{3.2.1}$$

where F is the bending load, l is the supporting span (8 mm), w is the bending specimen width (0.5 mm), and h is the bending specimen height (0.5 mm).

The fracture surface and deformed bending specimen were observed using a JEOL JSM-5600 scanning electron microscope (SEM) operating at 20 kV. Disks with 3mm diameter were punched out from the center and edge parts of the HPT-processed disks as illustrated in Fig. 3.2.1. They were ground to a thickness of 0.15 mm and then thinned using a twin-jet electro-polishing facility in a solution of 20%HNO_3 and 80%CH_3OH at room temperature with an application of 5~10 V. The microstructures were observed using a Hitachi H-8100 and Akashi EM-002B transmission electron microscope (TEM) operating at 200 kV and 125 kV, respectively. Selected area electron diffraction (SAED) patterns were taken from regions having diameters of 6.3 μm.

3.2.3. Results and discussions

3.2.3. (1) Vickers microhardness measurements

3.2.3. (1-a) After HPT process

Figure 3.2.2(a) plots Vickers microhardness against the distance from the disk center after HPT processing for 1 and 5 revolutions. For both revolutions, the microhardness increases with increasing distance from the center. The hardness increase is faster with increasing number of the revolution as reported in other metallic materials [16-18]. All values of the microhardness are plotted against the equivalent strain in Fig. 3.2.2(b). Here, the following equation is used for the calculation of the equivalent strain [14].

$$\varepsilon = (1 - s) \int_0^N \frac{2\pi r}{\sqrt{3} t(N)} dN \qquad (3.2.2)$$

where r is the distance from the disk center, N is the number of revolutions, s is the fraction of slippage and $t(N)$ is the disk thickness after HPT processing. The value of s was measured at each pressure for both metals using a procedure as in Ref. [19] and was found to be in the rage of 0.1 to 0.2. The form of $t(N)$ was determined as a function of N by measuring the thicknesses after several different revolutions as in Ref. [20].

Figure 3.2.2(b) shows that the hardness increases with increasing equivalent strain at an early stage of straining but appears to saturate to a level of 225 Hv at higher strains. Similar hardness variations were reported in many different metals and alloys after processing by HPT [14, 16-18].

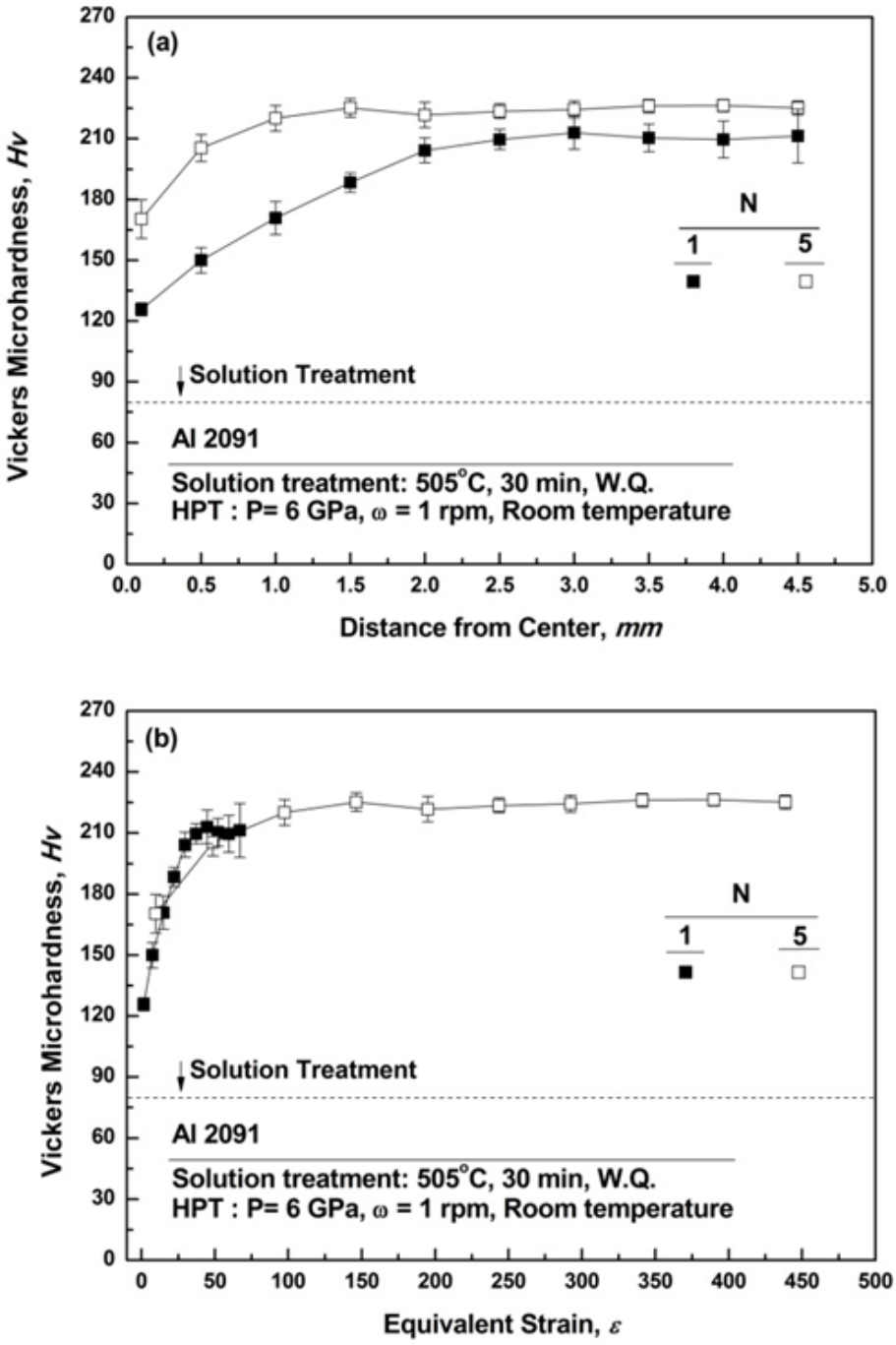

Figure 3.2.2. Vickers microhardness plotted (a) against distance from center and (b) against equivalent strain for 2091 alloy after HPT processing under 6 GPa for 1 and 5 revolutions.

3.2.3. (1-b) Aging after HPT process

The HPT-processed disks for 5 revolutions were aged at 100, 150 and 190°C. Figure 3.2.3(a), (b) and (c) plots the hardness variation with the distance from the disk center after aging at 100, 150 and 190°C for different periods up to 804 ks (9.3 days), respectively. For the aging at 100 and 150°C, the hardness level increases gradually with aging time above the as-HPT level and this increase occurs equally irrespective of the positions from the disk center. For the aging at 190°C, there is no hardness increasing but the hardness decreases below the as-HPT level from the beginning of the aging. The temperature of 190°C is too high to obtain hardness increase in the HPT-processed samples.

Taking average at the saturation level in the plots of hardness against the distance from the disk center in Fig. 3.2.3(a), (b) and (c), the average values are plotted in Fig. 3.2.4 with aging time. Figure 3.2.4 includes the hardness variation with aging time not only for the HPT-processed samples but also for cold-rolled samples for comparisons. Several important features arise. (1) Hardening occurs above the as-HPT level by aging at 100°C and 150°C. At 190°C, however, the hardness decreases from the beginning of aging. (2) The hardness continuously increases even after aging for 9.3 days at 100°C but begins to decrease for aging at 150°C after 2.3 days. (3) The hardness reaches the highest level of 275Hv by aging at 100°C for 9.3 days and at 150°C for 2.3 days. (4) For the 50%-rolled samples, hardening occurs by aging at any temperature of 100, 150 and 190°C. The highest hardness of 180Hv is reached after aging at 150°C for 4.6 days. (5) Comparison clearly indicates that the hardness levels attained by aging are much higher in the HPT disks than in the cold-rolled disks.

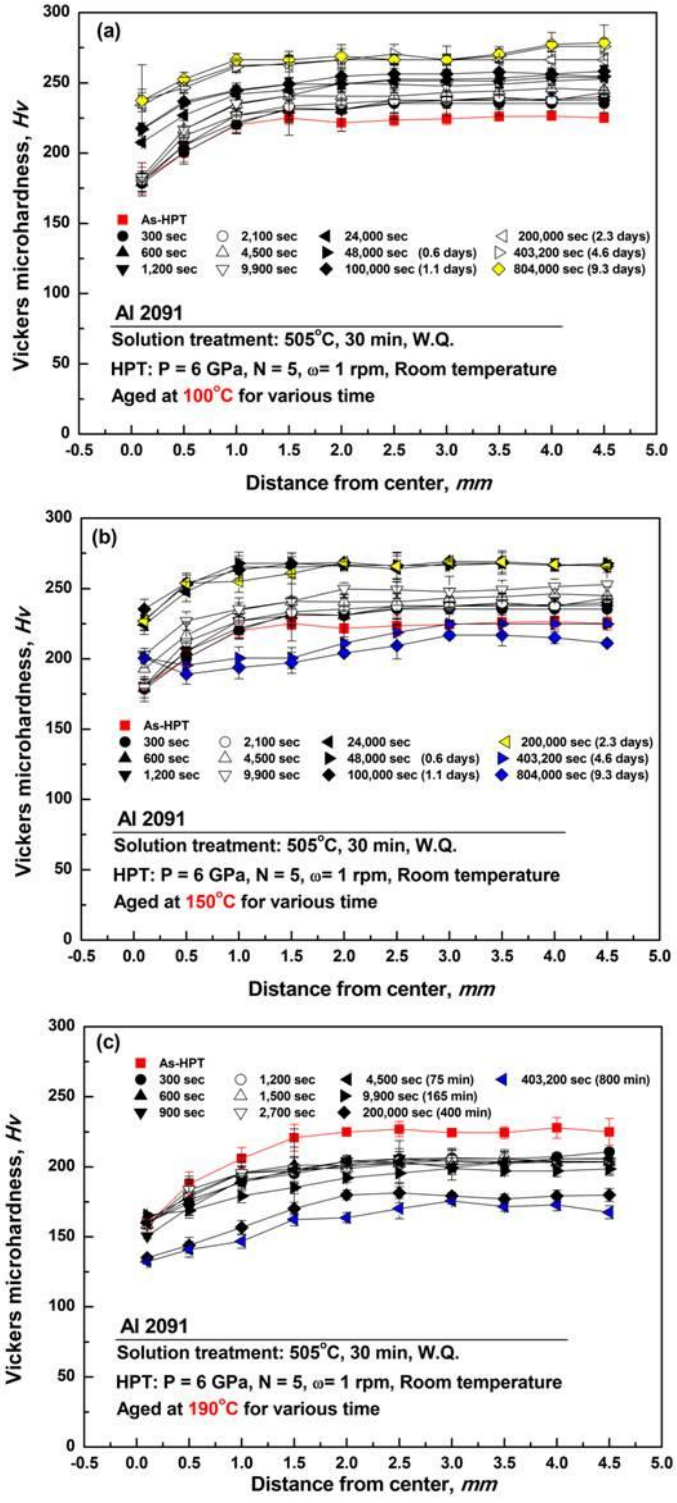

Figure 3.2.3. Hardness variation against distance from disk center after processing with HPT and aging at (a) 100°C, (b) 150°C for periods up to 804 ks (9.3 days) and (c) 190°C for periods up to 800 min.

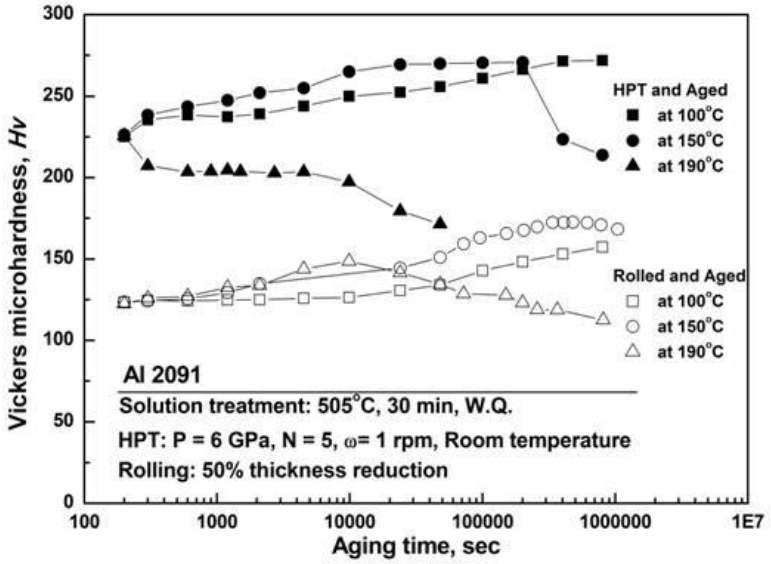

Figure 3.2.4. Hardness variation against aging time both HPT-processed and cold-rolled samples.

3.2.3. (2) Bending tests

The stress-displacement curves are delineated in Fig. 3.2.5 for the samples processed for N = 5 under 6 GPa including the pressing direction as illustrated in the inset. The bending strength of the as-HPT sample shows 1,200 MPa with some ductility. After peak aging at 150^{o}C for 2.3 days, the bending stress was further increased without loss of ductility. However, once they passed peak aged periods, the bending stress tends to decrease with almost little plastic elongation.

3.2.3. (3) Fractography

The fracture surfaces of bending specimens were examined by FE-SEM. Images in Fig. 3.2.6 show overall views of the fracture surfaces from samples with an aging temperature of 150^{o}C. Figure 3.2.6(a) corresponds to the as-HPT condition, Fig. 3.2.6 (b) to the sample aged for 2.3 days (peak-aged), Fig. 3.2.6(c) to the high magnification image of Fig. 3.2.6(d) to the sample aged for 9.3 days (over-aged).

In Fig. 3.2.6(a), the fracture surface shows a ductile-type intergranular dimple pattern. The dimple size is quite large; ~2 μm in size dimples can be observed on the surface (pointed with arrows). However, in Fig. 3.2.6(b), fewer large dimples can be observed. The clear appearance of the fractured surfaces are composed of finer dimples as ~300 nm in size as shown in Fig. 3.2.6(c). It is considered that well dispersed precipitates (δ`, Al_3Li) prevent the alloy from crack propagation while loading, and this is consistent with the observed increase in tensile strength without a significant loss in the ductility. In the over-aged fractured surface as shown in Fig. 3.2.6(d), a shell-like pattern composed of fine, sharply torn and clear areas are visible. It was demonstrated by Itoh *et al.* [11], that coherent δ` precipitates change to incoherent δ precipitates after

prolonged aging and this significantly reduces the strength and elongation in the tensile deformation of the 2091 alloy.

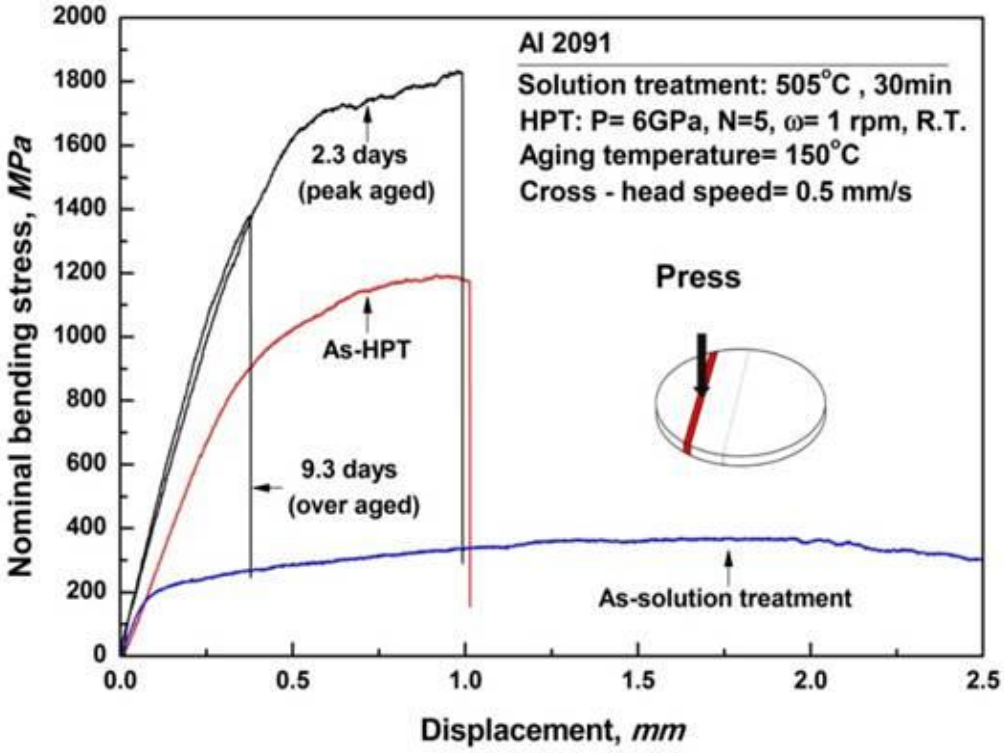

Figure 3.2.5. Nominal bending stress versus displacement curves after bending testing for 2091 alloys after HPT and aging treatment.

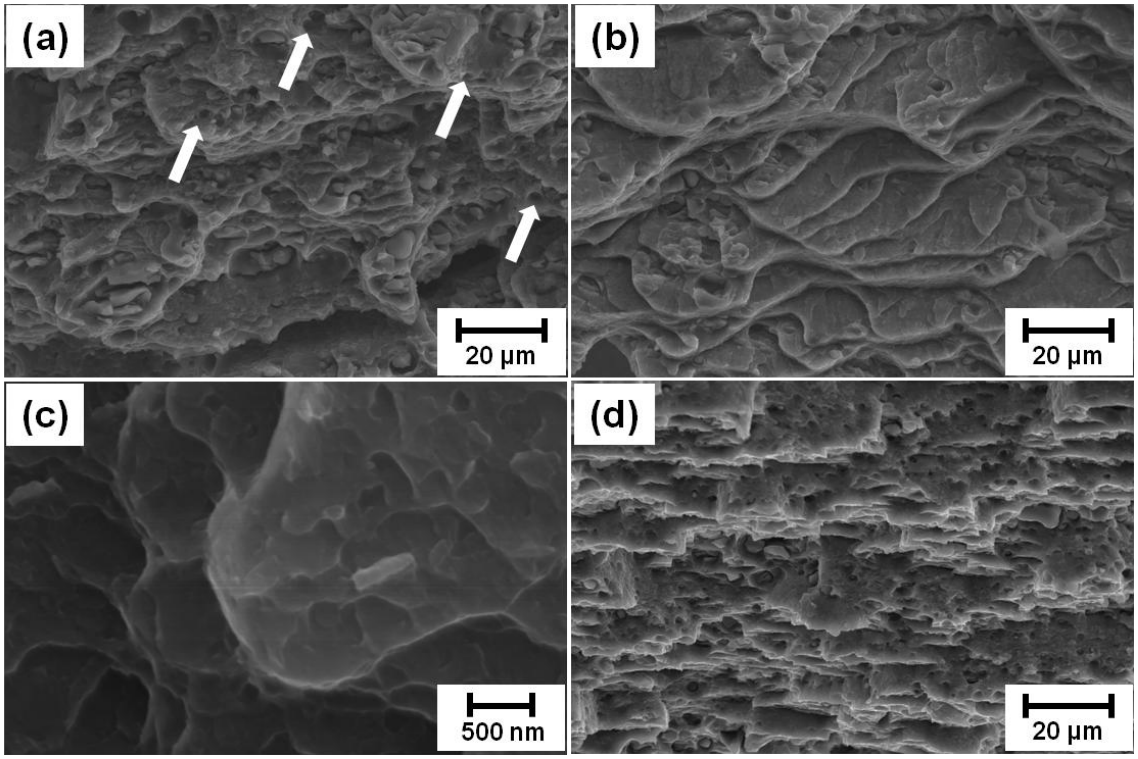

Figure 3.2.6. SEM fractographs after bending testing for 2091 alloy: (a) as-HPT sample, (b) aged for 2.3 days at 150^{o}C after HPT (peak-aged), (c) high magnification image of (b), and (d) aged for 9.3 days at 150^{o}C after HPT (over-aged).

3.2.3. (4) TEM microstructure observation

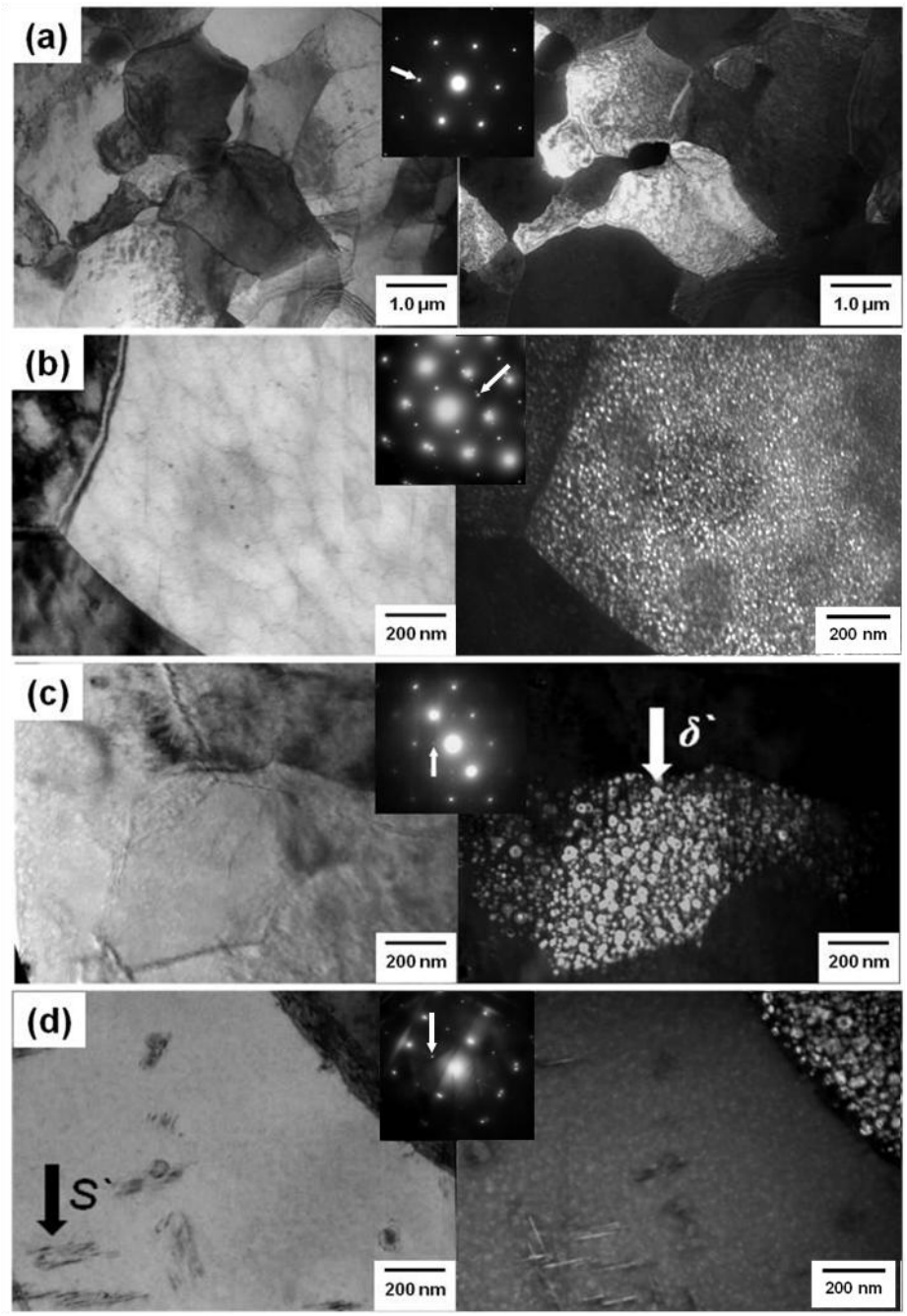

Figure 3.2.7. TEM micrographs and SAED patterns of not HPT processed 2091 alloy: (a) as-solution treated, (b) aged at 150^{o}C for 30 min, (c) aged at 150^{o}C for 4 days and (d) aged at 150^{o}C for 7 days.

Figure 3.2.7 shows TEM micrographs and SAED patterns of the samples (a) solution treated at 505°C for 30 min, solution treated and aged at 150 °C for (b) 30 min, (c) 4 days and (d) 7 days. Bright-field images are shown on the left and dark-field images on the right of Figure 3.2.7. The dark field images were taken from the diffracted beams indicated by arrows in the SAED patterns. In Fig. 3.2.7(a), the structure consists of fully recrystallized, equiaxed grains with a size of 3~5 μm and it is confirmed that there are no particles after solution treatment. In Fig. 3.2.7(b), δ` ($Al_3Li$) precipitates were observed with the size in the range of 10 to 20 nm. . The δ` phase has crystallographic relationship with the matrix as $[110]_{Al}//[110]_{\delta`}$. Figure 3.2.7(c), shows the size of the δ` precipitates increased to 30-50 nm and as shown in Fig. 3.2.7(d), the S` (Al_2CuMg) precipitates are visible in the matrix as marked by an arrow.

Representative microstructures after HPT processing and aging treatment are shown in Fig. 3.2.8: (a) HPT-processed sample, and the samples subsequently aged at (b) 100°C for 9.3 days, (c) 150°C for 9.3 days and (d) 190°C for 800 min. The corresponding SAED patterns were taken from regions having a diameter of 6.3 μm. The dark-field images and the ring form of the SAED patterns show that an ultrafine-grained structure with high angle grain boundaries was formed by the HPT processing. The average grain size of the HPT-processed sample was measured as ~140 nm.

Observation of Fig. 3.2.8 (b), (c) and (d) reveals that the ultrafine-grained structures with high angle grain boundaries are still retained after the aging treatment. Although grain growth occurs during aging at 150°C and 190°C, the amount of grain growth is minor as ~160 nm and ~180 nm even after long time aging.

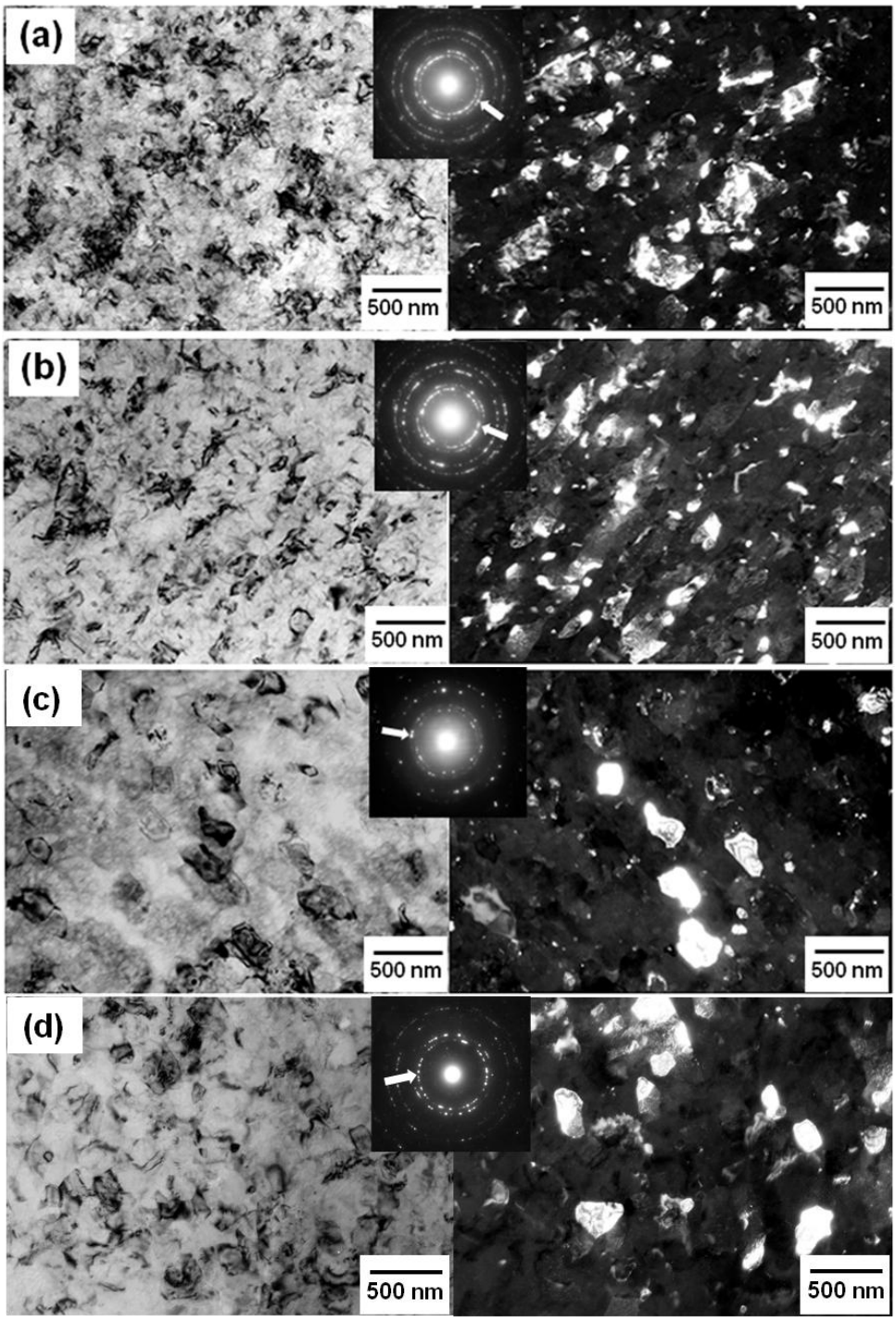

Figure 3.2.8. TEM micrographs and SAED patterns of HPT processed 2091 alloy with 5 revolutions under 6 GPa: (a) as-HPT, (b) aged at 100^{o}C for 9.3 days (over-aged), (c) aged at 150^{o}C for 9.3 days (over-aged) and (d) aged at 190^{o}C for 800 min (over - aged).

This observation is more quantitatively documented in Fig. 3.2.9 with grain size distributions (a) after prolong aging at 100°C and 190°C and (b) after aging for 2.3 and 9.3 days at 150°C including the grain size distribution for the as-HPT condition for comparison The average grain sizes at the corresponding conditions are also summarized in Table 3.2.1.

Figure 3.2.10 shows TEM images after (a) HPT processing, and after HPT processing and subsequently aging at 150°C (b) for 2.3 days (peak aging) and (c) for 9.3 days (over aging). In Fig. 3.2.10(a), dimly spots are visible as marked by arrows and this indicates the formation of δ` precipitates possibly due to heat generation during HPT processing. Sato and Kamio [21] reported the formation of clusters resemble to the δ` phase even in the quenched state. In Fig. 3.2.10 (b) and (c), δ` precipitates with the size of ~20 nm are observed within the fine grains and they have crystallographic orientation relationship with the matrix as $[001]_{Al}//[001]_{\delta`}$. It should be noted that this is the same orientation relationship as observed in the sample without HPT processing. It is confirmed that the crystallographic structure including coherency is retained even for the precipitation within the small grains produced by HPT processing. It is reasonable to conclude that such a fine dispersion of particles after aging leads to the increase in hardness as demonstrated in Fig. 3.2.3 and to the bending stress as shown in Fig. 3.2.5. For the over aged sample, S` ($Al_2CuMg$) precipitates were not found in Fig. 3.2.10(c) but, nevertheless both hardness and bending stress were decreased. It is considered that the decrease in the hardness is due to coarsening of the δ` particles and probably due to the formation.

3.2.4. Summary and conclusions

1. Ultrafine-grained structure with a grain size of ~140 nm was achieved in an Al-Li-Cu-Mg alloy (2091) through application of HPT under a pressure of 6 GPa for 5 revolutions.

2. Such a fine grain structure was retained during aging at 100^{o}C and 150^{o}C for up to 9.3 days, while age hardening occurs to increase the hardness well above the hardness level achieved by the HPT processing.

3. A fine dense dispersion of δ`(Al_3Li) precipitates was observed within the small grains and such a formation of precipitates was responsible for the strengthening during aging of the HPT processed 2091 alloy because no significant grain coarsening occurs.

4. Simultaneous hardening due to aging and grain refinement was attained in the 2091 alloy.

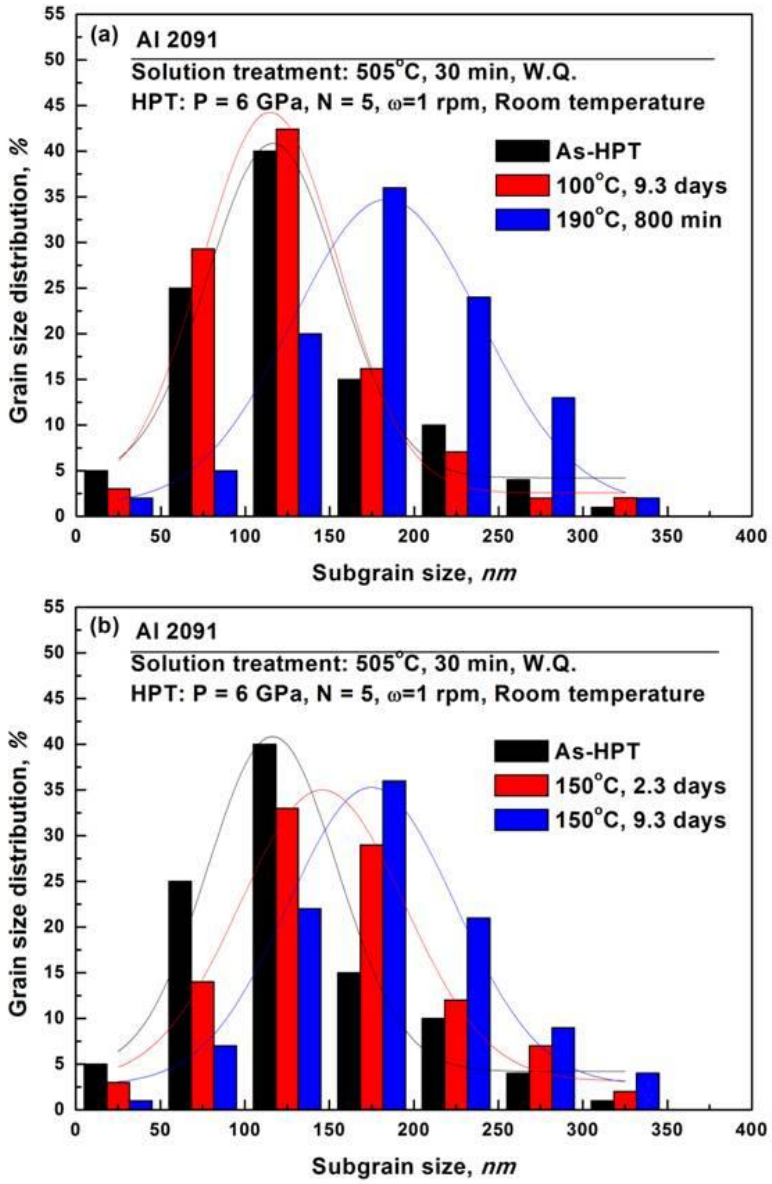

Figure 3.2.9. Grain size distribution of 2091 alloy: under P= 6 GPa for 5 revolutions (a) as-HPT, aged at 100°C and 190°C and (b) as-HPT and aged at 150°C.

Table 3.2.1 Grain sizes for 2091 alloy after HPT process and aging treatment.

Before HPT	After HPT				
As- solution treated	As-HPT	100°C, 9.3 days	150°C, 2.3 days	150°C, 9.3 days	190°C, 800 min
~5μm	140nm	140nm	160nm	160nm	180nm

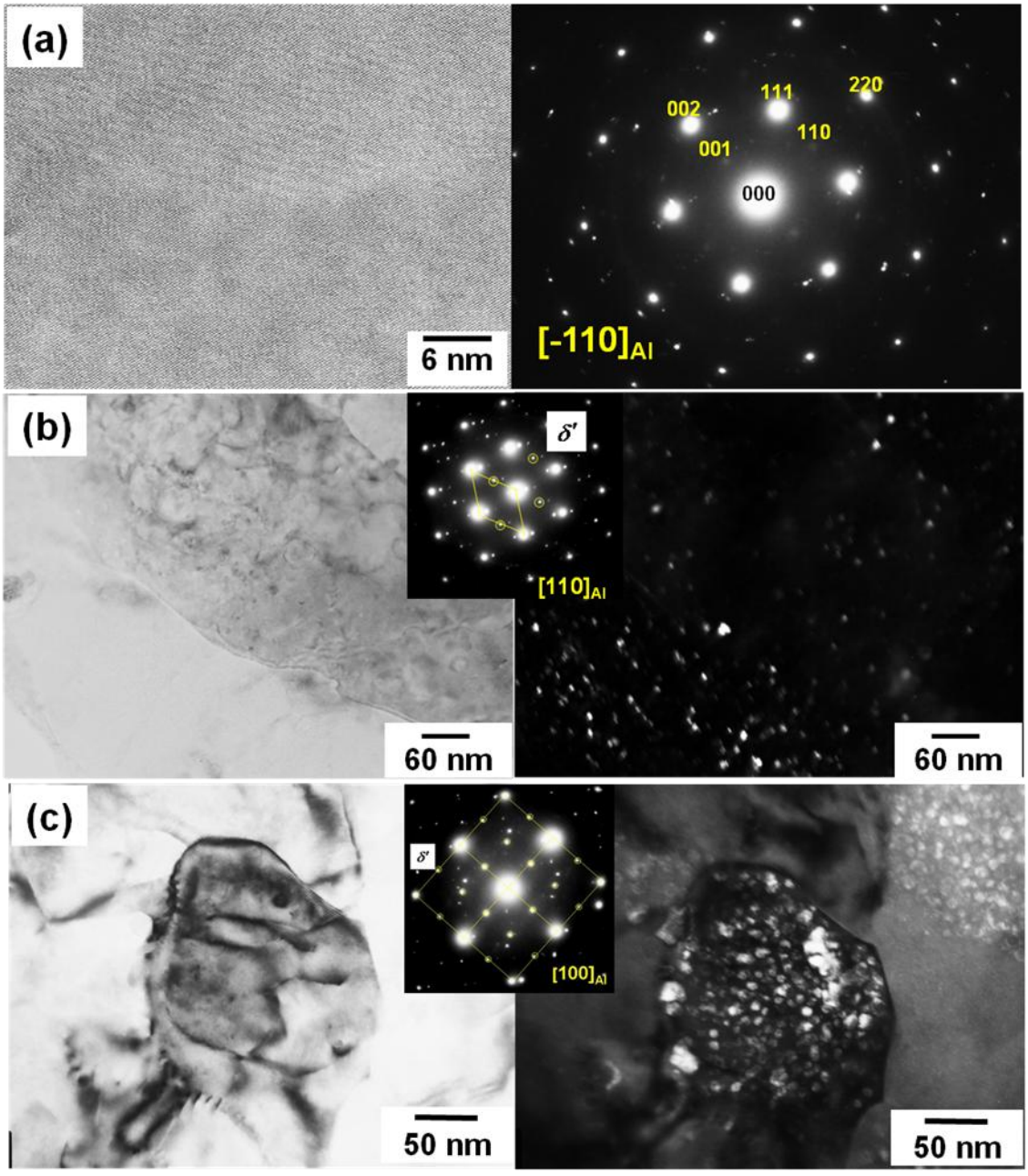

Figure 3.2.10. High resolution TEM micrographs and SAED patterns of HPT processed 2091 alloy with 5 revolutions under 6 GPa: (a) as-HPT, (b) aged at 150^{o}C for 2.3 days (peak-aged), (c) aged at 150^{o}C for 9.3 days (over-aged).

References

1. T. H. Sanders, Jr., Al-Li-X alloys-an overview. In: T.H. Sanders, E.A. Starke, Editors, Proc. 1st Int. Aluminium-Lithium Alloys Conf., The Metallurgical Society of AIME, Warrendale, PA, 1981.

2. B. Noble, G. E. Thompson, Met. Sci. J. 5 (1971) 114-120.

3. R.Z. Valiev, R.K. Islamgaliev, I.V. Alexandrov, Prog. Mater. Sci. 45 (2000) 103-189.

4. G. Sakai, K. Nakamura, Z. Horita, T. G. Langdon, Mater. Sci. Forum 503-504 (2006) 391-396.

5. J.K. Kim, H.G. Jeong, S.I. Hong, Y.S. Kim, W.J. Kim, Scripta Mater. 45 (2001) 901-907.

6. Z. Horita, K. Ohashi, T. Fujita, K. Kaneko, T.G. Langdon, Adv. Mater. 17 (2005) 1599-1602.

7. K. Ohashi, T. Fujita, K. Kaneko, Z. Horita, T.G. Langdon: Mater. Sci. Eng. A 437 (2006) 240-247.

8. D. S. McDarmaid, Mater. Sci. Eng. A 101 (1988) 193-200.

9. P. Gomiero, F. Livet, Y. Brechet, F. Louchet, Acta Metall. Mater. 40 (1992) 847-855.

10. P. Gomiero, Y. Brechet, F. Louchet, A. Tourabi, B. Wack Acta Metall. Mater. 40 (1992) 857-861.

11. G. Itoh, M. Kanno, T. Hagiwara, T. Sakamoto, Acta Mater. 47 (1999) 3799-3809.

12. P.W. Bridgman, Phys. Rev. 48 (1935) 825-847.

13. A.P. Zhilyaev, T.G. Langdon, Prog. Mater. Sci. 53 (2008) 893-979.

14. K. Edalati, T. Fujioka, Z. Horita, Mater. Trans. 50 (2009) 44-50.

15. ASTM E290, Standard Test Methods for Bend Testing of Material for Ductility, ASTM International, West Conshohocken, PA, 2009.

16. K. Edalati, T. Fujioka, Z. Horita, Mater. Sci. Eng. A 497 (2008) 168-173.

17. S. Lee, K. Edalati, Z. Horita, Mater. Trans. 51 (2010) 1072-1079.

18. K. Edalati, E.Matsubara, Z. Horita, Metall. Mater. Trans. A 40 (2009) 2097-2086.

19. Y. Todaka, J. Sasaki, T. Moto, M. Umemoto, Scripta Mater. 59 (2008) 615-618.

20. Y. Ito, Z. Horita, Mater. Sci. Eng. A 503 (2009) 32-36.

Chapter 4. Aging behavior of ultrafine structured Fe-50at%Ni alloy after processing by high-pressure torsion

4.1. Introduction

According to the equilibrium phase diagram [1, 2], some intermetallic phases such as $FeNi_3$, FeNi and Fe_3Ni are reported to exist in the temperature range below 800 K. Among the intermetallics, the FeNi ordered phase called tetrataenite is discovered only in meteorite in nature and requires a very slow cooling rate (1 K/10^6 year) to form because it exists below the temperature as low as 593 K according to the phase diagram.

It is now well known that severe plastic deformation (SPD) introduces intense strain in metallic materials and thus an enormous amount of lattice defects is produced [3]. It was reported that atomic diffusion is significantly enhanced by the presence of lattice defects [4]. *In situ* observation indicated that the density of the lattice defects is fairly close to the melting point of the material [5]. It is then anticipated that the formation of such an intermetallic ordered phase as FeNi may be feasible. In this study, high-pressure torsion (HPT) which is a typical SPD process is applied to examine any possible formation of the second through annealing after the HPT process.

4.2. Experimental materials and procedures

An ingot of an Fe-50at%Ni alloy was prepared by arc-melting using high purity Fe (99.99%) and Ni (99.97%) in argon atmosphere. The ingot was homogenized at 1273 K for 3 hours in a tube filled with argon gas. The ingot was sliced to thicknesses of 1

mm and ground to 0.85 mm. Disks with 10mm diameter were then cut from the slices by a wire-cutting electric discharge machine. The disks were processed by HPT under a pressure of 6 GPa for 1/4, 1, 2, 5 or 10 revolutions with a rotation speed of 1 rpm at room temperature. The alignment around the rotation axis of the upper and lower anvils was adjusted to well within ±0.01 mm. Slippage between the disk and the anvils was measured after 1/4 revolutions as in Ref. [6]. After processing by HPT, annealing was conducted at 583 K for up to 40 days in a tube filled with argon gas.

The disks were mechanically polished to mirror-like surfaces and Vickers microhardness was measured along 12 radial directions at every 0.5 mm from the disk center. The average values were calculated from the twelve separate measurements at the same distances from the disk center. Each hardness measurement was conducted by applying a load of 200 g for duration of 15 s. XRD analyses were conducted using a Rint-2100 diffractometer with a Cu target and also a synchrotron facility of the SAGA light source (in Saga prefecture, Japan) with a Co target.

For transmission electron microscopy (TEM), disks with 3mm diameter were punched from the edge parts (corresponding to hardness saturated area as shown below) of the HPT-processed disks. They were ground to a thickness of 0.15 mm and further thinned using a twin-jet electro-polishing apparatus in a solution of 5vol% $HClO_4$, 20vol% CH_3OH and 75vol% CH_3COOH at 263 K with 20 V. The microstructures were observed using a Hitachi H-8100 transmission electron microscope operating at 200 kV. Selected area electron diffraction (SAED) patterns were taken from regions having diameters of 6.3 μm.

4.3. Results and discussions

4.3. (1) Vickers microhardness measurement

Vickers microhardness is plotted in Fig. 4.1(a) against the distance from the disk center after HPT processing for 1, 2, 5 and 10 revolutions. For all revolutions, the microhardness increases with increasing distance from the center. The hardness increase is faster with increasing number of the revolution as reported in other metallic materials [9-12]. This can be seen more clearly when hardness values are plotted as a function of equivalent strain. All values of the microhardness are plotted against the equivalent strain in Fig. 4.1(b). Here, the equivalent strain was calculated by the equation as [8]

$$\varepsilon = (1 - \mathrm{s}) \int_0^N \frac{2\pi r}{\sqrt{3}t(N)} dN \qquad (4.1)$$

where r is the distance from the disk center, N is the number of revolutions, s is the fraction of slippage and $t(N)$ is the disk thickness after HPT processing. The value of s was measured at each pressure for both metals using a procedure as described in Ref. [8] and was found to be in the range of 0.1 to 0.2. The form of $t(N)$ was determined as a function of N by measuring the thicknesses after several different revolutions as in Ref. [8]. Figure 4.1(b) shows that the hardness increases with increasing equivalent strain at an early stage of straining but appears to saturate to a constant level of ~400 Hv at higher strains. Hardness remains unchanged after reaching the steady-state with further straining. A single level of saturation is achieved in both metals and the microhardness data fall on one unique curve. Similar hardness variations were reported in many different metals and alloys after processing by HPT [7-10].

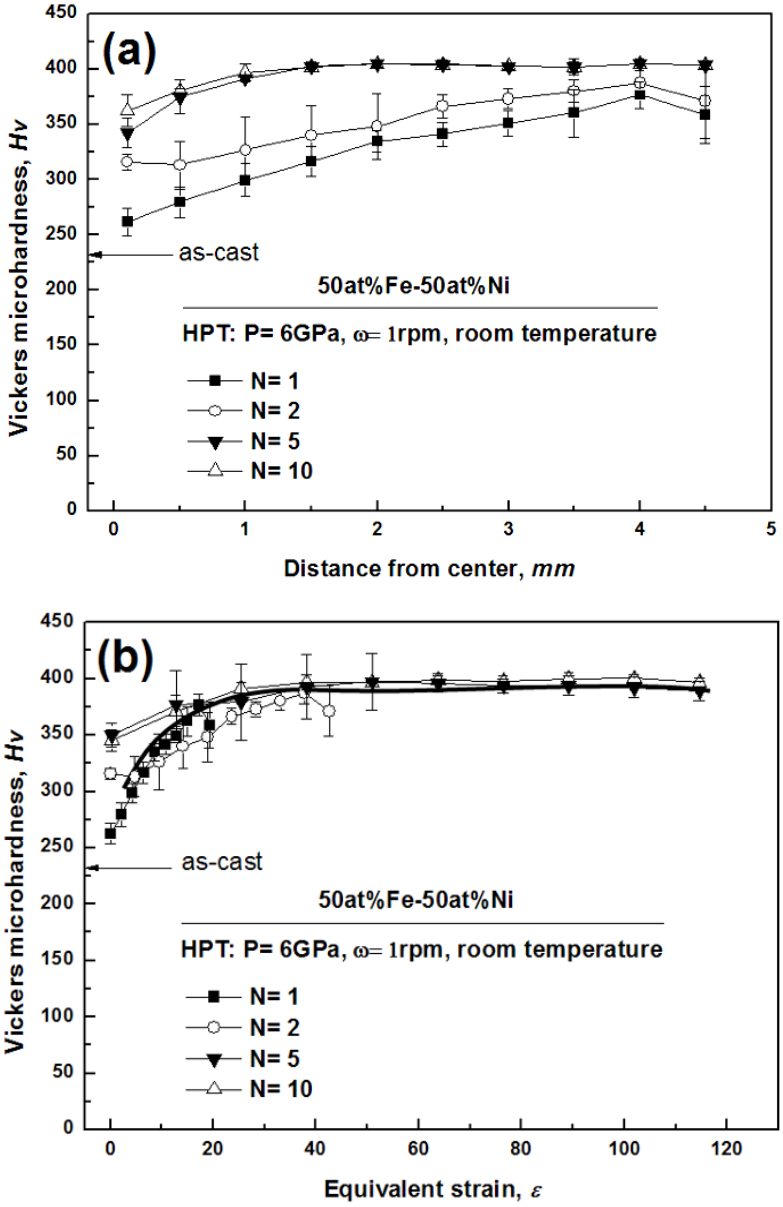

Figure 4.1. Vickers microhardness plotted against (a) distance from center and (b) equivalent strain.

4.3. (2) Microstructure observation

Figure 4.2 shows optical micrographs of the FeNi alloy (a) in the as-cast condition and (b) after homogenization at 1273 K for 3 hours. The grain sizes for both as-cast and homogenized states are of ~800 μm and there is no significant change in the grain size and configuration by the homogenization treatment

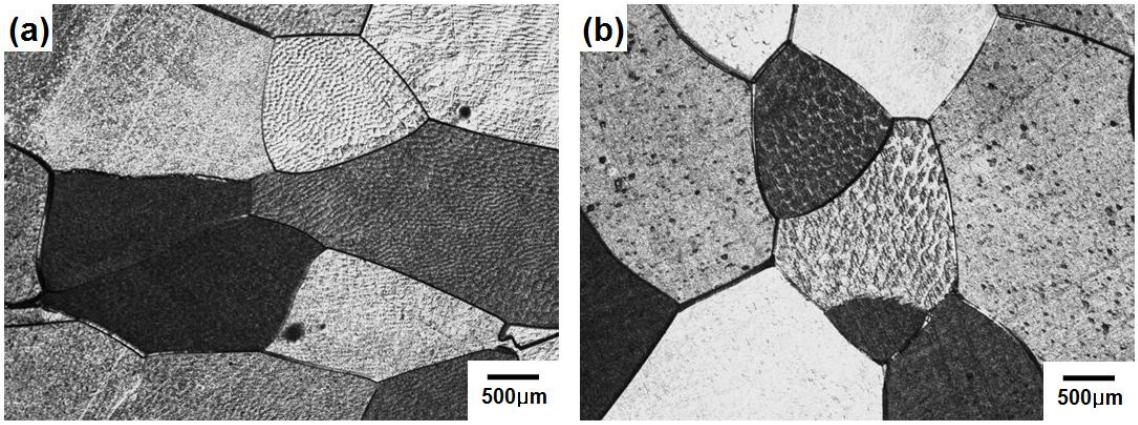

Figure 4.2. Optical micrographs of Fe-Ni alloy (a) in as-cast state and (b) after homogenization at 1273K for 3 hours.

Figure 4.3 shows TEM micrographs including SAED patterns of the FeNi alloy after HPT processing for 5 revolutions under 6 GPa. Those of the sample further annealed at 583K for 40 days after the HPT processing are shown in Fig. 4.4. For both figures, bright-field images are shown on the left and dark-field images on the right. The dark field images were taken with the diffracted beams indicated by arrows in the SAED patterns. It is now found that, by the HPT processing, the grain size was significantly refined to the size of ~120 nm with high angle boundaries. After the subsequent annealing process, the grain size was measured to be ~125 nm and there was essentially no grain coarsening during the annealing process.

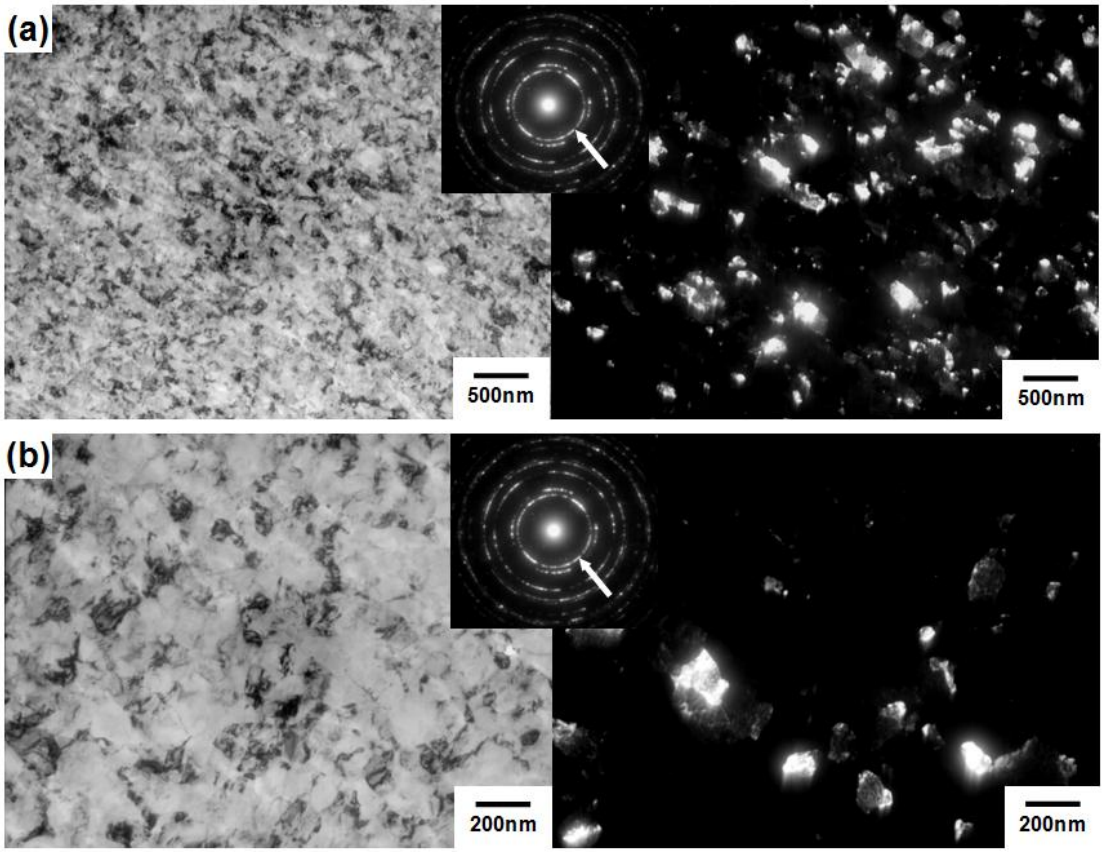

Figure 4.3. TEM micrographs of Fe-Ni alloy after HPT under pressure of 6 GPa for 5 revolutions: (a) low magnification and (b) high magnification.

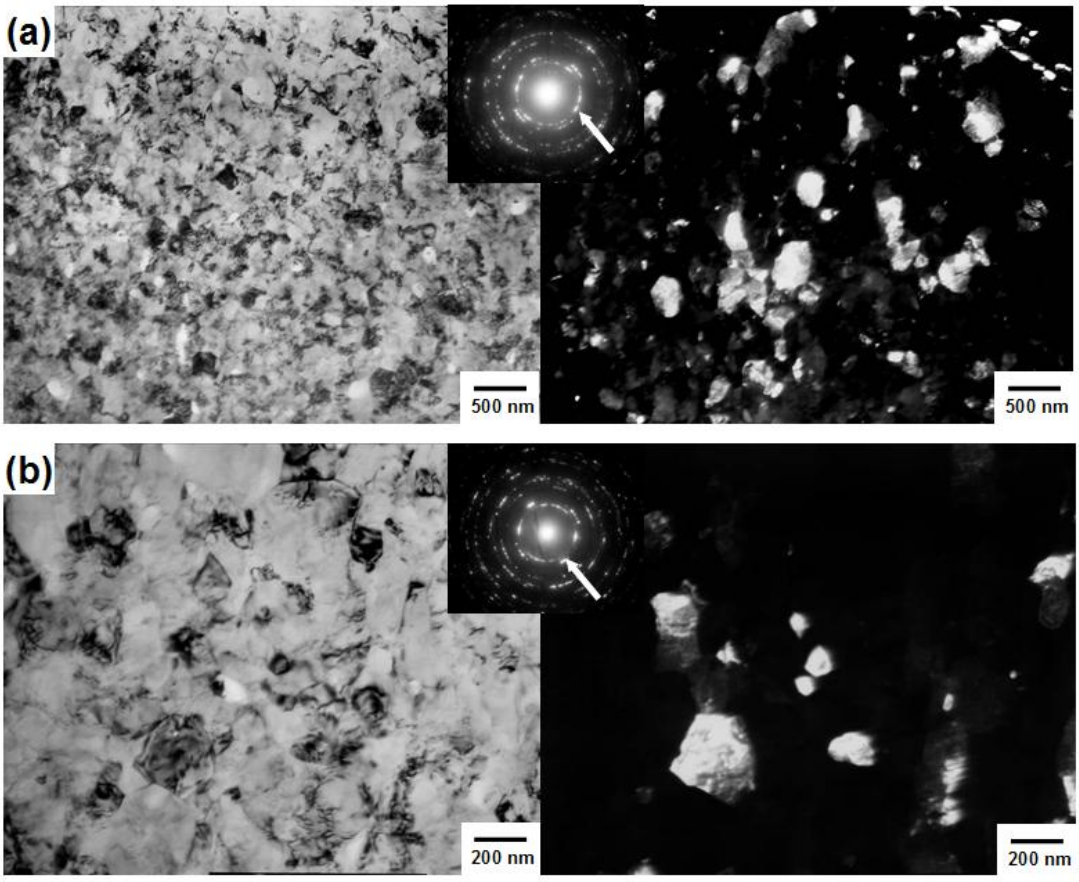

Figure 4.4. TEM micrographs of HPT-processed Fe-Ni alloy after annealing at 583 K for 40 days: (a) low magnification and (b) high magnification.

4.3. (3) XRD analysis

Figure 4.5(a) shows XRD profiles obtained after HPT and the subsequent annealing at 583 K for 3 days and 10 days. Close inspection of the XRD profiles reveals two important points: first, there is an appreciable difference in the peak width as evident from the enlarged part of the profiles shown in Fig. 4.5(b). Whereas the peak width is wider after the HPT process, it is narrower after the subsequent annealing. This indicates that a large strain is stored in the sample after HPT and it is released in the annealed sample; second, a new peak appeared during the annealing as marked by an arrow in Fig. 4.5(a). This peak is more distinctive in the XRD profiles obtained by the synchrotron facility as marked in Fig. 4.5(c). This new peak is identified as an α-Fe phase and it provides very promising possibility that the ordered FeNi phase might be present because the tetrataenite structure forms along the interphase between α-Fe(or α(Fe,Ni)) and γ-Fe(or γ(Fe,Ni)) with a form of very thin layer.

4.3. (4) Evaluation of atomic diffusion

It may be possible to evaluate a diffusion distance of Ni atoms in the γ (Fe, Ni) matrix when the sample is held at 583 K for 40 days. The following equation is used for this evaluation.

$$x \approx 2\sqrt{Dt} \tag{4.2}$$

where D is the diffusion coefficient and t is the time. In this research, grain boundary diffusivity of Ni in Fe-based alloy is used to calculate the diffusion distance. Because the diffusivity is available only at temperatures higher than 1073 K [11], extrapolation is made to the temperature of 583 K to yield $D = 2.0\times10^{-24}$ m^2 s^{-1}.

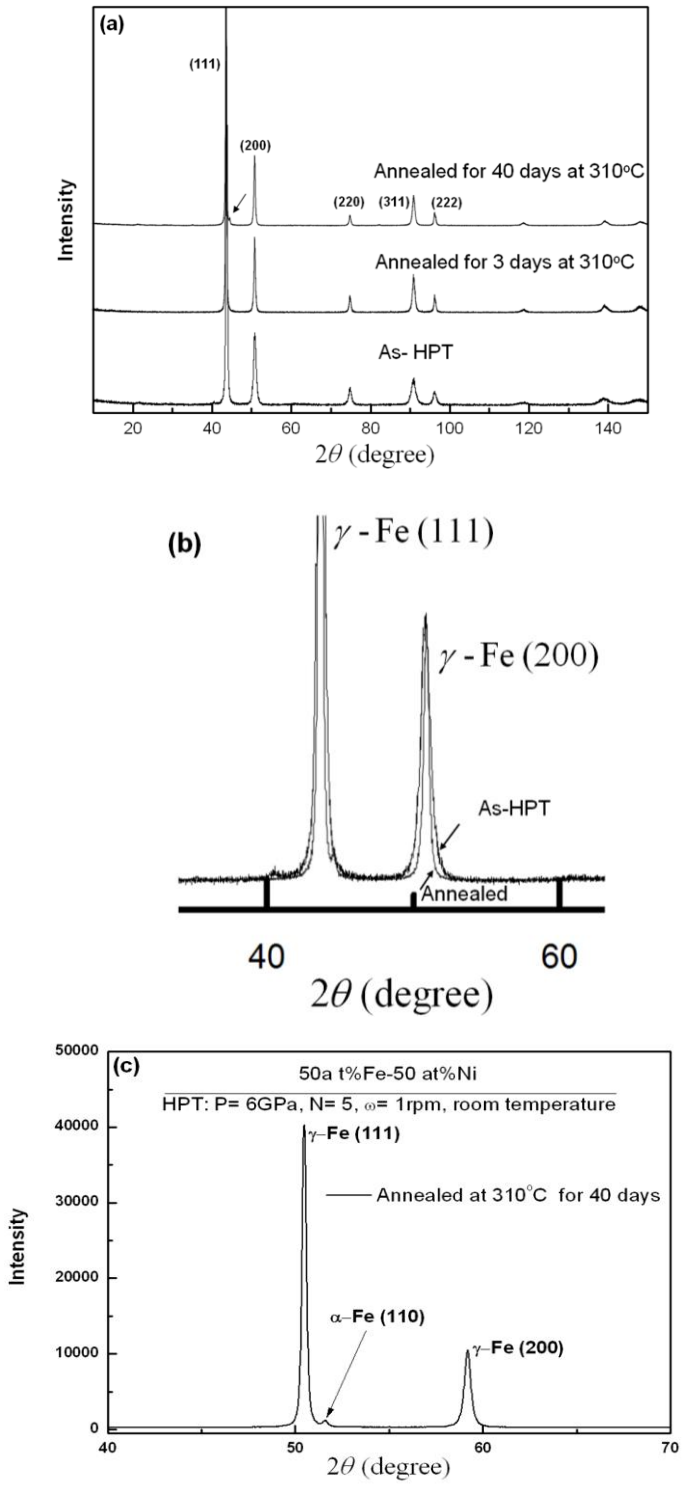

Figure 4.5 (a) XRD profiles of Fe-Ni alloy after HPT processing and subsequent annealing, (b) enlargement of peak profiles near γ-Fe(111) and γ-Fe(200), and (c) XRD profile from synchrotron facility.

Thus it follows that the diffusion distance at 583 K for 40 days can be ~5 nm. It appears that this diffusion distance is short when compared with the grain size, 125 nm, but this estimation is based on the condition without any strain. Provided that the diffusion coefficient is higher by two orders of magnitude because of the intense strain introduced by HPT, the diffusion distance should be ~50 nm which is now one half of the grain size. This can be reasonable and it is concluded that many lattice defects including grain boundaries generated during HPT processing are sufficient to produce precipitates as the α phase.

4.4. Summary and conclusions

An Fe-50at% Ni alloy was subjected to HPT and subsequently annealed at 583K for up to 40 days. The following conclusions are drawn from this study.

1. Significant grain refinement form the initial grain size of ~800 μm to ~120 nm was attained by the process of HPT. This grain size was essentially retained by the subsequent annealing at 583 K for 40 days.
2. XRD analysis showed that appreciable annihilation of lattice defects occurred during the annealing.
3. High-intensity XRD analysis using the synchrotron facility revealed unambiguously that a new peak corresponding to an α-Fe phase appears after the annealing for 40 days.

References

1. J.F. Albertsen, G.B. Jensen, J.M. Knudsen, Nature 273 (1978) 453-454.

2. K.B. Reuter, D.B. Williams, J.I. Glodstein, Metall. Trans. A. 20A (1989) 719-725.

3. R.Z. Valiev, Y. Estrin, Z. Horita, T.G. Langdon, M.J. Zehetbauer, Y.T. Zhu, JOM 58(4) (2006) 33-39.

4. R.Z. Valiev, R.K. Islamgaliev, I.V. Alexandrov, Prog. Mater. Sci. 45 (2000) 103-189.

5. A.R. Kilmametov, G. Vaughan, A.R. Yavari, A. LeMoulec, W.J. Botta, R.Z. Valiev, Mater. Sci. Eng. A 503 (2009) 10-13.

6. K. Edalati, Z. Horita, T.G. Langdon, Scripta Mater 60 (2009) 9-12.

7. K. Edalati, T. Fujioka, Z. Horita, Mater. Sci. Eng. A 497 (2008) 168-173.

8. K. Edalati, T. Fujioka, Z. Horita, Mater. Trans. 50 (2009) 44-50.

9. K. Edalati, Z. Horita, Mater. Trans. 51 (2010) 1051-1054.

10. S. Lee, K. Edalati, Z. Horita, Mater. Trans. 51 (2010) 1072-1079.

11. H. Mehrer, Numerical Data and Functional Relationships in Science and Technology, Diffusion in Solid Metals and Alloys, Vol. 26, Springer-Verleg, Berlin, 1990.

Chapter 5. Summary

In this thesis, it is investigated that the bcc structured refractory metals is deformed using high-pressure torsion (HPT) to produce ultrafine/ nano structures and to enhance their strength. Also, simultaneous strengthening using both grain refinement by HPT process and post annealing is attempted in Al alloys and FeNi alloy. A summary of this study is given in this chapter.

Chapter 1 has presented that a brief description of severe plastic deformation (SPD) including equal-channel angular pressing (ECAP), accumulative roll-bonding (ARB) and HPT processing. Four kinds of strengthening methods are described with brief explanation. A basic concept of combining two strengthening methods, grain refinement and precipitation hardening, are presented and are shown to be attained in this study.

In chapter 2, bcc structured refractory metals of 5th and 6th groups in the periodic table, V^{23}, Cr^{24}, Nb^{41}, Mo^{42} and Ta^{73} are subjected to HPT process at room temperature. Vickers microhardness increases with increasing of equivalent strain in the early stage of straining and then levels off and saturates to a steady state. In the case of 5th group materials, tensile strength is significantly increased compared with as-received specimen with some ductility. However, metals of 6th group are shown brittle fracture patterns. Grain refinement is achieved to the level of ~400nm as confirmed by TEM observation.

In chapter 3, age-hardenable Al-Ag alloys and Al 2091 are subjected to aging treatment after HPT processing. For both alloys, hardness increase is achieved without grain coarsening. Precipitates are observed in ultrafine grains with the sizes of ~20nm

δ` (Al_3Li) particles and of ~10nm η-zone in the Al 2091 and Al-Ag alloys, respectively. These precipitates influence mechanical properties: not only the strength increase but also appreciable presence of ductility is achieved in bending tests of the Al 2091 alloy. For the Al-Ag alloy, an increasing in both tensile strength and elongation are observed after peak aging. The aging time to reach peak hardness is significantly shorter as ~ 40 sec when compared with 10day of aging in an ECAP-processed Al-Ag alloy, 10 days. Both Al 2091 and Al-Ag alloys, simultaneous hardening is achieved by combination of grain refinement and precipitation hardening.

In chapter 4, an Fe-50at%Ni alloy is processed by HPT and then, subjected to post-aging treatment at the temperature of 310^{o}C. During HPT processing, Vickers microhardness increases with increasing equivalent strain and enters into a steady state level. The post-HPT aging leads to a slight increase in hardness. Close inspection using high energy X-ray analysis reveals that the hardness increase results from the formation of α phase. The second phase precipitation is achieved throughout the sample by combining both HPT process and post-aging treatment even at low temperature. It is demonstrated that many lattice defects generated by the HPT process can enhance diffusivity in the FeNi disordered matrix.

Acknowledgments

Sincere appreciation should be expressed mostly to my superviosr, Prof. Zenji Horita for his continuous guidance and support throughout the course of this research. Also, I would like to thank the reviewers of this thesis, Prof. Minoru Nishida (Kyushu University) and Prof. Kenji Matsuda (University of Toyama) for their invaluable condtributions and comments.

It is my great pleasure to thank my colleagues, Dr. Kaveh Edalati, Mr. Hirotaka Matsunaga, Mr. Daichi Akama and Mr. Jorge Mauricio Cubero Sesin (Kyushu University) for their valuable and unyielding support throughout the completion of my thesis.

I would like to thank Prof. Kenji Higashida (Kyushu University) for permitting the use of the bending test facility and Dr. Masaki Tanaka (Kyushu University) for helpful assistance in using the bending test machine.

I would like to thank Prof. Masashi Watanabe (Lehigh University, USA) and Dr. Zyunya Nakamura (Tohoku University) for their helpful cooperation for using of high resolution transmission electron microscopy.

Also, I would like to thank Prof. Shoichi Hirosawa (Yokohama National University) for his invaluable comments about precipitation in Al alloys.

I would like to thank the AQ program for a PhD scholarship from the MEXT (Ministry of Education, Culture, Sports, Science, and Technology), Japan.